AD_____

Award Number: W81XWH-11-1-0306

TITLE: Center for Advanced Bioengineering for Soldier Survivability

PRINCIPAL INVESTIGATOR: Robert E. Guldberg, Ph.D.

CONTRACTING ORGANIZATION: Georgia Tech Research Corporation
                                                Atlanta, GA 30332-0420

REPORT DATE: June 2013

TYPE OF REPORT: Annual Report

PREPARED FOR: U.S. Army Medical Research and Materiel Command
                        Fort Detrick, Maryland 21702-5012

DISTRIBUTION STATEMENT: Approved for Public Release;
                                        Distribution Unlimited

The views, opinions and/or findings contained in this report are those of the author(s) and should not be construed as an official Department of the Army position, policy or decision unless so designated by other documentation.

REPORT DOCUMENTATION PAGE

Form Approved
OMB No. 0704-0188

Public reporting burden for this collection of information is estimated to average 1 hour per response, including the time for reviewing instructions, searching existing data sources, gathering and maintaining the data needed, and completing and reviewing this collection of information. Send comments regarding this burden estimate or any other aspect of this collection of information, including suggestions for reducing this burden to Department of Defense, Washington Headquarters Services, Directorate for Information Operations and Reports (0704-0188), 1215 Jefferson Davis Highway, Suite 1204, Arlington, VA 22202-4302. Respondents should be aware that notwithstanding any other provision of law, no person shall be subject to any penalty for failing to comply with a collection of information if it does not display a currently valid OMB control number. **PLEASE DO NOT RETURN YOUR FORM TO THE ABOVE ADDRESS.**

1. REPORT DATE *(DD-MM-YYYY)*	2. REPORT TYPE	3. DATES COVERED *(From - To)*
Õ¦^æÁ2013	Annual Report	23ÁRá]Á2012 to 22ÁRá]Á2013

4. TITLE AND SUBTITLE

Center for Advanced Bioengineering for Soldier Survivability

5a. CONTRACT NUMBER
W81XWH-11-1-0306

5b. GRANT NUMBER
ÙÎFVÙÒËFFËFË€Ğ€IJ

5c. PROGRAM ELEMENT NUMBER

6. AUTHOR(S)
Guldberg, Robert E., PhD (PI); Boyan, Barbara D., PhD; Barker, Thomas, PhD; Bellamkonda, Ravi, PhD; McDevitt, Todd, PhD.

5d. PROJECT NUMBER
10188001

5e. TASK NUMBER

5f. WORK UNIT NUMBER

7. PERFORMING ORGANIZATION NAME(S) AND ADDRESS(ES)
Georgia Tech Research Corporation

Atlanta, GA 30332-0420

8. PERFORMING ORGANIZATION REPORT NUMBER

9. SPONSORING / MONITORING AGENCY NAME(S) AND ADDRESS(ES)
ÛÈUÈÁNã↑]ÁRæä↔´á→ÁÞæbæáã´åÁá^äÁRá\æã↔æ→ÁO~↑↑á^äÁÁÁÁÁÁÁÁ

Ô~ã\ÁŒæ\ã↔´←ÊÁRáã]→á^äÁÁGFÍ€GËI€FGÁ

10. SPONSOR/MONITOR'S ACRONYM(S)

11. SPONSOR/MONITOR'S REPORT NUMBER(S)

12. DISTRIBUTION / AVAILABILITY STATEMENT "Fkuvtkdwvkqp"Wpnkokvgf

13. SUPPLEMENTARY NOTES

14. ABSTRACT
The goal of this research effort and center is to use advanced bioengineering to develop technologies that will facilitate the transfer of research in musculoskeletal biology and regenerative medicine to patient care. While much is known about the basic biology of cells in the musculoskeletal system, efforts to convert this information to useful products have been limited. This is in part because the technology development teams have failed to include clinicians and engineers collaborating to ensure that the outcomes have clinical utility and the devices can be fabricated and delivered appropriately for medical applications. In addition industry involvement has typically occurred late in the technology development cycle, often requiring re-engineering before inventions can be incorporated into existing products. To avoid these pitfalls, investigators in the Center for Advanced Bioengineering for Solider Survivability have worked in teams that include a clinician with experience in military medicine bioengineers, and bioscientists with experience working closely with industry, and wherever possible, an industry partner committed to rapid transfer of the novel technologies. Our over-arching hypothesis is that if technology is developed in this manner, it will move quickly to commercialization in a form that has clinical usefulness.

15. SUBJECT TERMS
Trauma; bone repair; bioengineering; preclinical models; adult stem cells; translational research.

16. SECURITY CLASSIFICATION OF: U			17. LIMITATION OF ABSTRACT: SAR	18. NUMBER OF PAGES	19a. NAME OF RESPONSIBLE PERSON Robert E. Guldberg, PhD
a. REPORT	b. ABSTRACT	c. THIS PAGE		72	19b. TELEPHONE NUMBER *(include area code)* 404-894-6589

Standard Form 298 (Rev. 8-98)
Prescribed by ANSI Std. Z39.18

Table of Contents

INTRODUCTION

Background: Combat casualty care begins at the front lines of battle and continues into rehabilitation. Current experiences in trauma care in Iraq and Afghanistan have highlighted some critical issues in combat care including the effectiveness and shelf life of blood products, the reduction of wound infections and the reconstruction of bone, tissue and facial structures. Army surgical research concentrates on issues such as hemostasis, resuscitation, bone tissue injury, soft tissue injury, trauma informatics, and clinical trauma. These six areas focus on saving the soldiers' lives, preventing viable tissue loss, and returning the soldiers back to duty as soon as medically possible.

Objective: Our goal is to use advanced bioengineering to develop technologies that will facilitate the transfer of research in musculoskeletal biology and regenerative medicine to patient care. While much is known about the basic biology of cells in the musculoskeletal system, efforts to convert this information to useful products have been limited. This is in part because the technology development teams have failed to include clinicians and engineers collaborating to ensure that the outcomes have clinical utility and the devices can be fabricated and delivered appropriately for medical applications. In addition industry involvement has typically occurred late in the technology development cycle, often requiring re-engineering before inventions can be incorporated into existing products. To avoid these pitfalls, investigators in the Center for Advanced Bioengineering for Soldier Survivability work in teams that include a clinician with experience in military medicine, bioengineers, and bioscientists with experience working closely with industry, and wherever possible, an industry partner committed to rapid transfer of the novel technologies. Our over-arching hypothesis is that if technology is developed in this manner, it will move quickly to commercialization in a form that has clinical usefulness.

Study Design: The initial problem addressed in the Center was the need for enabling technologies for reconstruction of bone and facial structures. These are composite tissues consisting of multiple components including nerve, a vascular supply, and at least one or more cell types. We have focused on three technology platforms: imaging of tissues following trauma and during healing; percutaneous stem cell delivery methods; and "smart" scaffolds to promote composite tissue repair. Of particular concern is the interaction of cells with materials and how to optimize this interaction. To achieve these goals our aims are to: (1) establish a translational research center focused specifically on enabling technologies for treatment of composite tissue injuries; (2) develop enabling technologies for delivery of musculoskeletal stem cells; (3) develop enabling technologies for intra-operative delivery of musculoskeletal stem cells in nanofiber mesh wound dressings; and (4) develop technologies for visualizing and controlling internal bleeding and scar formation. Successful attainment of these aims has been facilitated by two advisory boards: a Clinical Advisory Board consisting of surgeons with combat experience, and an Industry Advisory Board that includes senior executives from medical device companies. The achievement of these aims will move our technologies more quickly to large animal models and to the clinic (optional appropriation year).

Tasks targeted for Year 2:

Specific Aim 1. Expand the translational research center in concert with the External Advisory Board recommendations to include technologies for reconstruction of oral and maxillofacial tissues, detecting internal injuries and treating skin wounds to limit scar formation (CABSS Administration).

Task 1. Review progress in context of new developments in the field and solicit proposals.

Task 3. Identify industry sponsors for joint development projects.

Task 4. Monitor progress toward goals.

Task 5. Develop relevant animal model standards (ASTM and ISO) for testing novel technologies.

Specific Aim 2. Adapt microCT imaging technology for detecting internal bleeding following traumatic injury.

Task 2. Perform femoral artery injury model.

Task 3. Perform liver injury model.

Specific Aim 3. Adapt 3D scaffold and stem cell technology to enhance healing and control scar formation.

Task 4. Perform *in vitro* studies to characterize cellular invasion and differentiation within synthetic provisional matrices.

Task 5. Conduct *in vivo* study to determine if fibrin-inspired synthetic polymer scaffolds enhance functional dermal and epidermal repair of critically-sized full-thickness dermal excisional wounds.

Task 6. Determine the appropriate conditions for large-scale culture, decellularization, and lyophilization of stem cell embryoid body (EB) extracellular matrices (ECM).

Task 7. Modify EB-ECM with fibrin 'knobs' for targeted delivery/retention within synthetic provisional matrix.

Task 8. Perform *in vitro* studies to characterize cellular invasion and differentiation within EB-ECM modified synthetic provisional matrices.

Task 12. Develop animal model to characterize the behavior of Dabs or Dab-microgels in a complex in vivo environment.

Task 13. Perform circulation time studies

Task 14. Perform biodistribution studies

Specific Aim 4. Adapt percutaneous stem cell delivery strategies for craniofacial cartilage defect repair.

Task 6. Perform rat xyphoid defect study for microencapsulated rat ASCs and prechondrocytes.

Task 8. Determine critical size defect in rabbit ear cartilage. Surgeries will be conducted at the ISR for this part of the study.

Task 9. Perform rat xyphoid defect studies using scaffolds loaded with rat and human ASCs and prechondrocytes.

Task 10. Identify optimum microbead and scaffold delivery system.

Task 11. Characterize rabbit ear chondrocytes.

Specific Aim 5. Develop graft technologies for palate reconstruction

Task 5. Determine critical size defect size in the rat palate.

Task 6. Test palatal graft formulations in rat palate.

Specific Aim 6. Adapt stem cell delivery technology for treatment of large bone defects.

Task 4. Develop loading protocols for loading scaffolds with human ASCs with and without microencapsules.

Task 5. Evaluate different survival of stem cells with different delivery matrices in a subcutaneous model.

Task 6. Test scaffolds plus cells in the rat critical size defect model.

Specific Aim 7. Test feasibility of replacing injured or otherwise abnormal muscle with decellularized muscle.

Task 2. Determine optimal processing of decellularized muscle grafts to retain three dimensional tissue architecture and tensile strength and provide suture sites at each end.

Task 3. Use a rodent model for screening the effectiveness of decellularized muscle grafts in vivo in order to determine if decellularized muscle grafts will restore muscle structure and function.

Task 4. Determine if addition of MSCs or ASCs will improve graft effectiveness.

A Gantt chart with dates illustrates the progression of tasks and is included in the appendix.

BODY

Comments on Administrative and Logistical Matters

CABSS Leadership

In January 2013, Dr. Barbara D. Boyan accepted the position as the chair of the engineering department at Virginia Commonwealth University (VCU) and Dr. Robert E. Guldberg assumed the role of the Georgia Tech PI for this program. Dr. Boyan continues in a leadership role for the Center and the research reported. Georgia Tech is finalizing the necessary paperwork and subcontract to VCU for this work to continue. Martha Willis serves as program manager for CABSS since the departure of Maribel Baker also in January 2013.

CABSS Retreat

Our second annual CABSS Retreat was held on January 10th 2013. The CABSS Retreat consisted of the advisory board, CABSS investigators, GT faculty and graduate students. Details are provided under Aim 1 accomplishments and a copy of the meeting minutes are included in the appendix.

Key Research Accomplishments

Specific Aim 1. Expand the translational research center in concert with the External Advisory Board recommendations to include technologies for reconstruction of oral and maxillofacial tissues, detecting internal injuries and treating skin wounds to limit scar formation (CABSS Administration).

Task 1. Review progress in context of new developments in the field and solicit proposals.

The Center for Advanced Bioengineering for Soldier Survivability (CABSS) is now led by Dr. Robert Guldberg and we held our 2012-2013 Retreat on Jan 10th, 2013 with Dr. Boyan and Dr. Guldberg in attendance.   Progress reports from investigators Dr. Todd McDevitt, Dr. Ravi Bellamkonda, and Dr. Thomas Barker were given. Four new technologies were introduced to the external advisory board for review and consideration. Projects included research in post-traumatic osteoarthritis, osteoarthritis sex differences, infection-resistant biomaterials, and traumatic brain injury.   An agenda for the event is included in the appendix.

The CABSS Advisory Board members met privately following presentations. The advisory board discussion was led by retired Major General Maria Britt and she and the advisory board members provided their input to the CABSS management team. Questions the board considered include 1) What makes CABSS unique? 2) Are the problems we are addressing relevant to military medical problems? Are there gaps? 3) Are there other funding opportunities we need to leverage? and 4) What is the "way ahead" for CABSS? Minutes of the board meeting are attached in the appendix and include a more detailed discussion of these topics.

In general, the board concluded that what makes CABSS unique is the Department of Defense (DoD) focus, the brain trust, and the collaborative network that has been established. Once it was determined that leadership would continue with Dr. Guldberg at Georgia Tech and Dr. Boyan at VCU, all agreed that the CABSS name was good for "brand recognition," and that even if the mission expands, the military focus, the branding, and the collaborative team of scientists, engineers, practicing clinicians, physicians and industry are important to preserve.

Board members agreed that the focus of the center should be expanded based on the current military situation and resourcing constraints. Chronic diseases including osteoarthritis and funding from the Veteran's Administration (VA) and the National Institutes of Health (NIH) were areas to target in the future. The board agreed on the benefit of reaching out to additional funding sources to support CABSS and related projects. The VA was suggested as the major focus of future opportunities. The collaborative value of CABSS makes it unique. The interdisciplinary mix of scientists, engineers, practicing clinicians, physicians and industry is critical in seeking grant funding in the future, especially from DoD.

In terms of the "way ahead," the board concluded that the CABSS framework is working and valuable to future grant proposals. All agreed that keeping Dr. Boyan as a key leader of CABSS is important. The joint venture with Dr. Boyan at VCU and Dr. Guldberg at GT creates a strong synergy of effort. The board agreed that the focus on the military should remain, but that a shift in mission towards chronic diseases and quality of life issues would be advantageous. Seeking additional funding sources through the VA and NIH was reiterated.

Task 3. Identify industry sponsors for joint development projects.

The CABSS spin-out company, SpherIngenics, Inc. has received a Phase II SBIR grant. The proposal submitted contained a subcontract to CABSS investigator, Rene Olivares-Navarrete to perform the *in vivo* studies using an animal model of chondral defect healing developed in CABSS.

New industry collaborations include projects with Abbott Laboratories and MiMedx Group, Inc. on preclinical assessment of systemically and intra-articularly delivered

therapies for post-traumatic osteoarthritis. New collaborations will be included in CABSS activities wherever deemed appropriate.

Task 4. Monitor progress toward goals.

Quarterly reports will continue to be used to monitor progress of the funded projects. The annual progress for each project was presented on January 10th at the CABSS Retreat. As a result of research findings to date, and the pending subcontract to VCU, some of the tasks will be realigned and restated in subsequent reports.
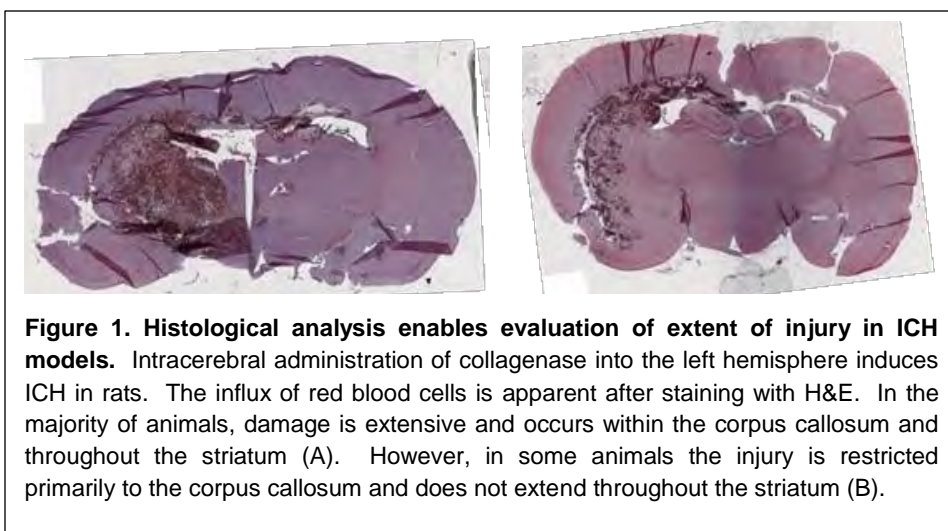
Task 5. Develop relevant animal model standards (ASTM and ISO) for testing novel technologies.

This task is being transitioned to the work to be done by Dr. Boyan's lab, at VCU. And Task 6 (administrative) will be added to "expand CABSS to include the research site at Virginia Commonwealth University focused on specific Aims 4, 5 and 7" in future reports.
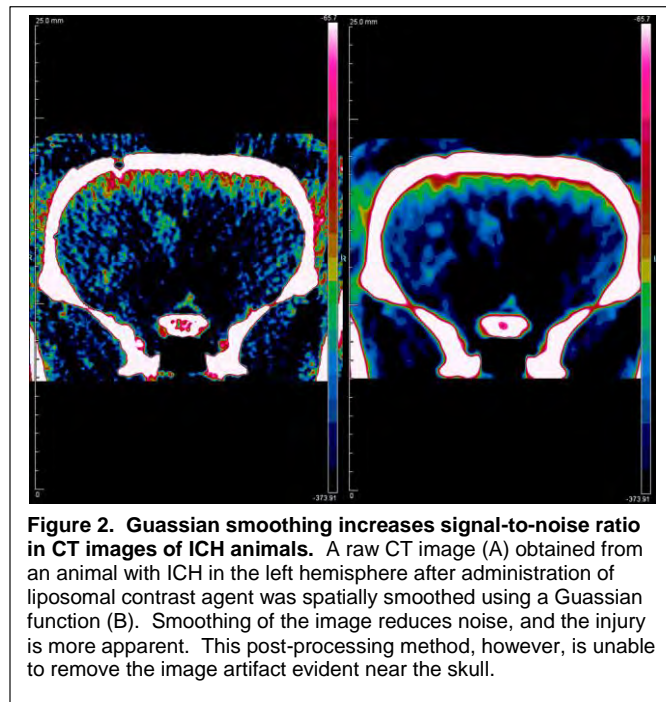
Specific Aim 2. Adapt microCT imaging technology for detecting internal bleeding following traumatic injury.

Task 2. Perform femoral artery injury model.

We have finished developing the intracerebral hemorrhage (ICH) model which will be used to test the use of microCT to non-invasively detect internal bleeding. We have successfully verified our ability to achieve reproducible injuries within rats using an intracerebral injection of bacterial collagenase. Through histological analysis, we have confirmed the influx of red blood cells into healthy brain tissue within the left hemisphere approximately 1.5 hours after the stereotaxic injection of collagenase. We have performed histological analysis of brains obtained from multiple animals after injury to determine the reproducibility of our model. The model resulted in histologically verified injury in 100% of animals tested; however, the extent of injury varied between animals (Fig. 1). We will attempt to correlate the extent of injury in each animal with CT imaging using our nanocarrier encapsulated contrast agent in subsequent imaging studies. The ability to non-invasively evaluate the extent of injury using our contrast agent will be advantageous, and this model will be suitable to test this capability.

Figure 1. Histological analysis enables evaluation of extent of injury in ICH models. Intracerebral administration of collagenase into the left hemisphere induces ICH in rats. The influx of red blood cells is apparent after staining with H&E. In the majority of animals, damage is extensive and occurs within the corpus callosum and throughout the striatum (A). However, in some animals the injury is restricted primarily to the corpus callosum and does not extend throughout the striatum (B).

In preparation for the imaging studies, we have investigated various techniques to enhance the image quality obtained from CT imaging of ICH animals. As a result, we have modified the CT imaging protocol and post image processing methods. We have investigated the use of Gaussian smoothing to remove excess noise from CT images which resulted in enhanced injury detection (Fig. 2); however, we have observed a significant artifact in the images due to the presence of the highly attenuating skull (Fig. 2, 3A). To correct for this image artifact caused by x-ray beam hardening, we have investigated the use of aluminum filters to absorb low energy x-rays while imaging an uninjured animal (Fig. 3B-D). By pre-filtering the x-ray beam, we were able to reduce the scattering artifact in the images. We will utilize this filtration method in subsequent imaging studies of ICH animals to further improve image quality.

Figure 2. Guassian smoothing increases signal-to-noise ratio in CT images of ICH animals. A raw CT image (A) obtained from an animal with ICH in the left hemisphere after administration of liposomal contrast agent was spatially smoothed using a Guassian function (B). Smoothing of the image reduces noise, and the injury is more apparent. This post-processing method, however, is unable to remove the image artifact evident near the skull.

We have completed the intracerebral hemorrhage (ICH) studies investigating our ability to detect vascular leaks non-invasively using our novel contrast agent and CT imaging. CT scans were performed on rats after induction of ICH and subsequent intravenous injection of either free contrast agent or liposomally encapsulated contrast agent. Figure 4 displays representative CT images from this study. Images from rats receiving liposomal contrast agent exhibited increased contrast at the site of ICH, whereas administration of free contrast agent did not result in any change in contrast at the injury site. Additionally, injury could not be detected in any animals prior to administration of contrast agent.
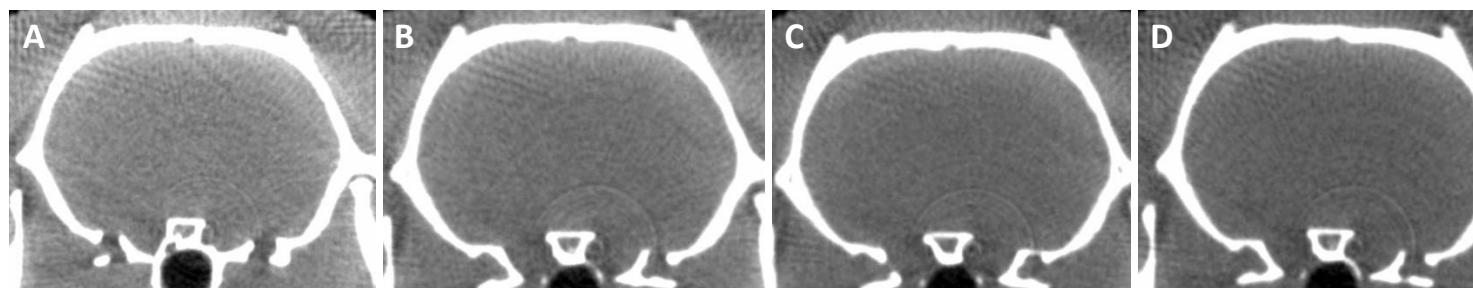
Figure 3. Aluminum filtration reduces image artifacts introduced by the skull. When no x-ray filtration method is employed, beam hardening introduces noise in the vicinity of the skull particularly at the top of the brain (A). When an aluminum filter is placed in between the subject and the x-ray source, this noise is reduced. Increased noise reduction is observed as the filter thickness is increased from

Quantitative analysis of the data obtained from rats treated with liposomal contrast agent revealed a significant increase in the voxel intensity measured within a volume of interest centered at the collagenase injection site compared to the uninjured contralateral hemisphere (Figure 4). Conversely, there was no significant difference in contrast between the 2 hemispheres in rats receiving free contrast agent. We have submitted an abstract summarizing these results for presentation at the Society for Biomaterials Annual Meeting and Exhibition. (April 2013.) We are also preparing a manuscript describing this study and our results for publication within a peer-reviewed scientific journal.
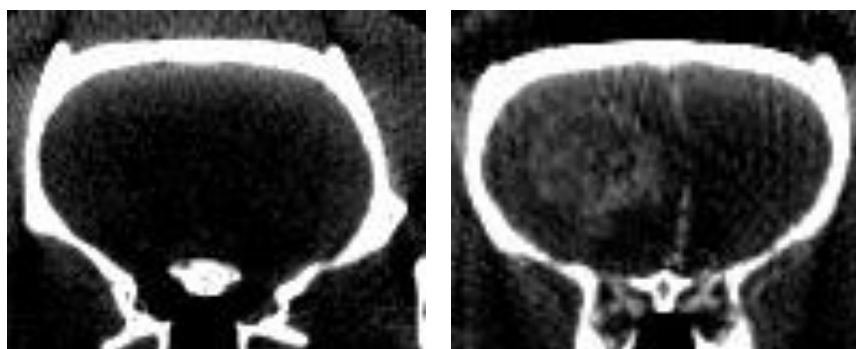
Figure 4. CT images from ICH rats after intravenous administration of free (left panel) or liposomal (right panel) contrast agent. Administration of free contrast agent did not improve ICH detection capability since there was no change in contrast at the injury site. Animals receiving liposomal contrast agent demonstrated an increase in contrast at the injury site within the left hemisphere.
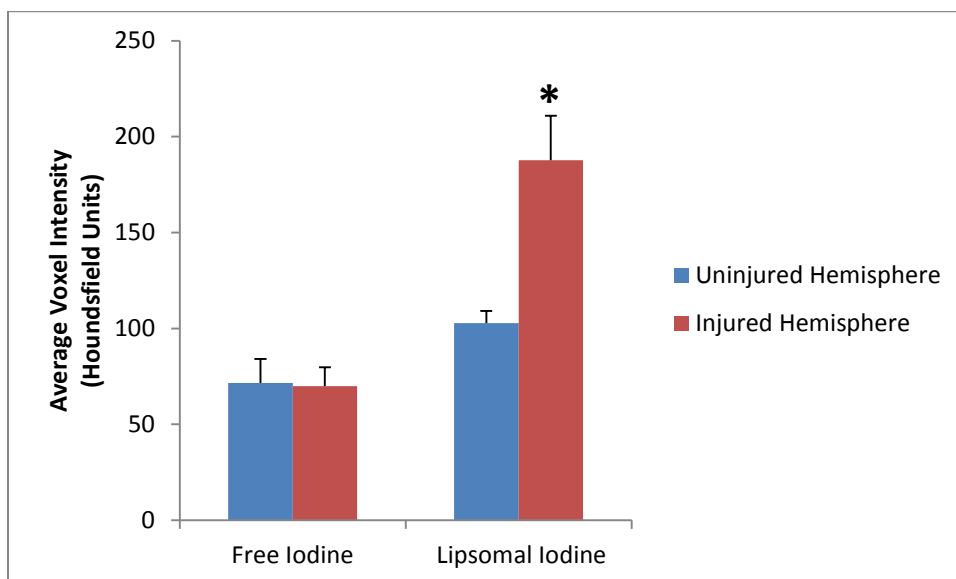
Figure 5. Quantification of CT images obtained from ICH study. Average voxel intensities within volumes of interest centered at the sites of injury were compared to average voxel intensities measured within volumes of interest centered within uninjured, contralateral hemispheres. Average voxel intensity at the injury site of animals receiving liposomal contrast agent was significantly greater than voxel intensities within the uninjured hemisphere as well as intensities measured within both hemispheres of animals treated with free contrast agent ($p < 0.05$). There was no significant difference between contrast within the uninjured and injured hemispheres of rats receiving free contast agent verifying that our liposomal agent is superior to the unencapsulated agent for detecting ICH.

CT scans performed on ICH rats after intravenous injection of free contrast agent or liposomally encapsulated contrast agent demonstrate a clear advantage to the use of liposomes as contrast agent delivery vehicles. Figure 6 displays axial, coronal, and sagittal CT images obtained from this study. Images from rats receiving liposomal contrast agent exhibited increased contrast at the site of ICH, whereas administration of free contrast agent did not result in any change in contrast at the injury site. This was confirmed in all 3 views for each animal. Three-dimensional reconstruction of the CT projections has been performed. Figure 7 displays reconstructed images from an ICH rat before (A) and after (B) administration of liposomal contrast agent. Also shown is an image from a control animal after receiving free contrast agent (Fig. 7C). Histological confirmation of injury has been performed through hematoxylin and eosin staining and anti-IgG staining for extravasated blood (Figure 8), and this data is being compared to CT scans from corresponding animals to verify a correlation between our non-invasive imaging technique and histological examination.
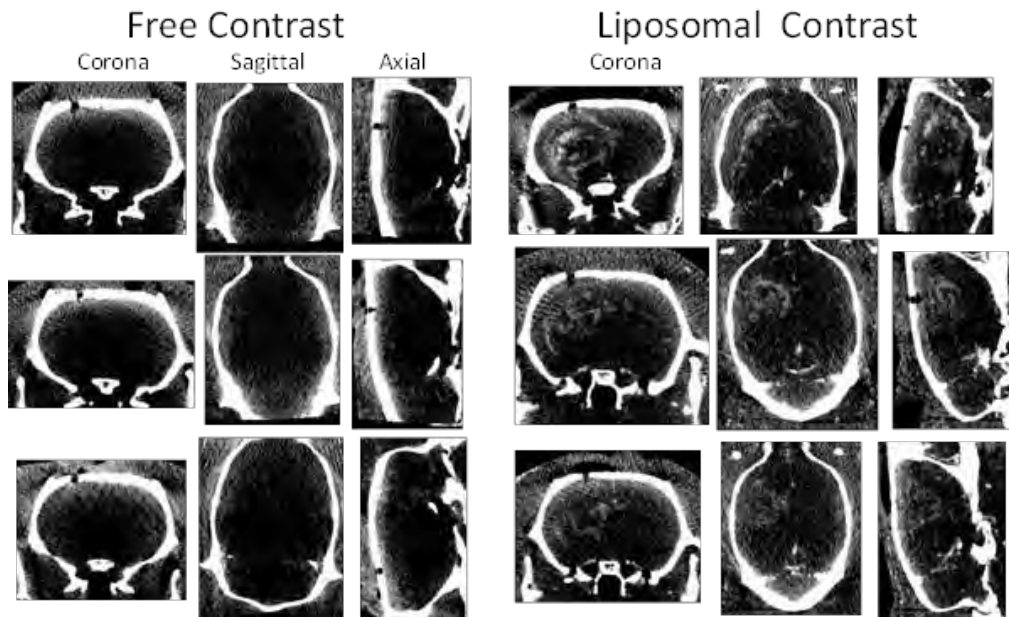
Figure 6. CT images from ICH rats after intravenous administration of free (left panels) or liposomal (right panels) contrast agent. Three CT views (axial, coronal, and sagittal) are shown for each subject (n=3 per group). Administration of free contrast agent did not improve ICH detection capability since there was no observed signal enhancement at the injury site. Animals receiving liposomal contrast agent demonstrated an increase in contrast at the injury site within the left hemisphere.
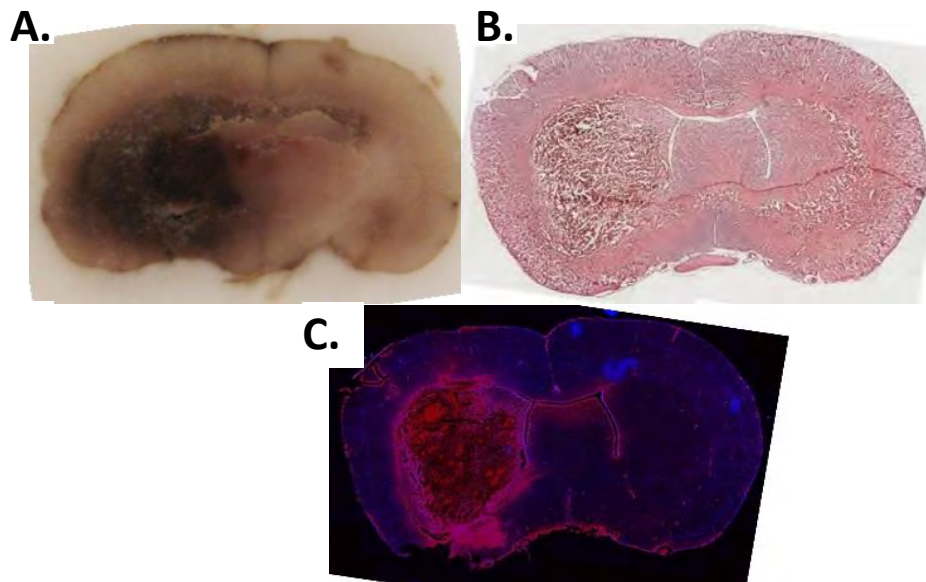
Figure 7. Three dimensional reconstructions of CT projections obtained from a rat receiving liposomal contrast agent before (A) and after (B) iv injection. Panel C displays a CT scan from an animal after receiving free CT contrast agent. Vasculature and injury to the left cerebral hemisphere is clearly present after animals are injected with liposomal contrast (B); whereas, there is no increase in signal at the injury site without the use of contrast agent (A) or after administration of free contrast agent (C).
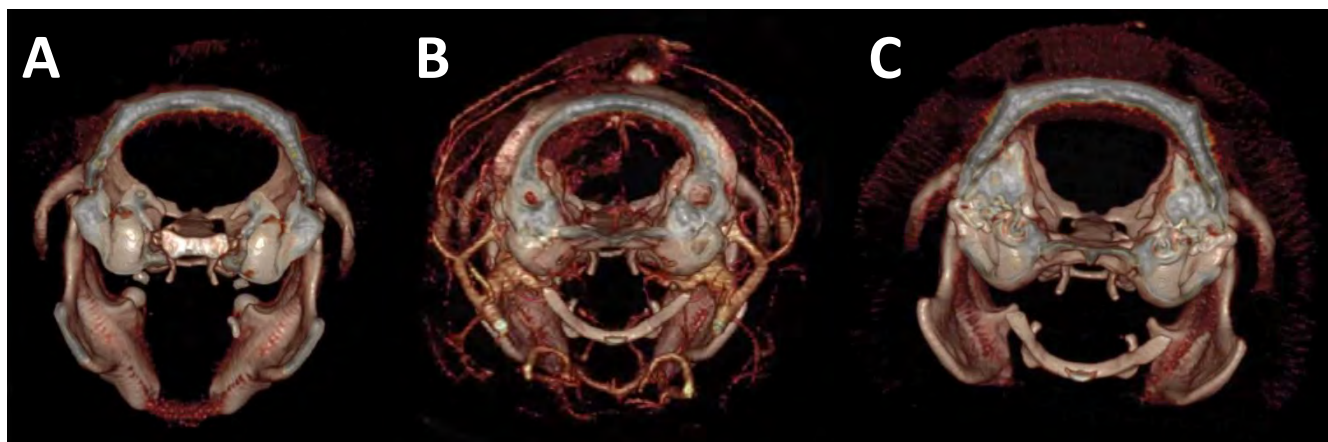
Figure 8. Immunohistochemical analysis of ICH model. After prepping and freezing injured brains for cryosectioning, a large accumulation of blood is evident at the injury site within the frozen block prep (A). H&E staining confirms the presence of ICH (B). Staining the tissue for IgGs present in the bloodstream also aids in the data validation. Panel C shows a representative brain slice from an injured animal. DAPI (blue) marks cell nuclei while anti-IgG stains (red) for bood leaks.

Task 3. Perform liver injury model

The blunt non-penetrating liver injury model in rats continues. Adult, male Fisher rats were anesthetized with isoflurane, and a 100cm length PVC tube was positioned onto the abdomen directly below the sternum. A steel punch was then dropped through the tube onto the animal. Visual assessment of injury was performed after euthanizing the animals and exposing the liver. Multiple lacerations and blood clots were apparent on the liver surface. Length and number of lacerations as well as the number of lobes affected varied between animals. We have altered the height from which the weight is dropped to further vary the extent of injury.

We have continued to develop the livery injury model in rats over the last quarter. Extent of damage is currently being investigated after subjecting anesthetized rats to a blunt non-penetrating liver injury resulting from dropping a steel punch onto the abdomen from various heights. We have been successful producing liver injury in this manner in all test rats.

We have initiated a non-penetrating liver injury by dropping a steel punch from a height of 100cm onto the abdomen of anesthetized rats. CT images of the abdomen were obtained immediately after injury. Free CT contrast agent (Visipaque) was then administered intravenously (2000mg/kg) via tail vein. Post contrast CT images were acquired immediately afterwards. Initial testing seems to indicate that free contrast agent is capable of accumulating at the injury site as demonstrated by the increase in contrast in that location (Figure 1). We aim to determine whether liposomal contrast agent will provide contrast that is more strictly confined to the injury site allowing for improved identification of the origin of injury. We will also investigate CT detection of liver injuries that are less extensive. These models will be established by dropping the punch from 25cm and 50cm heights.

Figure 9. CT scans obtained from rats after establishment of liver injury before (left) and after (right) intravenous administration of free CT contrast agent (Visipaque). Injury is not apparent in the precontrast CT scan; however, contrast is enhanced within the abdomen in animals receiving contrast agent.

Specific Aim 3.   Adapt 3D scaffold and stem cell technology to enhance healing and control scar formation.

Task 4: Perform in vitro studies to characterize cellular invasion and differentiation within synthetic provisional matrices.

In these studies, we incorporate fibrin-binding PEGylated knob peptides into fibrin matrices and then analyze their ability to enhance wound-healing properties in an angiogenesis assay.   To determine if PEGylation affects the binding capacity of knob peptides to fibrinogen, we utilized surface plasmon resonance (SPR) to characterize binding affinities of PEGylated knob peptides and native knob peptides for fibrinogen fragment D.   Next, the behavior of fibrin-PEGylated knob peptide matrices under compression was examined by bulk compression in order to determine the effect of PEGylated knob peptides on the strength and rigidity of a fibrin matrix. We then utilized a three-dimensional *in vitro* assay that uses human umbilical vein endothelial cells (HUVECs) and recapitulates the major steps of angiogenesis, including sprouting, migration, alignment, proliferation, tube formation, branching and anastomosis. Collagen beads were coated with cells and embedded in the fibrin-PEGylated knob peptide matrices to characterize cell invasion and differentiation.

In order to determine if PEGylation of knob peptides alters interactions with fibrin matrices, SPR was performed to characterize binding affinities of PEGylated knob peptides and non-functionalized knob peptides for fibrinogen fragment D. Characterizing the binding kinetics of PEGylated knob peptides provides insight into the optimal range of concentration of peptides for incorporation into fibrin matrices.

Materials and Methods: Human fibrinogen (Enzyme Research Laboratories) at 2 mg/mL was digested with 0.1 U/mL human plasmin (Enzyme Research Laboratories) in HEPES (N-2-hydroxyethylpiperazine-N_-2-ethanesulfonic acid) CaCl2 buffer (150mM NaCl, 5mM CaCl2, 25mM HEPES; pH 7.4) overnight at room temperature. Fragment D was isolated by incubating the plasmin-digested fibrinogen with GPRPAA beads at room temperature for 30 minutes, with occasional agitation. The unbound proteins and protein

fragments were removed with excessive washing with HEPES + CaCl2 buffer. Fragment D was eluted with 1M sodium bromide and 50mM sodium acetate (pH 5.3). Eluted samples were pooled together and exchanged back into HEPES + CaCl2 buffer with a centrifugal filter (molecular weight cutoff, 10,000 Da). Fragment D was verified by sodium dodecyl sulfate–polyacrylamide gel electrophoresis and stored at 80°C until use.

The Biacore 2000 (Biacore Lifesciences, GE Healthcare) was used to investigate kinetic binding constants (k_a and k_d) of knob peptide variants for fibrinogen Fragment D. Briefly, Fragment D was covalently immobilized to gold-coated SPR sensor chips via self-assembled monolayer surface chemistry to generate a nonfouling surface with a controlled density of reactive carboxylic acid groups. Mixed self-assembled monolayers were generated on gold-coated chips by incubating with a 1-mM mixture of tri(ethylene glycol)–terminated alkanethiols (HS-(CH2)11–(OCH2CH2)3–OH; ProChimia) and carboxylic acid–terminated alkanethiols (HS-(CH2)11–(OCH2CH2)6–OCH2COOH) overnight. On loading the senor chip into the Biacore 2000, the carboxylic acid–terminated alkanethiols in all 4 flow cells was activated by flowing 200mM 1-ethyl-3-(3-dimethylaminopropyl) carbodiimide (Sigma- Aldrich) and 50mM N-hydroxysuccinimide (Sigma-Aldrich; 5 µL/ minute for 10 minutes). Immediately after activation, Fragment D was immobilized in 3 flow cells (5 µL/minute for 10 minutes) to achieve 1800 to 2000 resonance units (1 resonance unit ~1 pg/mm2). Unreacted N-hydroxysuccinimide groups were quenched in all 4 flow cells (3 sample cells and 1 reference cell) with 20mM ethanolamine (10 µL/minute for 10 minutes). On stabilization of the baseline signal, kinetic binding experiments were run in duplicate with the peptide variants as the flow analytes. Five various concentrations for each peptide (ranging from 5µM to 1.5mM, with specific concentrations optimized for each peptide analyzed) were flowed at 25 µL/minute for 4 minutes immediately followed by a 5-minute dissociation phase. Between each run, the surface was regenerated with 1M sodium bromide and 50mM sodium acetate (pH 6.0).

SPR sensorgrams were analyzed with the aid of Scrubber 2 and ClampXP software (Center for Biomolecular Interactions Analysis, University of Utah). Before analysis, all sensorgrams were inspected for abnormalities (i.e., baseline drift, air spikes, or irregular deviations) and excluded. Reference cell responses were subtracted from corresponding active response curves. Double-referenced curves were acquired by further subtracting the reference cell blank buffer injections from each reference subtracted response curve. All double-referenced curves were normalized by the molecular weight of each peptide and multiplied by 1000 to account for minor variations in response because of molecular weight. The resulting curves were then analyzed and fitted to the kinetic models. Kinetic modeling and simulations were performed with ClampXP software with the Langmuir 1:1 model or the heterogeneous ligand model; globally fitted parameters were determined for each kinetic dataset per peptide. Equilibrium binding constants were calculated from fitted kinetic constants. Goodness of fit for each model was determined by evaluating the residual plots and residual sum of squares.

The binding capacities of "A" knob peptide, GPRPFPAC, "B" knob peptide, AHRPYAAC, non-binding peptide, GPSPFPAC, and their respective PEGylated peptides to fragment D were determined by plotting the maximum response observed at various concentration for each sample (Figure 10). As expected, the "A" knob peptide exhibited the highest binding affinity for fragment D, followed by the "B" knob peptide and then the non-binding control. In general, PEGylation was found to slightly decrease the binding capacity of knob peptides for fragment D. However, the relative order of binding affinities were maintained; "A" knob > "B" knob > non-binding peptide.
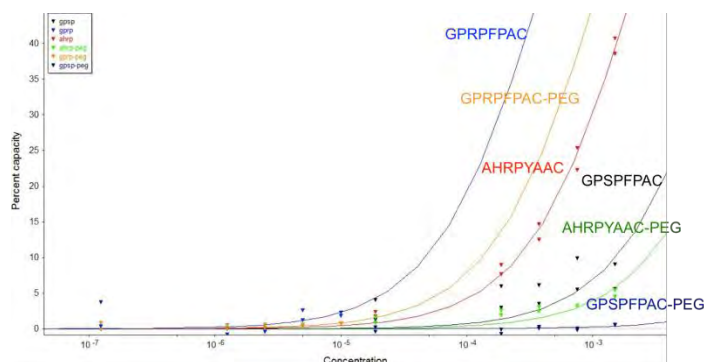
Figure 10. Maximum knob peptide binding capacity to immobilized fibrinogen fragment D. The binding capacities of "A" knob peptide, GPRPFPAC, "B" knob peptide, AHRPYAAC, non-binding peptide, GPSPFPAC, and their respective PEGylated peptides to fragment D were analyzed through SPR. As expected, the "A" knob peptide exhibited the highest binding affinity for fragment D, followed by the "B" knob peptide and then the non-binding control. In general, PEGylation was found to decrease the binding capacity of knob peptides for fragment D.

Experimental SPR curves were then fit to a Langmuir 1:1 model or a 2-site heterogeneous ligand model to determine the association and dissociation rates (ka and kd, respectively) for each peptide variant. Goodness of fit was analyzed by the residual sum of squares (RSS), which characterizes the difference between the experiment values and the fitted curves. A lower RSS corresponds to a better fit, and in general, this value should be below 10% of the maximum binding response. The RSS was evaluated for all knob peptide variants for both the Langmuir 1:1 model as well as the 2-site model. "A" knob and "B" knob non-functionalized peptides and their PEGylated counterparts best fit a 2-site model, while the non-binding control only converged when fit to the Langmuir 1:1 model. Binding to fragment D was only observed for the native non-binding peptide and the PEGylated version at high (mM) concentrations, which is likely due to nonspecific interactions. Previous reports characterizing the affinity of "A" knob for fragment D also reported a 2-site binding model; fragment "A" is known to bind both the "A" and "B" binding pocket of fragment D, and our calculated parameters are in good agreement with those previously reported. The binding affinities of the "B" knob have not been previously reported, however, the "B" knob is thought to only bind the "B" pocket of fragment D. Examination of the fitted parameters for the 2-site model of the "B" knob demonstrate one higher affinity reaction and one lower affinity reaction, with these values being two orders of magnitude apart for the PEGylated "B" knob. It is likely that the higher affinity reaction represents the "B" knob binding to the "B" pocket, whereas the lower affinity reaction could correspond to nonspecific binding. The experimental sensorgrams and their respective best fits are shown below in Figure 11. The fitted parameters (Bmax, ka, and kd) for each knob peptide variant are displayed in Table 1. These results indicate that, at a minimum, micromolar concentration of PEGylated knob peptides are required to effectively bind to fibrinogen. We therefore utilized equimolar concentrations of peptides and fibrinogen for subsequent studies.

15

	B	B*	kfwd	krev	kfwd*	krev*	RSS	KD1	KD2
GPRPFPAC	7.365	18.66	10538	9.31E-03	42.21	1.58E-04	1.526	**8.84E-07**	3.74E-06
GPRPFPAC-PEG	6.65	8.949	38729	0.02847	77.15	1.95E-03	1.505	**7.35E-07**	2.52E-05
AHRPYAAC	16.06	99.39	99.45	3.02E-03	1.81E+00	1.45E-04	2.30	**3.03E-05**	8.01E-05
AHRPYAAC-PEG	20.36	17.16	287.4	0.5032	4.518	2.59E-04	0.7292	**1.75E-03**	5.72E-05
GPSPFPAC	38.2		4.85	8.80E-04			2.664	**1.81E-04**	
GPSPFPAC-PEG	14.59		0.7367	2.14E-04			0.7466	**2.90E-04**	

Table 1: Fitted parameters. B and B* indicates maximal binding capacity of Fragment D in resonance units; kfwd, association rate; krev, dissociation rate; RSS, residual sum of squares. Calculated KD from fitted ka and kd values in which KD=kd/ka.

Under normal conditions, angiogenesis plays a significant role during wound healing. Fibrin is one of the major structural proteins involved in the provisional matrix during wound healing and is thus a suitable substrate for an angiogenesis model. *In vivo* angiogenesis involves endothelial cells (EC) undergoing several morphologic transitions and changes in gene expression profile, and the process can be thought of as a series of steps, including degradation of the basement membrane by secreted proteases, migration (sprouting) of the EC, alignment, proliferation, lumen formation, branching, and anastomosis. The assay described here is a particularly powerful tool, because most of the fundamental processes of angiogenesis are faithfully reproduced: basement membrane is degraded before sprouting of single EC; migration and proliferation of EC occur; lumen formation proceeds by the same process as has been demonstrated *in vivo*; and, in addition, microvessels branch and anastomose.

In the clinical setting, fibrin concentrations in the physiological range that allow for acceptable cell growth and matrix remodeling are very difficult to handle. In order to enhance handleability, high protein concentrations are used to yield more rigid gels, but the ability of cells to grow in and remodel these matrices is hindered. Extracellular matrix compliance and density have been shown to regulate capillary angiogenesis but the mechanisms remain unclear. By incorporating PEGylated knob peptides into a fibrin matrix, and thereby altering the polymerization mechanics, the goal was to enhance the mechanical strength and handleability of a fibrin matrix but at lower protein concentrations that would allow for improved angiogenic properties. The young's modulus of fibrin-PEGylated knob peptide microgel gels was measured by uniaxial compression.

A Bose EnduraTEC™ ELF 3200 Uniaxial Testing System (Bose Corporation ElectroForce, Eden Prairie, MN) was used to perform compression tests on a range of fibrin clot concentrations (2-8mg/mL) containing an equimolar ratio of one of three synthetic PEGylated peptides ('A' knob peptide GPRPFPAC-PEG; 'B' knob peptide AHRPPYAAC-PEG; and a non-binding scrambled peptide GPSPFPAC-PEG. Clots were polymerized with 1U/mL thrombin in 137.5 mM Trise HCl + 50 mM NaCl and 5 mM CaCl2 (TSBC) buffer for 1 hour in a silicone mold prior to taking measurements. The silicone mold consisted of two layers of a CoverWell™ perfusion chamber gasket (Invitrogen, Frederick, Maryland), 9mm in diameter and 2.5mm deep, with the final dimensions of the samples being 9mm in diameter and 5mm in height. Strain at 10, 20, 30, 40, 50, and 60% were applied at 1Hz and all experiments were conducted at room temperature, with each condition being tested with at least 5 samples. The young's modulus at each fibrinogen concentration was calculated and recorded for each condition.
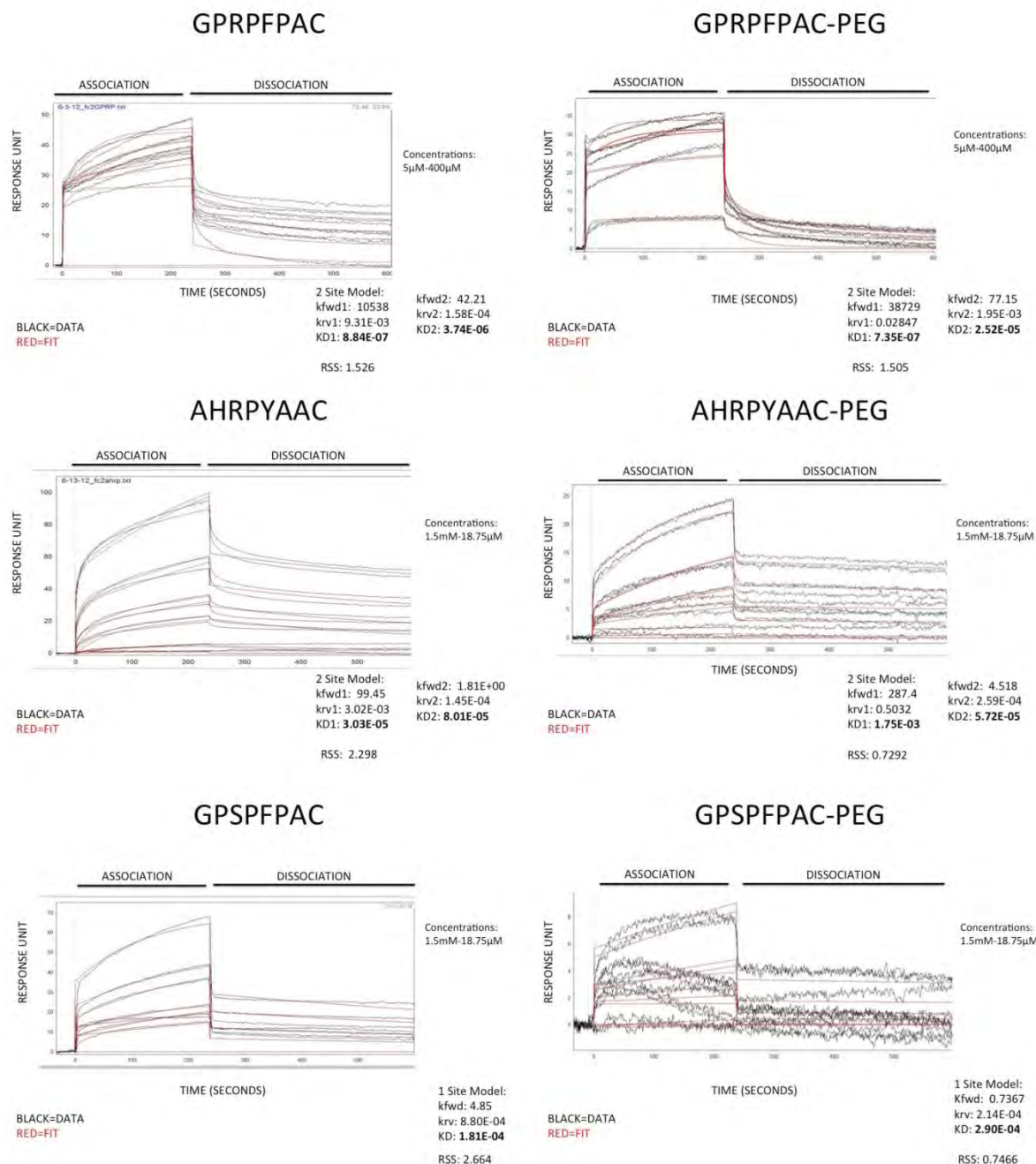
GPRPFPAC

Concentrations: 5µM-400µM

2 Site Model:
kfwd1: 10538
krv1: 9.31E-03
KD1: **8.84E-07**

kfwd2: 42.21
krv2: 1.58E-04
KD2: **3.74E-06**

BLACK=DATA
RED=FIT

RSS: 1.526

GPRPFPAC-PEG

Concentrations: 5µM-400µM

2 Site Model:
kfwd1: 38729
krv1: 0.02847
KD1: **7.35E-07**

kfwd2: 77.15
krv2: 1.95E-03
KD2: **2.52E-05**

BLACK=DATA
RED=FIT

RSS: 1.505

AHRPYAAC

Concentrations: 1.5mM-18.75µM

2 Site Model:
kfwd1: 99.45
krv1: 3.02E-03
KD1: **3.03E-05**

kfwd2: 1.81E+00
krv2: 1.45E-04
KD2: **8.01E-05**

BLACK=DATA
RED=FIT

RSS: 2.298

AHRPYAAC-PEG

Concentrations: 1.5mM-18.75µM

2 Site Model:
kfwd1: 287.4
krv1: 0.5032
KD1: **1.75E-03**

kfwd2: 4.518
krv2: 2.59E-04
KD2: **5.72E-05**

BLACK=DATA
RED=FIT

RSS: 0.7292

GPSPFPAC

Concentrations: 1.5mM-18.75µM

1 Site Model:
kfwd: 4.85
krv: 8.80E-04
KD: **1.81E-04**

BLACK=DATA
RED=FIT

RSS: 2.664

GPSPFPAC-PEG

Concentrations: 1.5mM-18.75µM

1 Site Model:
Kfwd: 0.7367
krv: 2.14E-04
KD: **2.90E-04**

BLACK=DATA
RED=FIT

RSS: 0.7466

Figure 11. Experimental SPR curves and fits. Bmax indicates maximal binding capacity of fragment D in resonance units; kfwd, association rate; krev, dissociation rate; RSS, residual sum of squares. Calculated KD from fitted ka and kd values in which KD=kd/ka.

HUVECs and Fibroblasts were grown in M199 supplemented with 10% fetal bovine serum (FBS) (GIBCO, Carlsbad, CA) and endothelial cell growth supplement (ECGS) (BD Biosciences, Bedford, MA) at 37C and 5% CO_2. Media is changed to EGM-2 (Clonetics, Walkersville, MD) the day before beading for HUVECs and the day before embedding for

17

fibroblasts. Cytodex 3 microcarrier beads (Amersham Pharmacia Biotech, Piscataway, NJ) are used for coating. Beads are washed in EGM-2 medias 3 times. HUVECs are trypsinized 1 million collected and mixed with 2500 beads (a 400 cell: bead ratio) in 1.5mL of EGM-2 media. This mixture is placed at 37C and 5% CO2 and incubated for 4 hours inverting and mixing every 20 min. The coated beads are then transferred to a T25 culture flask and incubated overnight in 5mL of EGM-2.

To embed the coated beads in fibrin, the coated beads are collected and washed 3x with EGM-2 and suspended in the fibrinogen solution at a concentration of 500 beads/mL. Fibrinogen solutions at concentrations from 2-8mg/mL containing an equimolar ratio of one of three synthetic PEGylated peptides ('A' knob peptide GPRPFPAC-PEG; 'B' knob peptide AHRPPYAAC-PEG; and non-binding peptide GPSPFPAC-PEG) in 137.5 mM Tris HCl + 50 mM NaCl 0.15U/mL Aprotinin and 5 mM $CaCl_2$ (TSBC) buffer were used. 1U/mL thrombin was added to the bottom of a well of a 96 well plate and 100µL of the fibrinogen/bead mixture was mixed with the thrombin to polymerize. The fibrin clots were incubated for 1 hour at 37C. EGM-2 media was then added to each well with 5,000 fibroblasts. Media was changed every day. Angiogenic growth was assessed by analysis of serial light microscopic images every 24h for 7 days.

Observing the young's modulus calculated for each fibrinogen concentration, the inclusion of the 'B' knob PEGylated peptide appears to increase the mechanical strength of the fibrin clot compared to the 'A' and non-binding control PEGylated peptide included clots. These results show that for higher fibrin concentrations, the effect is multiplied.
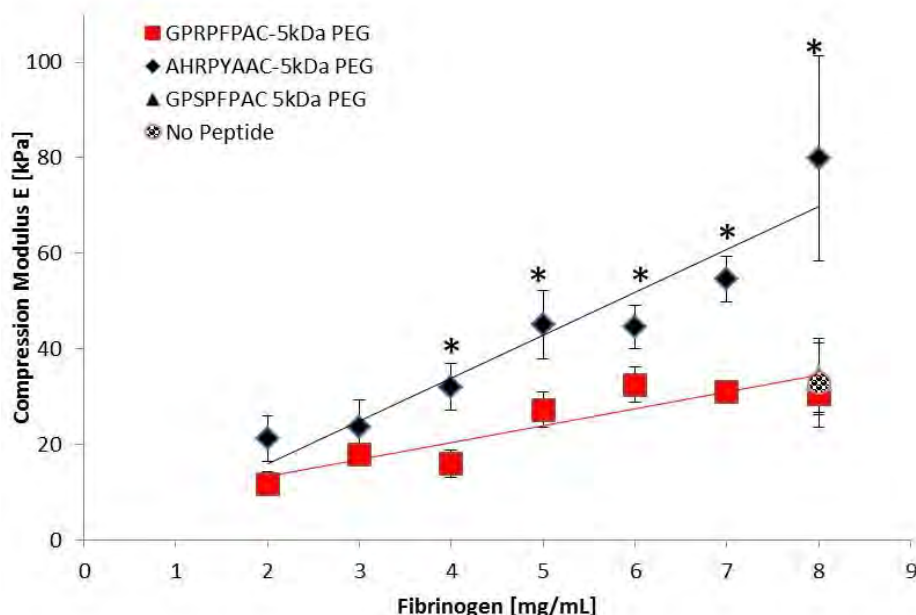
Figure 12. Bulk compression testing of fibrin/PEGylated knob peptides. 'B' knob AHRPYAAC PEGylated peptide (black) had a significantly increased compression modulus compared to 'A' knob GPRPFPAC PEGylated peptide (Red) and GPSPFPAC and No peptide control fibrin clots (triangle and circle, respectively) over a 4-8 mg/ml fibrin concentration range. (*; $P<0.05$). Error bars = SEM.

Below are serial light microscopy images of the HUVEC coated beads embedded in fibrin/PEGylated knob peptide clots. Images were taken with a Nikon Eclipse Ti microscope with a 10x lens every 24 hours. We have shown that these cells outgrow into the matrix up to 20 mg/mL, whereas 40 mg/mL fibrin concentration inhibits outgrowth independent of the inclusion of the PEGylated knob peptides.
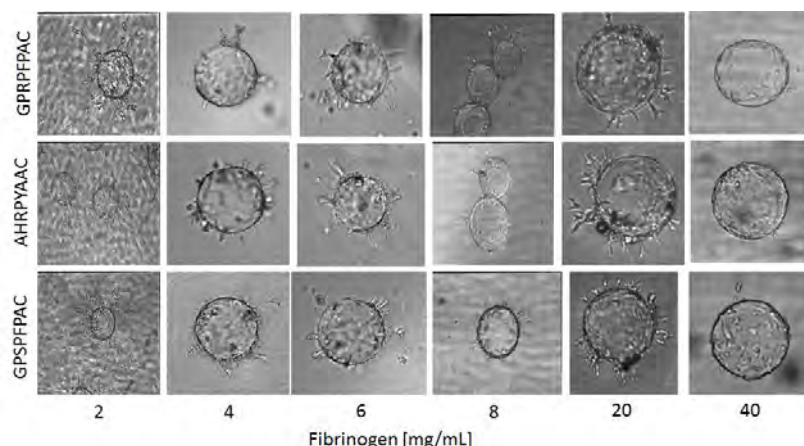

Figure 13. Serial light microscopy images of angiogenic outgrowth over a 2-40 mg/mL fibrin. concentration.

The inclusion of the 'B' knob PEGylated peptide enhanced the mechanical strength at a similar protein concentration compared with the 'A' and non-binding control knob peptides. Results show that all PEGylated knob peptides had similar angiogenic growth into fibrin clots with equivalent compression moduli. Thus we were able to increase mechanical strength and handleability of a fibrin matrix with the inclusion of the 'B' knob PEGylated peptide without hindering the ability of cells to grow in and remodel these matrices.

We are currently in the process of quantifying cell differentiation at various concentrations of fibrin/PEGylated knob peptide clots. Previous studies have shown that HUVECs take on a more microvascular phenotype as they undergo angiogenic sprouting in the gels, switching their gene expression profile from one that mimics large vessel venular EC to one that matches microvascular EC. Similarly, cell phenotypes of tip cells vs. stalk cells can also be elucidates with this approach.
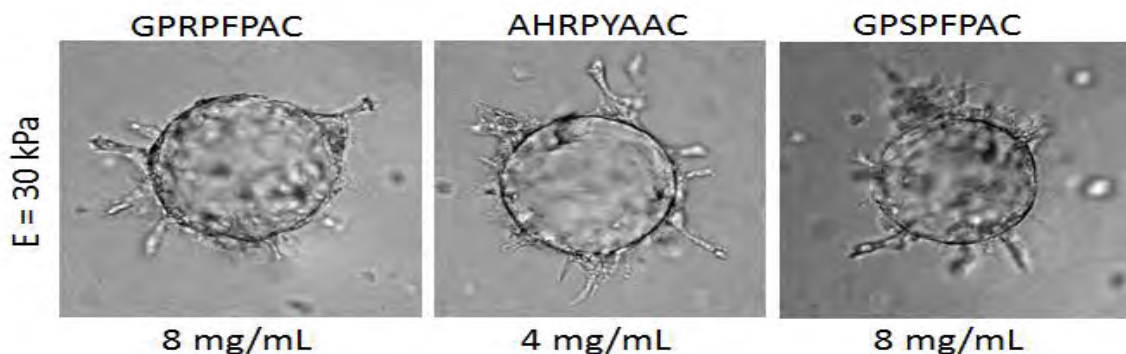
Figure 14. Angiogenic outgrowth at equivalent compression moduli.

Task 5: Conduct in vivo study to determine if fibrin-inspired synthetic polymer scaffolds enhance functional dermal and epidermal repair of critically-sized full-thickness dermal excisional wounds.

Preliminary *in vivo* studies were conducted using non-modified EB-ECM with fibrin vehicle controls.

Task 6: Determine the appropriate conditions for large-scale culture, decellularization, and lyophilization, of stem cell embryoid body (EB) extracellular matrices (ECM).

Mouse embryonic stem cells (ESCs; D3 cell line) were initially expanded on a feeder layer of mouse embryonic fibroblasts and were subsequently cultured feeder-free for several passages on 0.1% gelatin-coated 150 mm polystyrene cell culture dishes (Corning) with Dulbecco's modified eagle medium (Mediatech), supplemented with 15% fetal bovine serum (HyClone), 2 mM L-glutamine (Mediatech), 1x MEM non-essential amino acid solution (Mediatech), antibiotic/antimycotics (Mediatech), and 0.1 mM β- mercaptoethanol (MP Biomedicals, LLC). Undifferentiated cells were expanded prior to EB formation in the presence of 10^3 U/mL leukemia inhibitory factor (LIF) (ESGRO), which was added to the culture media upon each re-feeding. Cells were passaged every two to three days before reaching ~70% confluence. To initiate EB culture, ESCs were trypsinzed from the gelatin-coated dishes using 0.05% Trypsin/0.53 mM EDTA (Mediatech) and introduced into AggreWell™ 400 templates (Stem Cell Technologies) at a density of $6x10^6$ cells in 3 mL differentiation media (ESC media without LIF) to form 1000 cell EBs (~ 6000 microwells). After allowing the cells to initially settle in the insert wells, the multi-well plates were centrifuged for 5 minutes at 200xg. After 24 hours of culture, EBs were transferred from the AggreWell™ to rotary suspension culture with ~2000 EBs cultured in 100 mm bacteriological grade polystyrene Petri dishes (Corning) with 10 mL of differentiation media. EB suspension cultures were maintained on rotary orbital shakers (Barnstead Lab-Line, Model 2314) at 40 rpm at 37°C in 5% CO_2 for the entire duration of suspension culture. Previous work from our lab has demonstrated that rotary orbital suspension culture methods result in greater yields of homogeneous populations of EBs while preventing agglomeration of the 3D cell aggregates.

EBs were cultured in suspension for up to 12 days and re-fed every other day after collecting independent EB cultures via gravity-induced sedimentation in 15 mL conical tubes. Two different culture conditions were compared – serum-containing EB differentiation media (+serum) versus serum-free ESGRO media. The components of serum-containing media included Dulbecco's modified eagle medium, supplemented with 15% fetal bovine serum, 2 mM L-glutamine, 1x MEM non-essential amino acid solution, antibiotic/antimycotics, and 0.1 mM β- mercaptoethanol. The serum-free media used was ESGRO Complete media (Millipore). Spent media was aspirated, and the cultures were replenished with 10 mL of fresh differentiation media before being placed back in the Petri dishes and returned onto the rotary orbital shakers.

RNA was extracted from undifferentiated ESCs (day 0) and from EBs cultured in both +serum and ESGRO media on days 6, 9, and 12 of rotary culture utilizing the RNeasy Mini Kit (Qiagen) and analyzed on the NanoDrop spectrophotometer (NanoDrop) for concentration and purity at 260 nm and 280 nm. Complimentary DNA was reverse transcribed using 1 µg of total RNA in conjunction with the iScript cDNA synthesis kit (BioRad) on the iCycler Thermal Cycler (Bio-Rad). Quantitative RT-PCR was performed using SYBR Green with the MyIQ cycler (BioRad). Primer sets were designed using Beacon Designer software for housekeeping gene glyceraldehyde-3-phosphate dehydrogenase (Gapdh), as well as bone morphogenic protein-4 (Bmp-4), fibroblast growth

factor-2 (Fgf2), insulin-like growth factor-2 (Igf2), and vascular endothelial growth factor-A (Vegfa).

During EB feedings at days 9 and 12, conditioned media from both +serum and ESGRO cultures was collected. After 48 hours of conditioning, EBs were collected by gravity-induced sedimentation and the EB-CM (~10 mL) was transferred to a fresh conical tube. The spent media was centrifuged for 5 minutes at 10,000 RPM at 4°C to remove cellular debris and the supernatant fraction was transferred to a new 15 mL conical tube and stored at -20°C prior to further analysis.

Proteins were extracted from lyophilized EB matrices (EBM) from later days of differentiation (day 9 and day 12) using tissue protein extraction buffer (TPER, Thermo). TPER buffer is mild enough that proteins can be assessed using immunoassays. For both TPER and serum-free media EBM extractions, each lyophilized EBM sample was obtained from a single plate of EBs (~2500 EBs) and extracted with 500 □L of TPER buffer with rotation for two hours at room temperature. Before EBM protein analysis was performed, all samples (n=6 per group) were centrifuged to remove insoluble matrix for 5 minutes at 14,000 RPM at room temperature. Specific growth factors, including BMP-4, IGF-2, FGF-2, and VEGF-A, extracted from the EBM were quantified using enzyme-linked immunosorbent assays (ELISAs) obtained from R&D Systems.

The gene expression of several growth factors known to be involved in muscle regeneration and angiogenesis were differentially expressed in EBs cultured in +serum compared to ESGRO media.   Genes of growth factors involved in angiogenesis, including Bmp4, Fgf2, and Vegfa, were expressed at similar levels if not higher, in EBs cultured in ESGRO compared to +serum.   Igf2, a growth factor known to stimulate muscle regeneration, was expressed at similar levels at earlier days of differentiation (days 6 and 9) but was increased by day 12 in +serum EBs.
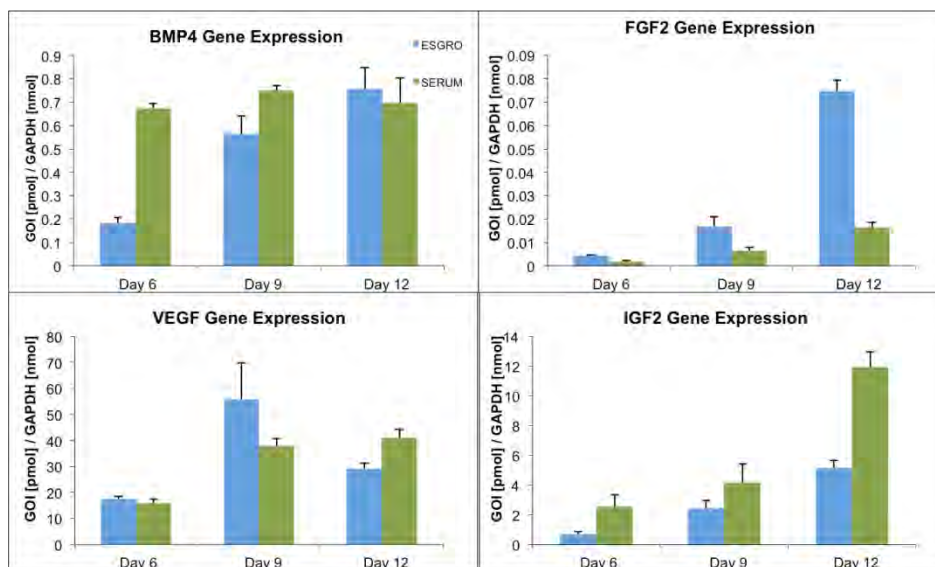

Figure 15. Growth factor gene expression comparison between ESGRO-
and +serum-cultured embryoid bodies during differentiation time. Sample
size n = 6, mean ± standard deviation.

Growth factor proteins generated by EBs during differentiation were quantified in the matrix associated fraction (EB matrix) over differentiation time. Following protein extraction from EBM with TPER buffer, the same four growth factors previously analyzed for gene expression and soluble protein content were examined. At both 9 and 12 days, the amount of BMP4 and FGF2 extracted from ESGRO EBM and +serum EBM was similar between the treatment groups. However, the differences in specific protein content were evident in the VEGFA and IGF2 proteins. The ESGRO EBM exhibited higher levels of VEGFA in the TPER extraction compared to +serum EBM. On the other hand, IGF2 content was higher in +serum EBM extraction compared to ESGRO EBM extractions, which appeared to increase at day 12 compared to day 9.

Overall, the culture conditions exhibited differences in the growth factor gene expression and in turn resulted in the differential protein expression secreted by the EBs as well as the protein associated with the matrix. These differences will aid in determining the conditions in which EBs will be cultured to further the development of 3D scaffolds to aid in composite tissue repair.n order to obtain a more global view of the growth profile differences between the two EB culture conditions, SuperArray analysis will be performed over samples collected during differentiation. This array analysis will further aid in assessing which growth factors are being differentially expressed, particularly ones that stimulate tissue repair, and ultimately determining the treatment condition and time point at which stem cell matrix should be utilized for 3D scaffold implementation.
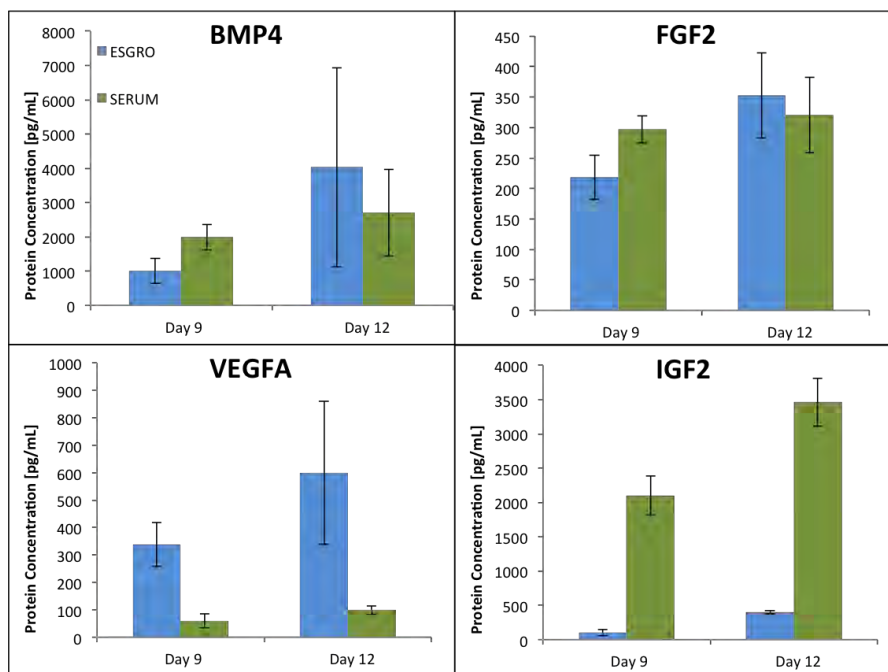
Figure 16. Matrix-associated growth factor protein comparison between ESGRO- and +serum EB matrices during differentiation time. Sample size n = 6, mean ± standard deviation.

Task 7: Modify EB-ECM with fibrin 'knobs' for targeted delivery/retention within synthetic provisional matrix.

Mouse embryonic stem cells (D3 line) were cultured in monolayer and embryoid bodies were formed as outlined above in task 6. After 10 days culture, EB plates were combined to yield ~4000 EBs per conical tube and were harvested by gravity-induced sedimentation. Collected EBs were washed 2X with 1X PBS and 2X with ultrapure water and placed at -80°C overnight. After complete freezing, EBs were lyophilized for 48 hours and subsequently stored at -20°C in dessicating conditions. Planned quality control assays including measuring DNA content, cell viability, and endotoxin screening, and will be performed before introducing the fibrin knob modification.
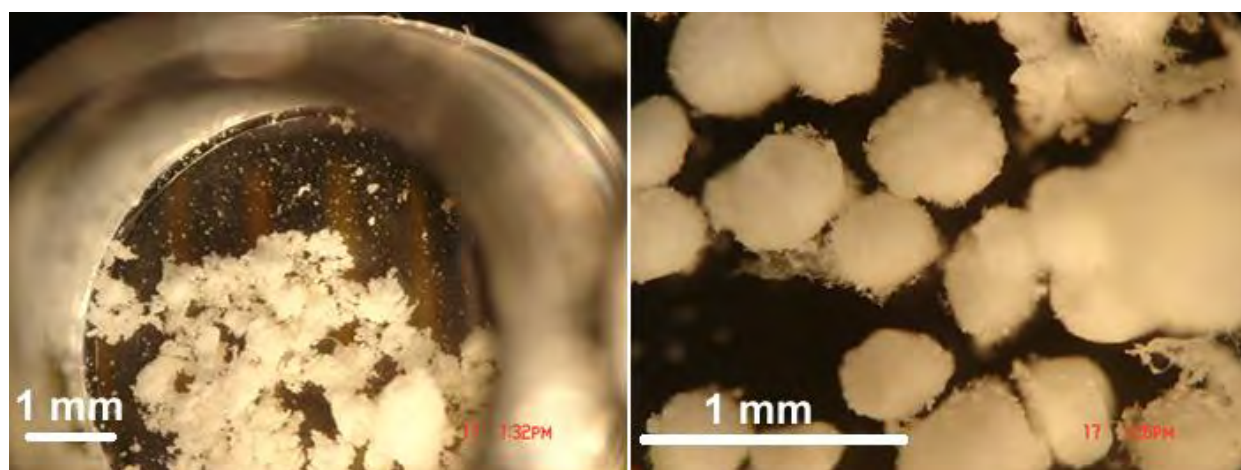
Figure 17. EB-ECM obtained from mouse embryonic stem cell aggregates.

EB-ECM has been obtained (figure 17) and has been given to the Barker lab for fibrin-knob modification. Based on our results to date, it may be necessary to restructure some of these Aim 3 tasks (specifically the remainder of 7 and12 through 14) next quarter.

Task 8: Perform *in vitro* studies to characterize cellular invasion and differentiation within EB-ECM modified synthetic provisional matrices.

Tasks 5 through 9 were originally added in order to determine if a fibrin knob delivery of the EB-ECM would improve its effectiveness. The original EB-ECM was obtained using chemical decellularization techniques, resulting in a highly viscous product that was difficult to administer and was not always retained within the wound bed following treatment. It was for this reason that the fibrin delivery vehicle was considered. At this point in our research, we have determined that EB-ECM obtained using a mechanical decellularization technique is preferable. This technique has resulted in an easily manipulated powder that is easily retained in the wound bed consequently eliminating the need for any delivery vehicle. Additionally we have shown that EB-ECM obtained via

mechanical decellularization retains more ECM and growth factors and unlike the original EB-ECM, it is made from entirely serum-free culture. Taken together, these protocol changes should produce a more uniform EB-ECM, free of xenogeneic components that can be more effectively administered in the *in vivo* wound environment.

Based on these results, we will conduct no further *in vitro* studies using fibrin controls, thus Task 5 and 8 are now completed. Task 9, to conduct *in vivo* studies to determine if the effect of the co-delivery of targeted EB-ECM nanoparticles with fibrin-inspired synthetic polymer scaffold will be modified slightly. This task has begun and will be conducted using the EB-ECM obtained using mechanical decellularization. As a part of this task, we will determine if the EB-ECM enhances functional dermal and epidermal repair of crucially sized full thickness dermal excisional wounds in both an acute wound mouse model (C57B1/6 mice) and in a chronic wound mouse model (stz mice).

Task 11: Apply for IACUC and ACURO approval for characterization of in vivo safety of fibrin-microgel hybrids

This task was completed in November 2012.

Task 12: Develop animal model to characterize the behavior of Dabs or Dab-microgels in a complex in vivo environment.

Task 13: Perform circulation time studies

Task 14: Perform biodistribution studies

Tasks 12, 13 and 14 have been refined and will focus on the evaluation of the use of Dabs and Dab-microgels for the detection and augmentation of clotting.

First generation fibrin binding technologies utilized fibrin knobs to engage fibrin matrices. While these knobs are useful for altering fibrin matrices, the alterations observed are nuanced and *in vitro* experiments indicate that these small changes in fibrin properties do not result in large scale enhancement angiogenic responses. Knob peptides bind fibrin with affinities in the micromolar range, however, higher affinity binding is likely required for gross alterations in fibrin matrix properties and subsequently large scale improvements in cellular responses. In order to identify fibrin-binding moieties with greater affinity and specificity for fibrin, we evolved humanized synthetic single chain variable fragment (scFv) antibodies with high affinity for fibrin utilizing two phagemid libraries in biopanning assays against fibrin. We identified several clones with affinities for fibrin in the nanomolar range. We utilized these superior fibrin-targeting motifs to create second-generation fibrin-binding microgel technologies for engagement of fibrin matrices.

While the initial goal was to utilize these fibrin-targeting microgel technologies for modification of EB-ECMs, initial characterization experiments in which fibrin-binding microgels were included during clot formation demonstrated a significant affect on clot augmentation. These exciting results warranted further investigation, therefore our focus shifted to further characterizing augmentation of clotting in the presence of our fibrin-binding microgels. Furthermore, data from Dr. McDevitt's group indicated that their novel method of EB-ECM generation retains more ECM and growth factors than the original EB-ECM and can be produced as an easily manipulated powder that is easily retained in the wound bed, consequently eliminating the need for any delivery vehicle. Because a fibrin delivery vehicle is no longer needed as a delivery vehicle for EB-ECMs we are no longer integrating these technologies. Therefore, this aim has been restructured to characterize

the ability of our fibrin binding microgels to augment clotting and act as synthetic platelets. We are characterizing augmentation of clotting in the presence of fibrin-binding microgels in a series of *in vitro* assays and through an *in vivo* femoral vessel injury model. Because these fibrin binding scFvs have the potential to interact with endogenous fibrin, we are also utilizing an *in vivo* rat pulmonary embolism model to evaluate the interactions of Dabs and Dab-microgels with endogenous regions of fibrin deposition. Progress along these new aims is outlined below.

Development of fibrin-binding microgels as synthetic platelets for augmentation of clotting

Clot formation is critical to the cessation of bleeding and involves the conversion of circulating fibrinogen to active, self-assembling fibrin monomers, which in conjunction with platelets, form a hemostatic plug at the site of injury. However, clot formation is impaired during hemorrhaging due to massive consumption and dilution of platelets and other critical clotting factors. During clot formation, platelets bind multiple fibrin fibers thereby cross linking and stabilizing the developing clot. Our fibrin binding microgels are able to mimic this feature of natural platelets by interacting with fibrin with high affinity and specificity at the site of injury and therefore can act as synthetic platelets (SPs). The ability of fibrin-specific microgels to act as SPs, fibrin-specific scFv antibodies were conjugated to pNIPAm hydrogel microparticles and their ability to augment clotting *in vitro* and *in vivo* was investigated. We characterized the effect of SPs on fibrin network structure using confocal microscopy. These experiments demonstrated that SPs interact extensively with fibrin networks compared to control microgels; furthermore, increasing concentrations of SPs during fibrin polymerization result in a denser fibrin network compared to control gels. To characterize the effect of SPs on clotting *in vitro*, we utilized an endothelialized microfluidics device that accurately recapitulates the cellular, physical, and hemodynamic environment of microcirculation. (1) Clotting of platelet poor plasma (PPP) in the
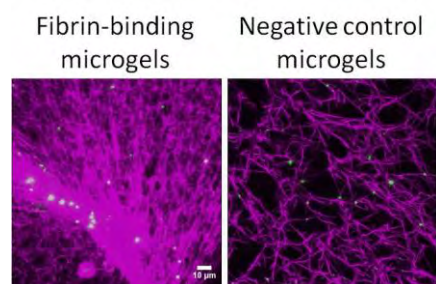

Figure 18: Effect of SPs on fibrin network architecture. The presence of fibrin-binding microgels during clot formation result in a much denser fibrin matrix compared to negative-control microgel incorporation. Fibrin matrix (purple); microgels (green).
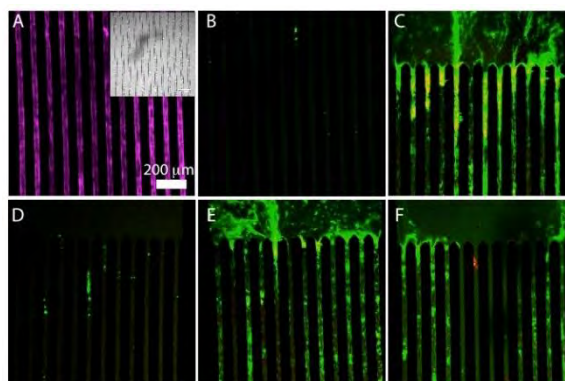

Figure 19. *In vitro* clotting assay. Endothelial cells prior to plasma injection stained with cell mask deep red (A) and phase (inset). Clotting of PPP alone (B), PRP (C), PPP + non-fibrin binding microgels (D), PPP + SPs (E) and diluted PPP + SPs (F). Fibrin=green; microgels/platelets=red

absence or presence of SPs was analyzed in real time using confocal microsopy.

As a control, clotting of platelet rich plasma (PRP) or PPP in the presence of non-fibrin binding microgels was also investigated. *In vitro* clotting experiments in an endothelialized microfluidic device demonstrate robust clotting of PPP in the presence of SPs, similar to that observed with PRP, while PPP alone or in the presence of non-fibrin binding microgels resulted in minimal clotting (Figure 19). Furthermore, clotting was also observed upon addition of SPs to PPP diluted 1:1 with buffer, conditions, which simulate the dilution of clotting factors observed during hemorrhage. These promising preliminary results led to the design of *in vivo* bleeding time studies to further characterize the utility of fibrin-binding microgels for augmentation of clotting.
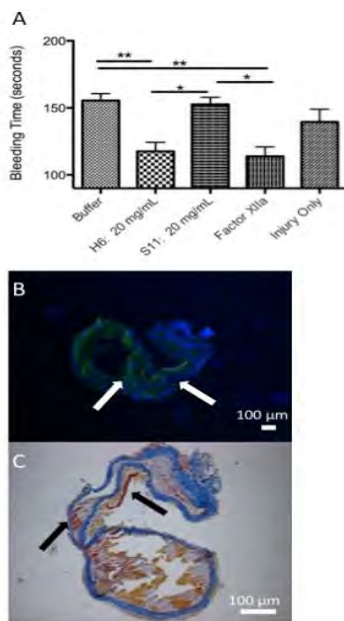
Figure 20. *In vivo analysis of clot augmentation.* Bleeding time of rat femoral vessel injury model. (A) Histological analysis (B,C) shows fibrin-binding microgels (I, green) localize to the clot.

To characterize the ability of fibrin-binding microgels to decrease bleeding times and blood loss in response to traumatic injury, we utilized a rat femoral vessel injury model. In these experiments, fibrin-binding microgels, non-binding control microgels, buffer only or FVIIa (current clinical standard) were injected via tail vein injection. Following a five-minute circulation time, an injury was introduced to the femoral vein and bleeding times were recorded. Following cessation of bleeding, animals were euthanized and veins were removed, fixed and utilized for postmortem analysis. Histological staining for the scFv and fibrin were performed to visualize the microgels and clot formation. Bleeding time were found to significantly decrease in the presence of fibrin-binding microgels (p<0.01) compared to buffer only controls. The observed decrease was similar to that seen in the presence of F7a, the current clinical standard for treatment of traumatic bleeding (Figure 20a). Furthermore, histological analysis of the veins indicates that fibrin-binding microgels localize to the site of injury. Fibrin binding microgels were visualized through immunofluorescence staining for the MYC tag on the scFv and are seen in green in Figure 20b. Fibrin clots were visualized through MSB staining for fibrin and are seen in red in Figure 20c.

Materials and Methods

<u>Synthetic platelet (SP) production</u>

SPs are products created through the coupling of fibrin-specific scFv antibodies to pNIPAm hydrogel microparticles. The production of scFvs and synthesis of microparticles are outlined below.

Fibrin-specific antibody production- ScFv antibodies with high affinity for fibrin and low affinity for fibrinogen were previously identified in Dr. Barker's lab using two phagemid libraries, Tomlinson I (scFv) and the domain antibody (DAb) library, in biopanning assays against fibrin. Ten clones were identified per library, and the specificity and binding affinity of each clone to fibrin were evaluated with surface plasmon resonance (SPR). Clones found to have a high affinity for fibrin and low affinity for fibrinogen will be utilized to impart fibrin-specificity to the HPMs. ScFv with a range of affinity to fibrin have been identified and will be investigated. Negative control microscaffolds will be created using a scFv clone with no affinity for fibrin. ScFvs will be produced in HB2151 *Ecoli* and purified using protein A affinity chromatography (AKTA Purifier, GE Healthcare, Piscataway, NJ, USA).

Microgel synthesis and conjugation of scFvs- Microgels with a highly deformable, dendritic architecture were produced using standard seeded precipitation polymerization utilizing a 95%pNIPAm/5%AAc composition (poly(*N*-isopropylacrylamide-*co*-acrylic acid). Resulting microgels were ~1-μm diameter in the swollen state. Co-polymerization with acrylic acid provides carboxylic acid chemoligation sites for scFv attachment. Following synthesis, microscaffolds were purified using ultracentrifugation and conjugated to fibrin specific scFvs using standard EDC/NHS chemistry. To enable imaging by confocal fluorescence microscopy, scFvs were labeled with malemide-Alexa Flour-488 prior to conjugation to the microscaffolds. As a control, microgels were conjugated to a non-fibrin binding scFv.

<u>Confocal microscopy analysis</u>- Fibrin clot structure was analyzed using confocal microscopy. Fibrin clots with and without fibrin-binding microgels or non-binding microgels were prepared by initiating polymerization with 0.25 U/mL human α-thrombin (Enzyme Research Laboratories) and then examined using confocal microscopy (Zeiss 510 VIS). To allow for visualization of the microscaffolds and fibrin matrix, Alexa Fluor 555-labeled fibrinogen and Alexa Fluor 488-labeled microscaffolds were utilized for these assays. Clots were formed directly on a glass slide, overlaid with a coverslip and allowed to polymerize for an hour prior to imaging.

<u>*In vitro* clotting assays</u> To characterize the effect of SPs on clotting *in vitro*, we utilized an endothelialized microfluidics device that accurately recapitulates the cellular, physical, and hemodynamic environment of microcirculation developed in our collaborator Dr. Wilbur Lam's lab, a description of which was recently published in the *JCI*[1]. Clotting of platelet poor plasma (PPP) in the absence or presence of SPs was analyzed in real time using confocal microscopy. As a control, clotting of platelet rich plasma (PRP) or PPP in the presence of non-fibrin binding microscaffolds was also be investigated.

<u>*In vivo* studies: Femoral vessel injury model and bleeding time studies</u> A well-established rat femoral vessel traumatic injury model[2-4] was utilized to test the efficacy of SPs in hemostasis. This model results in an easily visualized, continuous stream of blood flowing from the injury site. As previously described, an incision was made from the abdomen to the hindlimb of anesthetized rats to expose the right femoral vein. Bleeding was induced by puncturing the vein with a 22 gauge needle. Prior to induction of injury, treatment groups were injected intravenously via the tail vein. Treatment groups included

injury alone, saline (vehicle), rFVIIa (100 µg/kg, the current standard of care[5]), fibrin-binding microgels and non-binding microgels. 0.5 mL of 20 mg/mL microgel solutions were injected/animal. Following a 5 minute circulation time, injury was induced to the right femoral vein. Bleeding time was defined as the time required for bleeding to cease for a minimum of 10 seconds. 6 male Sprague Dawley rats were analyzed per group. Following cessation of bleeding, animals were euthanized, the femoral veins were isolated and fixed with 10% formalin. Veins were paraffin embedded and 5 um sections were produced using a Microm 355H Microtome (Thermo Scientific). Co-localization of fibrin-binding microgls and fibrin clots were characterized through IHC staining for the MYC tag on the scFv and through Martius Scarlet Blue (MSB) staining for fibrin in adjacent serial sections.
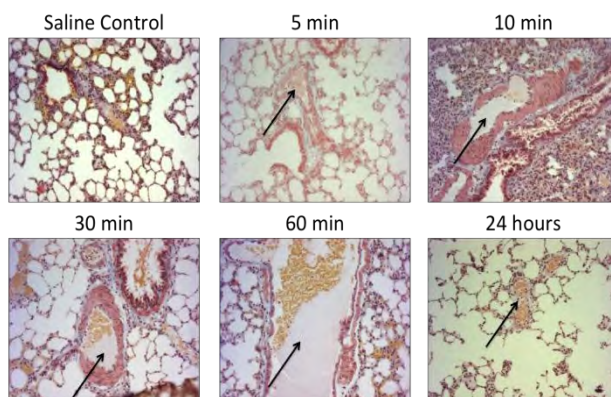
Figure 21. Pulmonary embolism model validation. Detection of fibrin clots in lungs of embolic rats with MSB stain for fibrin 5 min - 24 hours post injection. Fibrin particles in the lung readily accumulate within 5 min and can be minimally detected 24 hours after injection. Red = fibrin, yellow = erythrocytes, blue = collagen. Arrows indicate fibrin clots.

Characterization of fibrin-binding scFvs with regions of endogenous fibrin deposition

It is currently unknown how fibrin-binding DAbs or DAb-microgels behave *in vivo*, therefore it is necessary to explore potential complications associated with this technology such as initiation and/or augmentation of thrombi in the body. Because these DAbs have the potential to interact with endogenous fibrin, it is critical to determine if fibrin-binding DAbs or DAb-functionalized microgels will induce thrombus formation or augment thrombus growth leading to potential stroke and/or heart attack. To this end, we will perform a series of animal experiments to characterize the behavior of DAbs or Dab-microgels in a complex *in vivo* environment. We will use an *in vivo* rat pulmonary embolism model to evaluate the interactions of DAbs and DAb-microgels with endogenous regions of fibrin deposition. In these studies we will evaluate the circulation half-life of the DAbs and DAb-microgels in normal rats and monitor the biodistribution DAbs and DAb-microgels in both normal and embolitic rats. We have characterized this model, which is described below.

Pulmonary embolism model development:

Characterization of the pulmonary embolism model demonstrated accumulation of fibrin particles in the lung within 5 min after injection (Figure 21); particles can be minimally detected 24 hours post injection. These results demonstrate our ability to successfully

perform the pulmonary embolism model and inform the design of future *in vivo* experiments. Furthermore, tissue samples obtained from this model were used to analyze the ability of the fibrin binding antibodies to detect clots in fixed tissue. As seen in Figure 22, our fibrin-binding scFv can detect fibrin clots in fixed tissue and result in similar staining patterns as immunohistochemical (IHC) staining with a commercially available fibrin antibody and standard histological Martius Scarlet Blue (MSB) staining for fibrin. We will next analyze the circulation half-life and biodistribution of fibrin-binding scFvs and scFv-microgel conjugates.
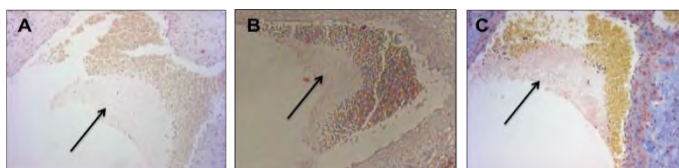
Figure 22. Detection of fibrin in fixed tissue: Detection of injected fibrin clots in fixed tissue with fibrin-binding scFv. Similar staining patterns are observed in serial sections through IHC staining with fibrin-specific scFv (**A**) a commercially available fibrin antibody (**B**) and MSB staining for fibrin (**C**). Arrows indicate fibrin clots.
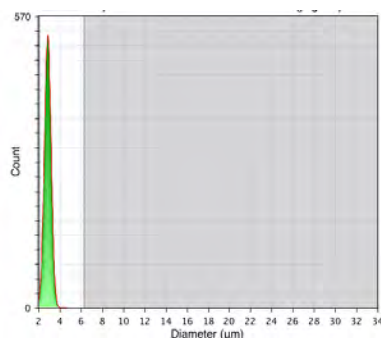
Figure 23. Moxi Z data indicating a narrow size distribution of fibrin particles (mean diameter= 2.5 µm).

Materials and Methods

Animal model development: microemboli acute pulmonary embolism model – The pulmonary embolism model utilized for these studies is based on a previously established model that systemically introduces microemboli (2-5µm clot particles) via tail vein injection. Briefly, clots were formed from human plasma mixed with thrombin and allowed to form for 4hrs at room temperature. Microemboli were generated by dissecting the clot into 1-2mm pieces, which will be resuspended in Krebs-Ringer bicarbonate buffer and undergo subsequent homogenization with a tissue homogenizer. The end product consists of a

population of microemboli of 2-5μm diameter. Particle size was verified with a Coulter Counter or a MOXI Z automated cell counter (Orflo). This protocol resulted in a narrow distribution of particles sizes with mean diameter of 2.5 μm (**Figure 23**). Anesthetized male Sprauge Dawley rats were then subjected to 200μL tail vein injection of the microemboli using a 27.5 gauge needle (106 particles per injection). This model has been shown by other groups to produce stable pulmonary embolisms with a low rate of mortality (<3%) and our validation of this model resulted in no deaths. Validation of this model demonstrates accumulation of fibrin particles in the lung within 5 min after injection (**Figure 21**); particles can be minimally detected 24 hours post injection. This microembolism rat model allows for unique control of the microembolism content. Therefore, we avoid cross-species reactivity concerns since the antibody fragments are derived from human IgG and screened against human fibrin clots.

Detection of fibrin clots in fixed tissue sections

In these studies we simultaneously validate the pulmonary embolism model and analyze the ability of our fibrin-binding scFvs to detect clots in fixed tissue. Fibrin clots and scFv biodistribution/co-localization was accessed post-mortem through staining and imaging of fixed/sectioned tissue. Clot accumulation was analyzed 5 min, 10 min, 30 min, 60 min and 24 hours after injection. At the specified time point, rats were euthanized and organs separated, fixed with 10% formalin, paraffin embedded and 5 um sections will be produced using a Microm 355H Microtome (Thermo Scientific). Co-localization of injected fibrin clots and scFvs was characterized through IHC staining with both our fibrin-binding scFv and a commercially available fibrin-binding antibody (American Diagnostica) and through Martius Scarlet Blue (MSB) staining for fibrin in adjacent serial sections. Data demonstrate our fibrin-binding scFv can detect fibrin clots in fixed tissue and result in similar staining patterns as IHC staining with a commercially available fibrin antibody and MSB staining for fibrin (Figure 22). Controls included rats injected with saline and euthanized immediately. IHC with both the fibrin-binding scFv and commercially available fibrin antibody, along with MSB staining, demonstrate minimal staining on tissue sections obtained from control rats (Figure 24).
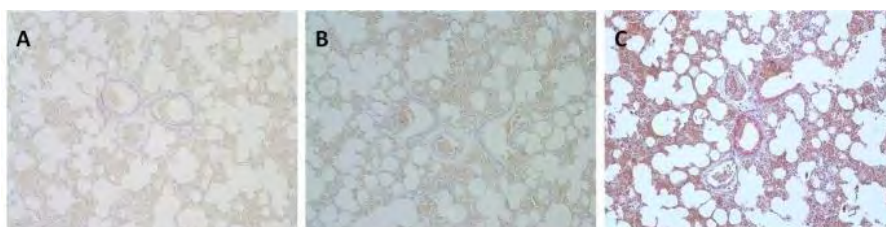

Figure 24: Minimal staining observed on control samples. Tissue samples from control rats injected with saline were analyzed for nonspecific staining with IHC staining with our fibrin-probe (**A**) a commercially available fibrin antibody (**B**) and MSB staining for fibrin (**C**). As expected, minimal staining was observed on these negative control samples.

Conclusions and Future Directions (for Aim 3, tasks 13, and 14.)

These studies combine innovative biopanning techniques with highly deformable microgels to develop fibrin-binding SPs that augment the natural clotting cascade. Like natural platelets, our SPs specifically target fibrin rather than fibrinogen and interactive extensively with fibrin networks. The addition of SPs to fibrin clots significantly alters clot architecture and results in the formation of a much denser fibrin network compared to

control clots. Furthermore, the addition of fibrin-binding SPs to PPP results in robust clot formation in an *in vitro* clotting assay, demonstrating our SPs can enhance clot formation *in vitro*. The utility of SPs in augmenting clotting was further verified in *in vivo* utilizing bleeding time assays in a rat femoral vessel injury model. SPs were found to localize to the site of injury and significantly decrease bleeding times. Future studies will characterize the circulation times and biodistribution of fibrin-binding microgels in a complex *in vivo* environment. These studies will utilize a rat pulmonary embolism model to characterize the safety of fibrin-binding microgels in the presence of endogenous fibrin deposition. Here we describe the successful implementation of the pulmonary embolism model. Results thus far demonstrate our fibrin binding microgels show extreme promise and materials for augmentation of clotting.

Specific Aim 4. Adapt percutaneous stem cell delivery strategies for craniofacial cartilage defect repair.

Task 6. Perform rat xyphoid defect study for microencapsulated rat ASCs and prechondrocytes.

We have completed the *in vivo* study investigating the effect combing a RGD-hydrogel scaffold with ASC microbeads has on cartilage regeneration using the xiphoid defect animal model. Below are the description of the experiment and the results.

Methods: P1 ASCs isolated from male Sprague Dawley were microencapsulated (uE) at 25×10^6 cells/cm^3 in 20mg/ml LVM alginate through a 28G needle at 6.0kV/cm and treated with growth medium or chondrogenic medium (CM) for 5 days. Prior to surgeries, sterile RGD-conjugated alginate (NOVATACH M RGD, FMC BioPolymer) was dissolved in DMEM containing 1% penicillin and streptomycin at a concentration of 25 mg/mL and mixed with sterile 20 mg/mL CaSO$_4$ (Sigma) at a 4:1 volume ratio using two syringes connected to a luer-lock 3-way connector. During surgeries, 2 mm cylindrical defects were made in the xiphoids of 120g male Sprague-Dawley rats. ASC microbeads were implanted into the defect, immobilized with the RGD-conjugated hydrogel mixture, and covered with SEPRAFILM®. Empty defects with the hydrogel mixture and re-implanted excised cartilage (autografts) served as controls in the 2 mm study. All groups were tested in 7 rats. After 35 days, xiphoids were explanted, x-rayed, and incubated in a 40% Hexabrix solution for equilibrium partitioning of an ionic contrast agent-microcomputed tomography (EPIC-µCT) to visualize and quantify proteoglycan distribution. Samples were then fixed in 10% phosphate-buffered formalin (Sigma) for 48 hours and embedded in paraffin. Sagittal sections of the defect were stained with safranin-O using a fast green counter stain to evaluate proteoglycan present. Statistical differences among these experimental groups were determined via ANOVA with a post hoc Tukey test (GraphPad Prism). All differences and effects were considered to be statistically significant if the p-value was less than 0.05.

Results: X-ray scoring of defects showed that defects with GM or CM preconditioned ASC microbeads and hydrogel mixture performed better than empty defects with only the hydrogel. Defects with only the hydrogel mixture had no apparent cell infiltration, new extracellular matrix (ECM) deposition, or perichondrium, as indicated by the lack of fast green staining in Figure 25. Defects with the ASC microbeads preconditioned in MSCGM had traces of fast green staining throughout the defect with cell infiltration and tissue deposition at the edges of the defect. Defects with ASC microbeads preconditioned in CM had ECM deposition throughout the defect with cell infiltration, tissue resembling a perichondrium, and initial proteoglycan deposition. Defects with the autograft had cell

infiltration, a perichondrium that resembled that of the surrounding xiphoid and proteoglycan deposition between the edges of the defect and autograft. EPIC-µCT measured cartilage volume was highest for the autograft group, and no difference in cartilage volume was seen in any defect containing the hydrogel mixture (Figure 25).

Subsequent investigation revealed that a noticeable amount of hexabrix was retained within alginate constructs after incubation overnight. This finding was highly surprising because of alginate polymer's negative charge and because of the ability of alginate microbeads to provide extended release of high pI proteins. However, the negatively charged hexabrix may have interacted with the calcium crosslinks in alginate gels. Because the ability of EPIC-µCT to visualize and quantify proteoglycan production is dependent on hexabrix exclusion from the anionic tissue, this method may not be optimal for detecting neocartilage formation within alginate constructs.
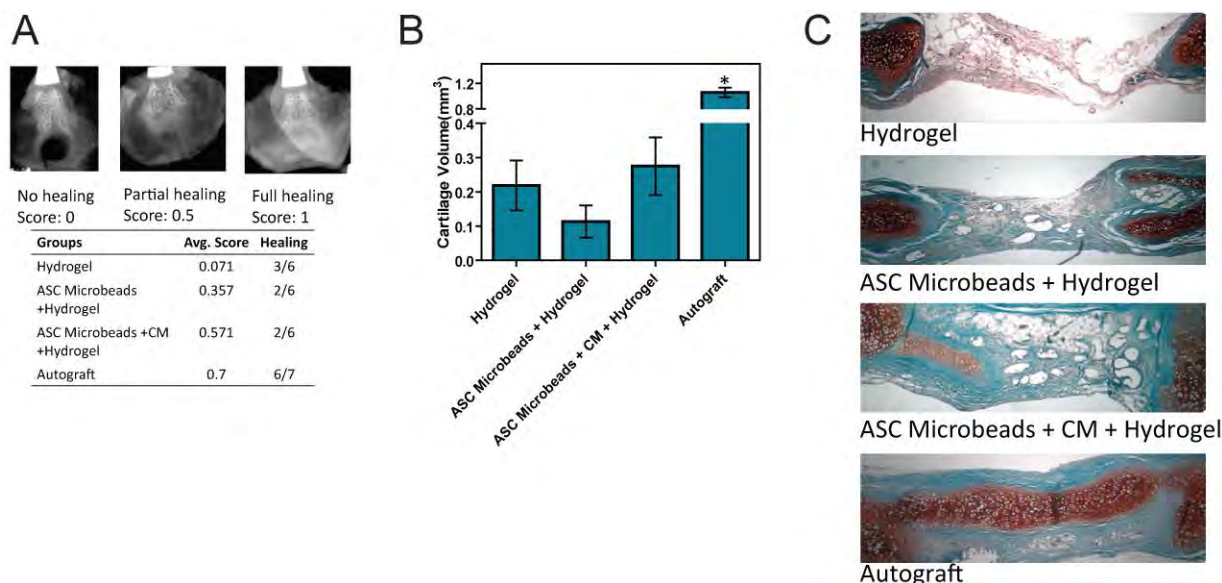
Figure 25. ASC Microbeads and RGD-Hydrogel Mixture in Xiphoid Defect
(A) Radiographic scoring. (B) 3-D EPIC-µCT calculated cartilage volume within defects (n=7±SE, *p<0.05 vs. all groups). (C) Representative Safranin-O staining of 2 mm defects.

Task 8. Determine critical size defect in rabbit ear cartilage. Surgeries will be conducted at the ISR for this part of the study.

Methods: New Zealand White rabbits (1500-2000 g, 8-10 weeks) were anesthetized using subcutaneous injections of ketamine/xylazine/ace-promazine. Anesthesia was maintained using inhaled isoflurane delivered by nose cone inhalation at 1-2% in O_2, to effect. The operation sites (outside and inside of ear) were shaved and disinfected with three alternating applications of isopropanol and chlorhexiderm. The skin at the concave side at the proximal medial border close to the root of the ear cartilage was incised approximately 5 cm in distal direction longitudinal along the point of inflection of the helix. Skin was elevated and blunt dissection of cartilage and the skin beginning with the convex side performed until we have created a pouch under the skin of approximately 5x3 cm and continued on the concave side. A metal protective device was placed at the convex side between the cartilage and the skin to avoid damage to the skin by the biopsy punch (Figure 26A). Three punch holes (2 mm, 4 mm and 6 mm) were made in each pinna, separated by

1 mm (Figure 26 B,C,D). The skin was closed with resorbable 5-0 sutures with simple interrupted stitches. Buprenorphine (0.03 mg/kg) was given once post-operatively. After 6 weeks, rabbits were euthanized by ear vein injections of pentobarbital 1.5 ml/rabbit of a 390 mg/ml veterinary euthanasia solution. Cartilage defects were examined by X-ray, uCT, and histology to determine the critical sized defect.
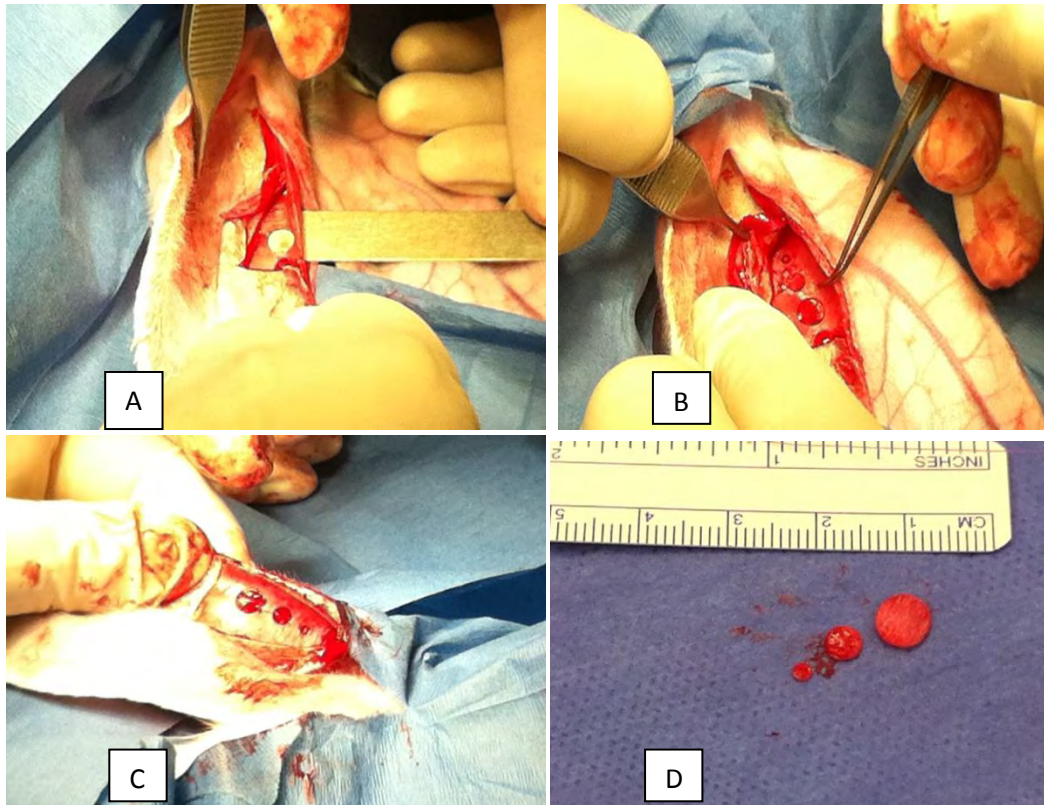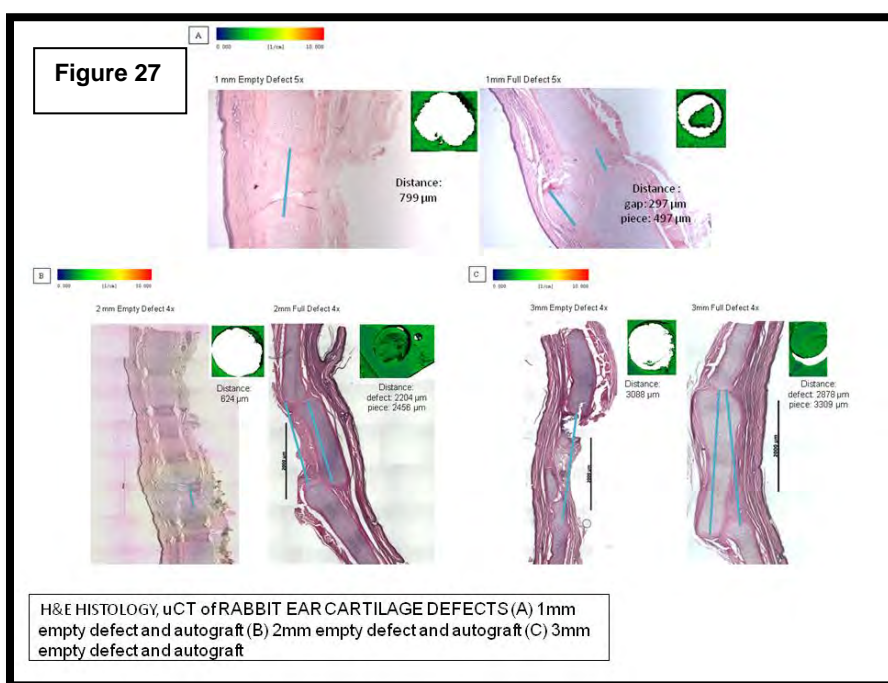

Figure 26. Intra-operative images of rabbit critical-sized defect model. (A) Protective metal device placed under cartilage to prevent damage to underlying skin during punch procedure. (B, C, D) Biopsy punches made in rabbit cartilage and resulting pieces removed.

Results: The 1mm, 2mm, and 3mm cartilage defects were examined by µCT and histology in order to demonstrate that a full-thickness defect was created in the cartilage layer, and that the defect maintained patency over time without wound repair or tissue replacement. Full-thickness defect patency was demonstrated over time in each of the three defect sizes (Figure 27 A,B,C). The 1mm empty sample had a 799µm-sized defect in the cartilaginous layer apparent on histology and the µCT image demonstrates a patent circular defect in the empty sample. The 3mm empty sample had a 3088µm-sized defect that also demonstrates a patent circular defect in the histologic and µCT images.

The autograft control demonstrates the presence of chondrocytes across the expanse of the defect, complete reintegration of the autograft was not achieved. The small size of the autograft made perfect replacement of the tissue within the margins of the cartilage layer difficult. It is likely that the autograft shifted position upon closure of the skin

33

or some time post-operatively. The larger-sized autografts were easier to replace within the margins of the cartilage defect as evidenced by both the histology and μCT images of Figures 27B and 27C. It is felt that with better replacement and apposition of the autograft within the margins of the defect, there will be more substantial reintegration of the tissue. Going forward, a fibrin sealant will be applied intra-operatively to the graft in order to secure its position prior wound closure. This will help to provide better apposition at the margins of the defect and the graft.

In conclusion, it was demonstrated that defect patency was maintained for the smallest defect size created. Going forward, the 3mm sized defect will be used. The larger size will allow easier implantation of biomaterials, as well as replacement and reintegration of the autograft tissue. This will provide a more effective model for studying cartilage regeneration.

Figure 27

H&E HISTOLOGY, uCT of RABBIT EAR CARTILAGE DEFECTS (A) 1mm empty defect and autograft (B) 2mm empty defect and autograft (C) 3mm empty defect and autograft

The model used in this study is being structured for ASTM's F04 division of Tissue Engineered Medical Products Preclinical Assessments. These results will be combined with the study currently underway at Spheringenics where they are using the model to assess effectiveness of microbeads containing mesenchymal stem cells.

Task 10. Identify optimum microbead and scaffold delivery system.

We finalized the microbead formulation prior to moving on to other experiments. Below are the results of our microbead formulation studies.

Previously, we demonstrated the controlled release of ASCs from alginate microbeads through alginate lyase-mediated degradation. Next, we investigated the viability of the ASCs released from the alginate microbeads. The viability of the cells was assessed through live/dead staining and the Tunel assay. The results show that the viability of microencapsulated ranged from 64% on day 2 to 79% on day 12 (Fig.28). The viability of

the cells released from the alginate microbeads ranged from 87% on day 2 to 71% on day 12 (Fig. 29). There was no difference in DNA integrity amongst all groups (Fig. 29C).
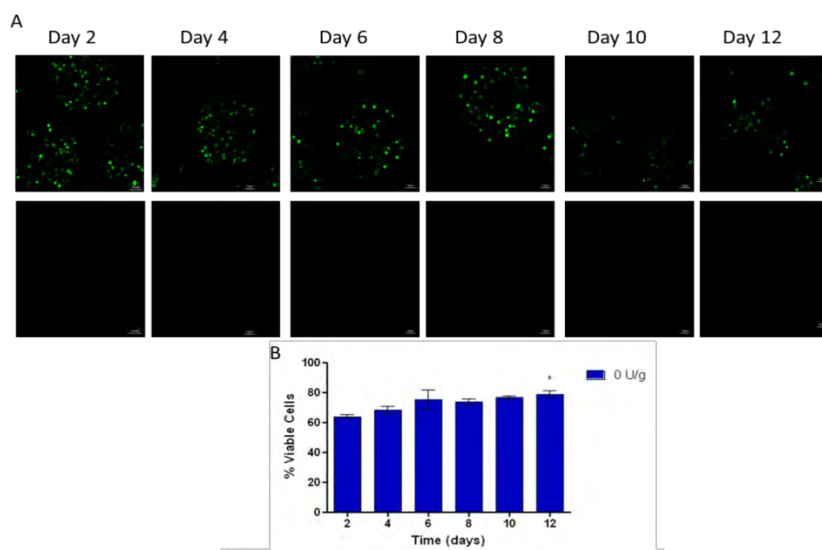

Figure 28. The viability of microencapsulated rASCs without alginate lyase. (A) Live/dead staining of rASCs within the 0 U/g alginate (medical grade) microbeads (Scale bar = 50 μm) on days 2, 4, 6, 8, 10, and 12, where green represents live cells and red represents dead cells, and (B) the percent viable cells. Data were analyzed using one-way ANOVA followed by Bonferroni's modification of Student's t-test. * $p < 0.05$ vs. day 2.
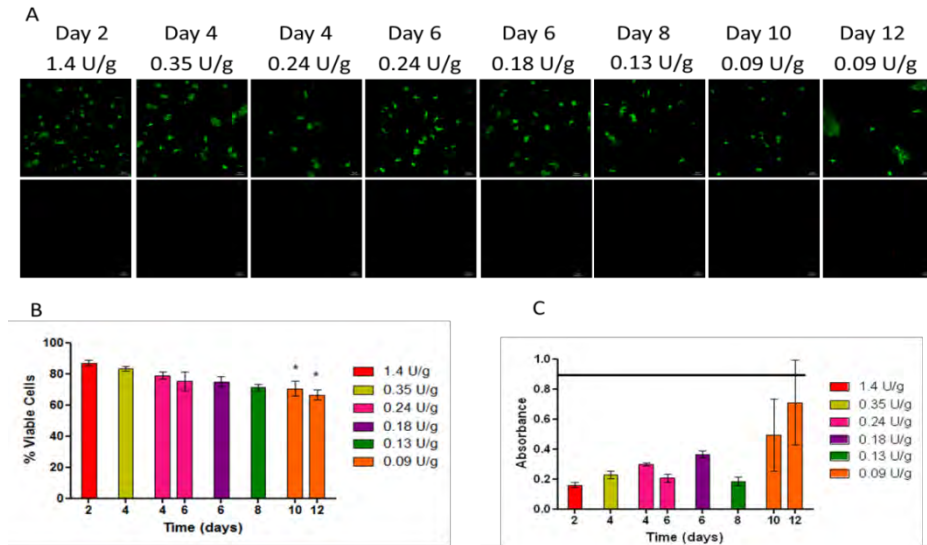
Figure 29. The viability of rASCs released from alginate (medical grade) microbeads made with different formulations of alginate lyase (U): alginate (g) (Scale bar = 50 μm) (A) Live/dead staining of released rASCs, where green represents live cells and red represents dead cells, (B) the percent viable cells, and (C) Tunel assay of released rASCs (the horizontal bar represents the positive control generated) at the respective times; 1.4 U/g on day 2, 0.35 U/g on day 4, 0.24 U/g on days 4 and 6, 0.18 U/g on day 8, 0.13 U/g on day 10, and 0.09 U/g on days 10 and day 12. Data were analyzed using one-way ANOVA followed by Bonferroni's modification of Student's t-test. * $p < 0.05$ vs. day 2.

It is important that the cells released from the alginate microbeads are able to become osteoblasts. The next study investigated whether or not the phenotype of the cells released were maintained. Previously, we found 0.13 U/g to release cells between 8 to 10 days. This group was used to conduct the phenotype study and compared to monolayer cells that were never microencapsulated. The early marker of osteogenic differentiation, alkaline phosphatase showed no statistical difference between the cells released from the alginate microbeads compared to the microencapsulated cells without any alginate lyase and the monolayer cells. Even more significant, osteocalcin, a late marker of bone differentiation was significantly higher compared to the monolayer cells (Fig. 22C). Likewise the mRNA levels of BMP-2, a very important protein in bone formation showed significant increase (Fig. 23D).

In the future, an *in vivo* study will be done to assess the ability of these injectable microencapsulated cells to aid the bone regeneration in a metaphyseal defect.
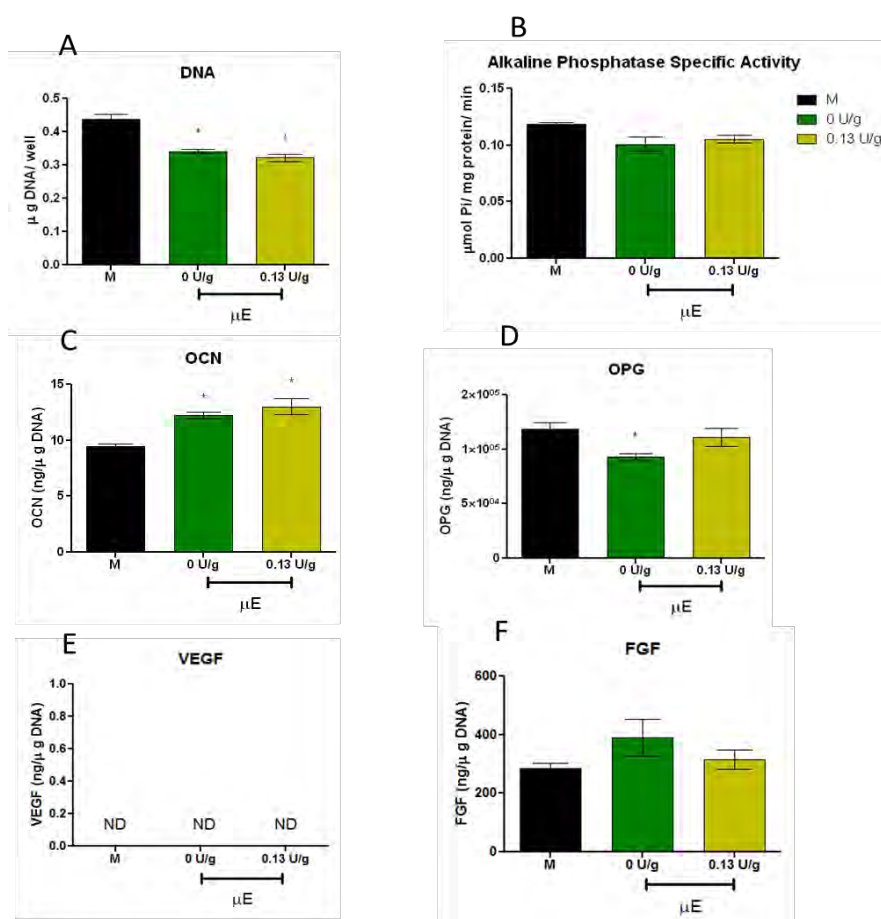

Figure 30. The response of rASCs to osteogenic media, that were not encapsulated (monolayer cells) (M), microencapsulated (μE) and released from 0 U/g and 0.13 U/g alginate (medical grade) microbeads. (A) DNA content, (B) alkaline phosphatase specific activity in the cell lysate, (C) osteocalcin (OCN) levels, (D) osteoprotegerin (OPG) levels, (E) vascular endothelial growth factor

(VEGF) levels, and (F) fibroblast growth factor (FGF) levels. Data were analyzed using one-way ANOVA followed by Bonferroni's modification of Student's t-test. * $p < 0.05$ vs. M.
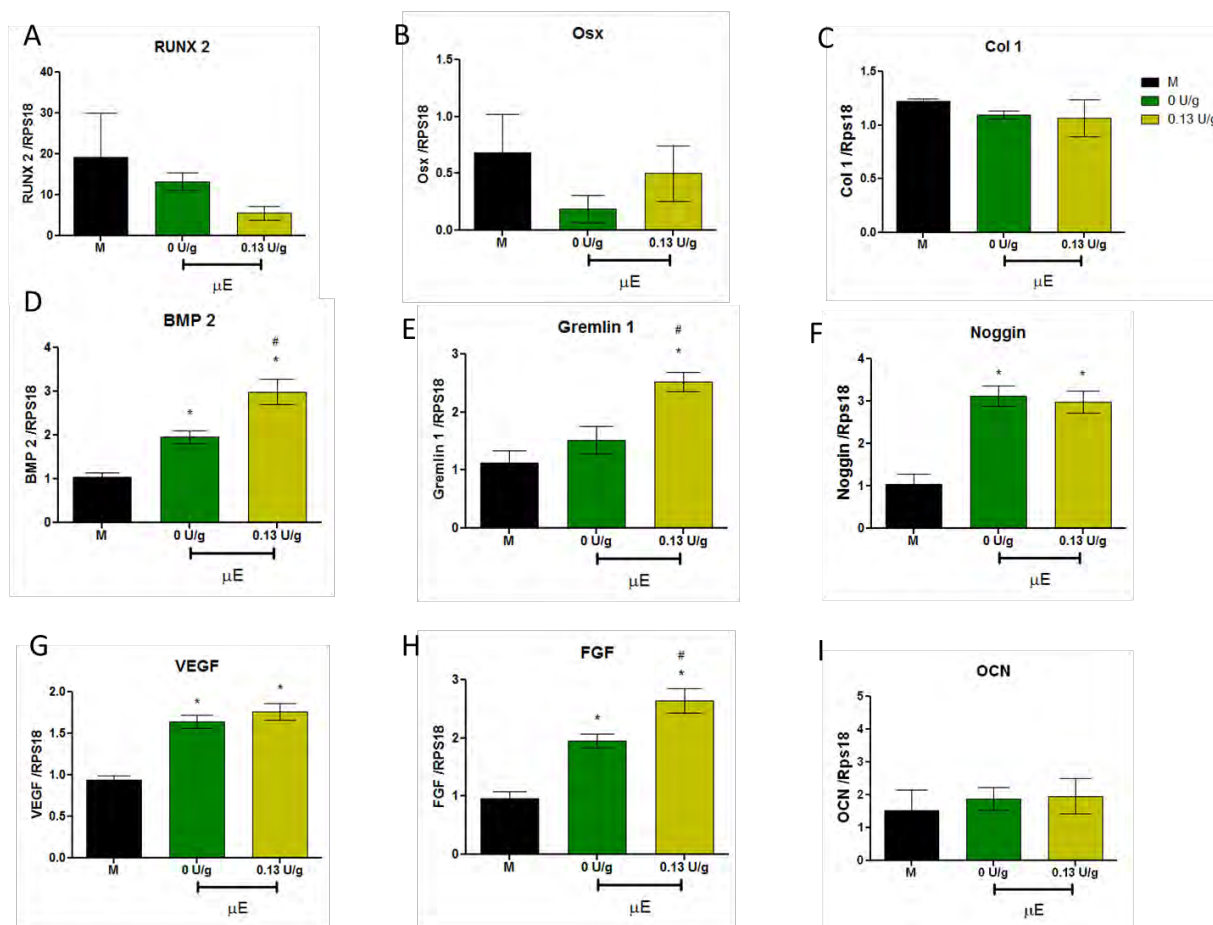

Figure 31. The mRNA levels in rASCs treated with osteogenic media that were not encapsulated (monolayer cells) (M), microencapsulated (µE) and released from 0 U/g and 0.13 U/g alginate (medical grade) microbeads. (A) Runt-related transcription factor 2 (RUNX2), (B) Osterix (Osx), (C) collagen type 1 (Col 1), (D) bone morphogenetic protein 2 (BMP-2), (E) gremlin 1, (F) noggin, (G) vascular endothelial growth factor (VEGF), (H) fibroblast growth factor (FGF), and osteocalcin (OCN). Data were analyzed using one-way ANOVA followed by Bonferroni's modification of Student's t-test. * $p < 0.05$ vs. M.

Specific Aim 5. Develop graft technologies for palate reconstruction.

Task 5. Determine critical size defect size in the rat palate.

Task 6. Test palatal graft formulations in rat palate.

These experiments have been delayed. The move to VCU necessitated a review of the IACUC protocol, which will then be submitted to DoD for ACURO review.

Specific Aim 6. Adapt stem cell delivery technology for treatment of large bone defects.

Task 3. Determine if ASCs are viable in hydrogel systems and assess their osteogenic differentiation potential and growth factor release.

Task 4. Develop loading protocols for loading scaffolds with human ASCs with and without microcapsules.

Task 5. Evaluate different survival of stem cells with different delivery matrices in a subcutaneous model

With these results we have taken the most effective hydrogel (the PEG RGD injectable gel) for cell viability and tested it for in vivo osotegenic differentiation and vascular infusion to provide some insights into Specific Aim 4.

Briefly, 1 million ADSC or BMMSCs were embedded into a 10% w/v PEG hydrogel 24 hours prior to implantation and injected into a nanofiber mesh tube. Some groups received 1 µg BMP-2 in the hydrogel as a osteogenic stimulus to promote mineralized matrix production. A subset of the ADSC groups were also cultured with 12.5 µM resveratrol as that dose was shown to increase mineralization in the PCL/collagen system. Samples were analyzed longitudinally for vascularization of the construct using Laser Doppler Perfusion Imaging (LDPI) at day 0, 1, 3, 7, 14, 21, and 28 days. After 28 days the samples were explanted, fixed, and scanned for mineralized matrix using Micro-CT imaging. Some samples were then snap frozen, sectioned, and analyzed histologically for mineralized matrix, presence of cells, and the presence of vessels in the construct.
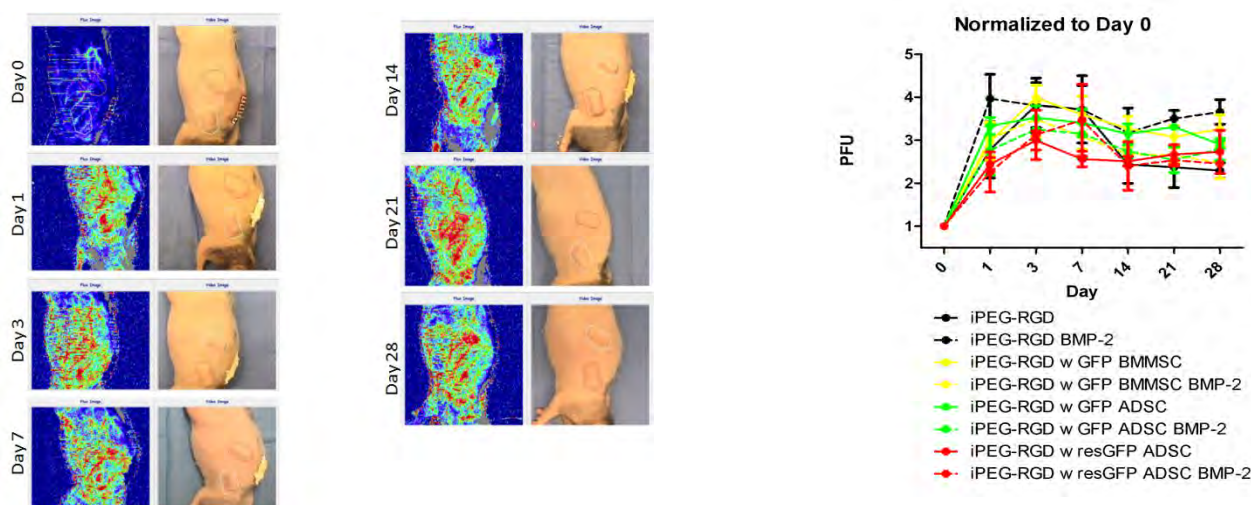

As the images above show, we were able to detect the presence of the hydrogel in vivo using LDPI. All groups displayed a similar longitudinal profile with an initial increase in the vascular perfusion at the implant site, followed by a slight drop off at later time points. No differences were observed in between groups, and this is mainly attributable to the high variance seen in the data. Interestingly, BMP-2 had no effect on the vascularization of the hydrogel although there is evidence in the literature of BMP-2 having a pro-angiogenic effect. This is most likely attributable to the low dose of BMP-2 used in this experiment and it is possible that higher doses would result in an increased vascular response. After explanting the hydrogels, we observed that there was a large amount of the hydrogel left in the nanofiber mesh tube. This is due to the lack of degradable components in the

hydrogel. Histologically we were unable to observe any vessels in the hydrogel due to this lack of degradation. Taken with the LDPI data, this means that the revascularization is occurring around the hydrogel rather than through the hydrogel. This is not ideal as most of the implanted cells in the middle of the construct will die via lack of mass transport.

Analysis of mineralized matrix was performed using Micro-CT imaging and von Kossa staining of frozen sections. Micro-CT showed a large number of small nodules of
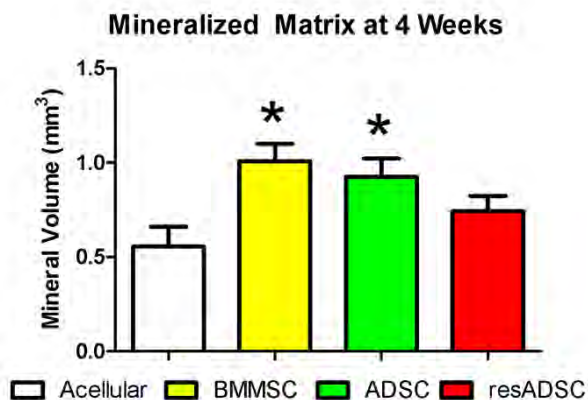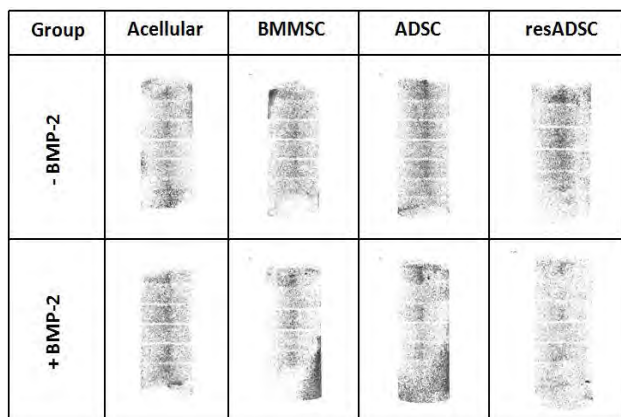

mineral in all viability and applied to an ectopic in vivo mineralization model. Quantification of the mineralized matrix showed that BMMSC and ADSC cell seeded groups had significant more mineralization than acellular groups. We had previously shown that resveratrol pre-treatment of ADSCs results in greater mineralized matrix than untreated cells on PCL scaffolds. Interestingly, we did not see an effect of resveratrol in the PEG hydrogels, and the quantified mineralized matrix was not significantly different from the acellular groups although the mean was higher. We next performed von Kossa staining on
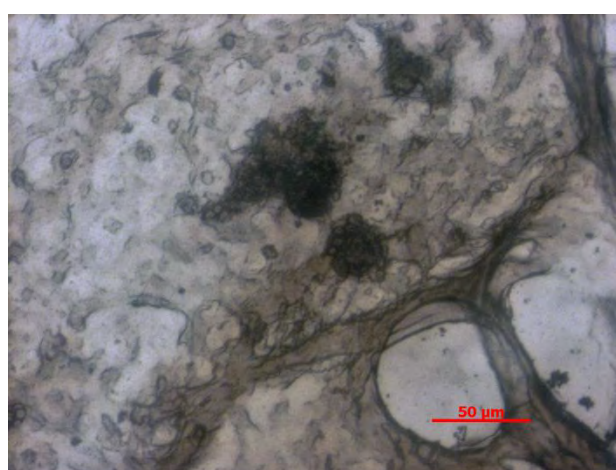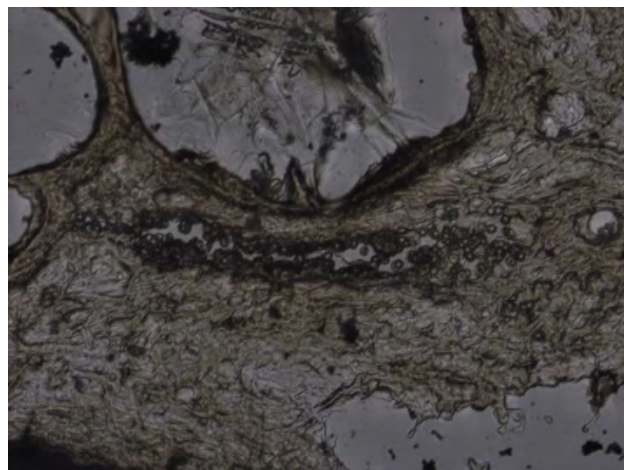
frozen sections to confirm the presence of mineral. Positive staining was found primarily where cells were present as shown below. This demonstrates that the mineralized matrix observed in the Micro-CT imaging is cell mediated. Further, we found cells both in the acellular (below, left) and cellular groups (below, right), demonstrating that there was some host cell invasion into the hydrogel constructs. We have performed fluorescent staining with a GFP antibody to determine if the cells observed in the hydrogel are implanted cells or the host cells, and also to differentiate between host cell mineralization and implanted cell mineralization. While we did observe some positive GFP cells, a majority of the cells in the constructs were GFP negative suggesting that most of the mineralized tissue is from

the host cells as shown in the images below. Taking the mineralization and vascularization data together, we determined that the PEG system was not ideal for robust bone formation *in vivo*.
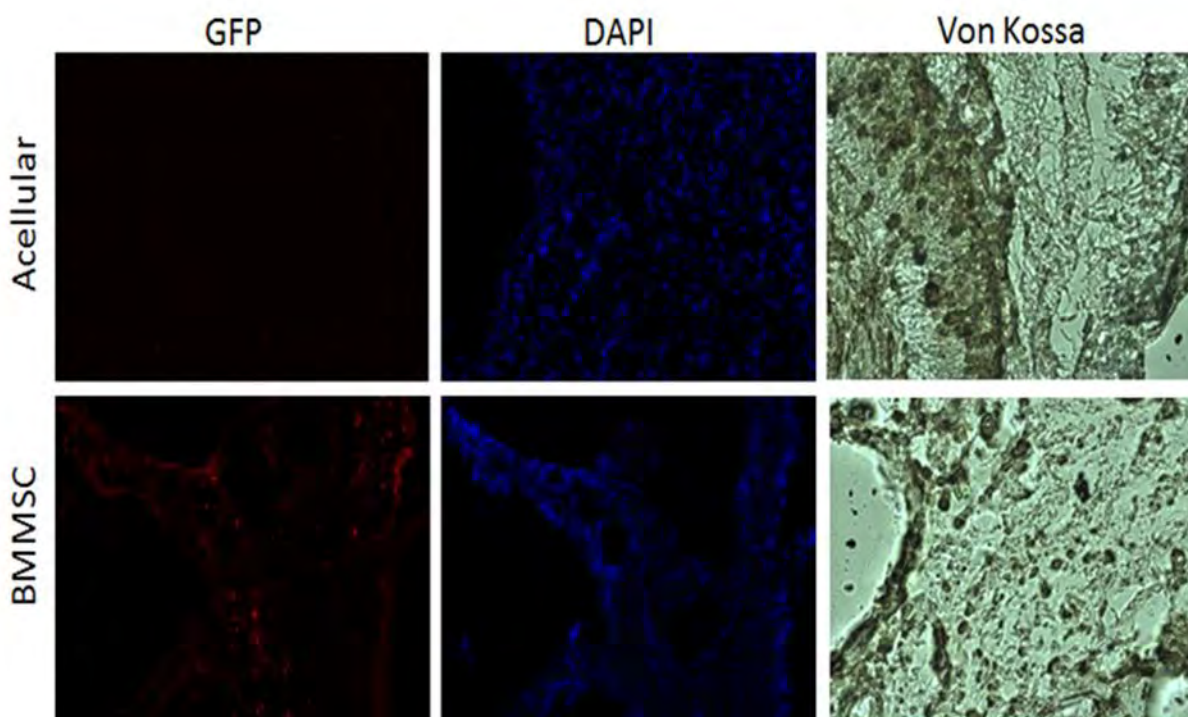

We have also begun investigation of an alginate hydrogel system as a cell delivery vehicle for bone tissue engineering. Compared to PEG, an alginate system has the advantage of being a much lower weight percentage gel facilitating degradation in vivo, as well as cross-linking without the use of chemical cross-linker or a ultra-violet sensitive cross-linker, both of which have a potential detrimental effect on cell viability. Briefly, GGGGRGDSP peptide molecules are covalently attached to the saccharide backbone of the alginate polymer facilitating cell attachment to the hydrogel. The peptide conjugated alginate powder is dissolved in α-MEM at a 3% initial concentration, and then is mixed with a volume of cells in α-MEM to obtain a 2% final weight percentage gel. We are currently investigating two alginate systems: an irradiated alginate that lowers the average molecular weight of the polymer chains, and an oxidized irradiated alginate that is also low molecular weight and also is susceptible to degradation via hydrolysis. We have investigated these two alginate hydrogel systems in terms of cell viability and mass loss over a 14 day time course.

We assessed the cell viability of resveratrol treated and non-treated GFP ADSCs and non-treated GFP BMMSCs in both the irradiated and oxidized irradiated alginate hydrogels. 1 million cells were incorporated into the alginate hydrogel and injected into a PCL nanofiber mesh and cultured statically for 14 days in growth media. At days 1, 7, and

14 samples were taken down and stained with DAPI and ethidium-2-homoimder for nuclei and dead cells, and live cells were determined by the presence of GFP. Using a histomorphometric analysis, we determined the number of live and dead cells at each time point for each cell type and gel type. The degradation kinetics of the gels was determined by weighing each sample at day 0, and then weighing the sample again at the take down point.
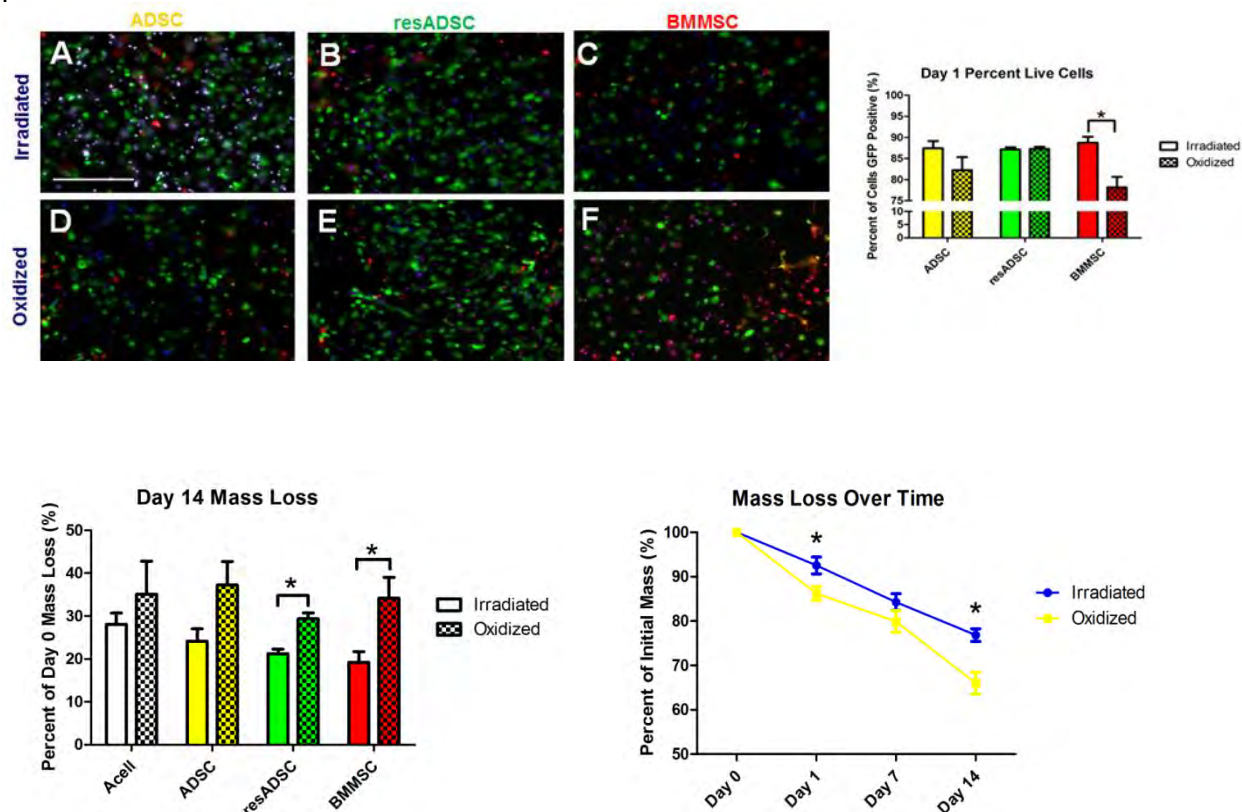

As the graphs above show, we observed an initial loss of ~8% in the irradiated alginate gels and ~15% in the oxidized irradiated gels after only 24 hours in culture. This initial loss is most likely due to the loss of hydrogel that was not fully cross-linked. At day 7 we observed no significant differences in terms of mass loss between the two different hydrogel systems. After 14 days, the oxidized again demonstrated greater mass loss than the irradiated hydrogels. Further, we observed some significant differences in the cell groups between the irradiated and oxidized gels after 14 days in culture, suggesting the cells may be facilitating degradation via hydrolysis in the oxidized gels.
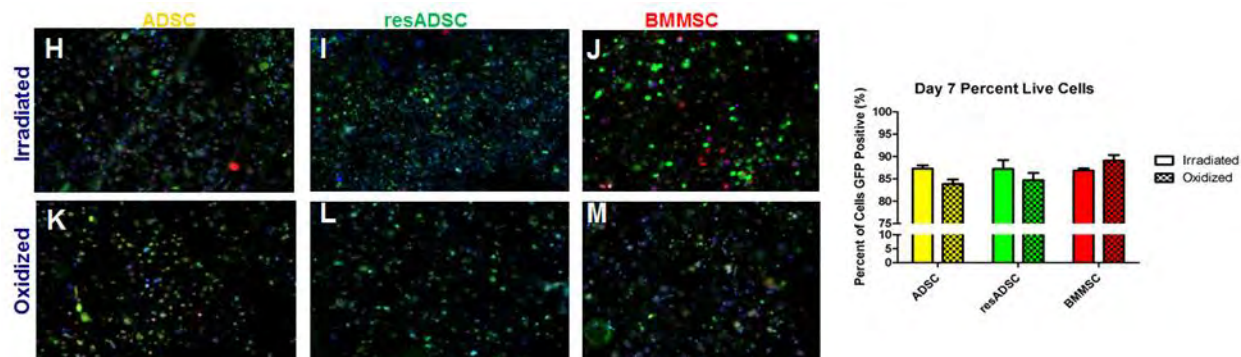
Cell viability was also assessed in the two different alginate hydrogels. We observed

that a majority of the cells survive the mixing and injecting process of generating the hydrogel. Further, the cell viability percentage was in the 80-90% range throughout the 14 day time period for all cell types and gel types, demonstrating a much higher percentage of live cells compared to the PEG hydrogel system described previously. We also observed that the cells appear much smaller at the later time points, hypothesized to be due to proliferation of the cells in the hydrogel causing crowding and a smaller phenotype. This was confirmed with the picogreen DNA assay, as a significant increase in the DNA content of the hydrogel constructs between days 1 and 7 was observed for both ADSC and BMMSC cell types (data shown below). When we pooled the cell groups to assess a difference in viability between the irradiated and oxidized gel systems we observed a significant difference in cell viability with the irradiated hydrogel possessing greater viability than the oxidized hydrogel at an early time point. However at later time points there were no significant differences in the viability of the two hydrogel systems.
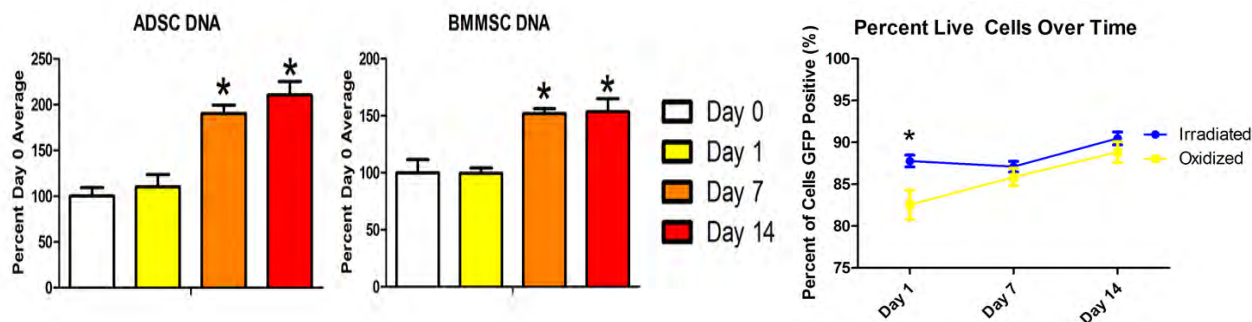
To further evaluate stem cell delivery matrices for their ability to support delivered cell survival, a bioluminescent imaging (BLI) protocol was implemented in collaboration with the Gazit Laboratory (Cedars-Sinai Medical Center, Los Angeles). Lenti-Ub.Luc/GFP viral vector was used to label human mesenchymal stem cells (hMSCs) and human amniotic fluid-derived stem cells (hAFSCs) for constitutive expression of the luciferase and GFP reporter genes. hMSCs and hAFSCs were then evaluated to determine labeling efficiency and the potential impact of Ub.GFP/Luc labeling on cell proliferation (see images below). Labeling efficiency was

Day 14 Percent Live Cells
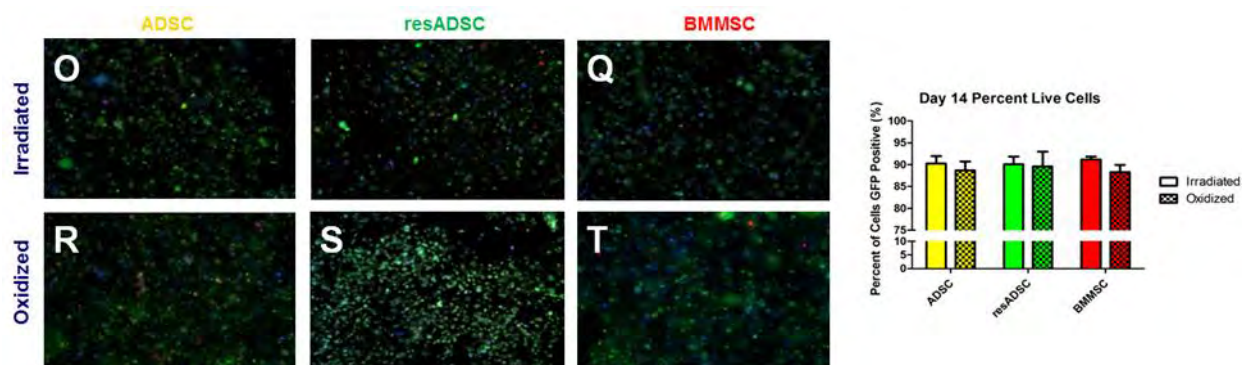
assessed using fluorescence microscopy and flow cytometry. On average, efficiencies of approximately 70% and 80% were observed for the hMSCs and hAFSCs, respectively. Proliferation, as measured 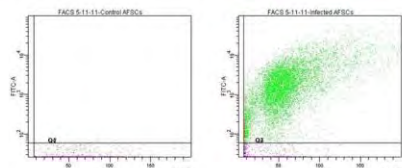by the bromodeoxyuridine (BrdU) assay, remained unchanged following co-transfection and hMSCs retained the ability to osteogenically differentiate over 4 weeks *in vitro*.

hMSC Labeling Efficiency
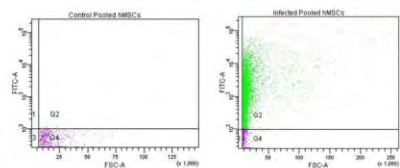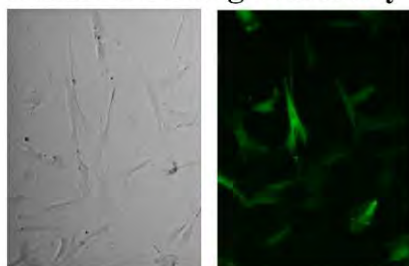
hAFSC Labeling Efficiency
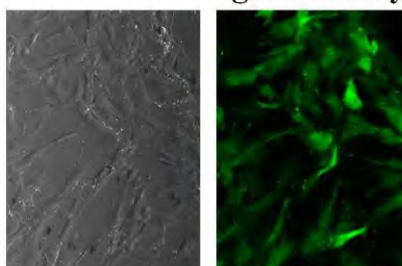
Assessment of Proliferation (BrdU Assay)

BrdU Assay
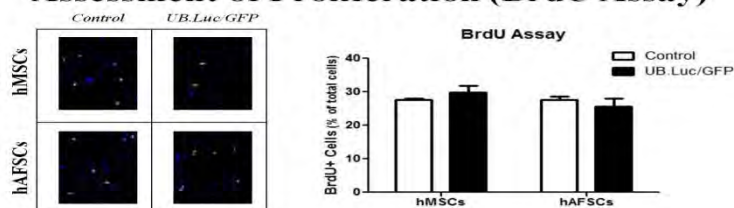
In order to leverage BLI as an in vivo quantitative cell tracking tool, it was necessary to implement an imaging protocol capable of discerning differences in cell number within our large-sized hydrogel-based delivery system and utilization of a subcutaneous implant model. In particular, it was important that bioluminescent counts be specific, void of residual signal from previous injections, and a function of viable cell number. As bioluminescent counts are produced via luciferase-catalyzed oxidation of luciferin substrate, compromised luciferin transport could potentially mask the effect of cell number if the substrate is not

presented effectively. To develop and validate a BLI protocol which correlated linear BLI counts to viable cell number, a cell dose study was conducted in NOD/SCID mice.

Hydrogel-based hybrid delivery constructs were assembled through dual-syringe embedding of hMSCs within a 2% hydrogel and injection of cell-seeded gel into PCL nanofiber mesh tubes as described previously. These constructs were then implanted subcutaneously (2 per mouse) and cells were visualized at each BLI time-point through the injection of luciferin substrate. It was determined that locally injecting 0.2mg of luciferin per construct 20 minutes prior to BLI collection resulted in a linear correlation between counts and live cell number (see images below). Furthermore, BLI counts were found to be specific and lacking in residual signal following a 24-hour period.
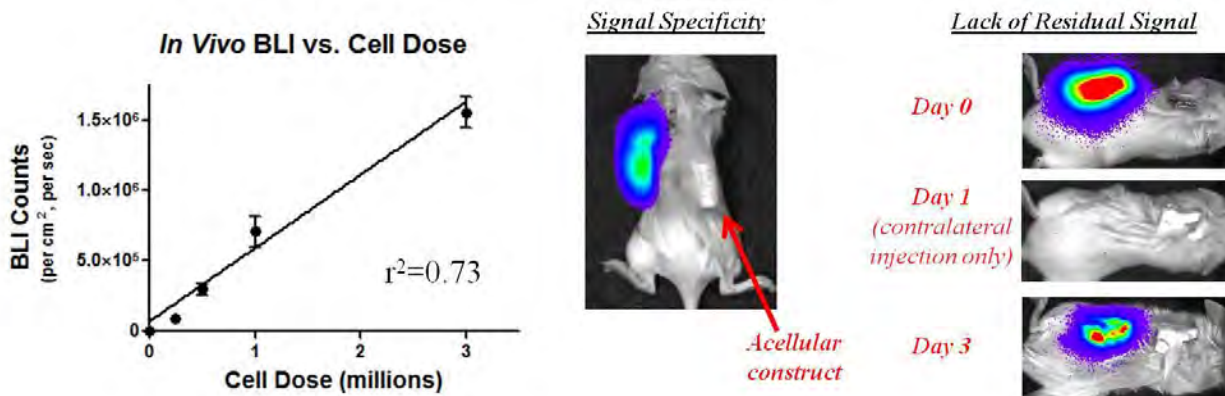
Live cell number, as indicated by BLI, was significantly decreased for all initial cell doses following one-week in vivo, with a more pronounced reduction observed at higher doses (see images below). Live cell number at day 7 was similar across all initial cell dose groups and, for the lower cell doses (0.5 and 1 million), this value was shown to positively correlate with total viable cell number (sum of delivered and endogenous populations) in the explants. Taken together, these results indicate no benefit of higher cell-seeding densities for the examined delivery system and suggest that the short-term persistence of viable delivered hMSCs may positively impact host cell infiltration. Histological analysis confirms the presence of a viable, GFP+ cell population within the constructs at day 7.
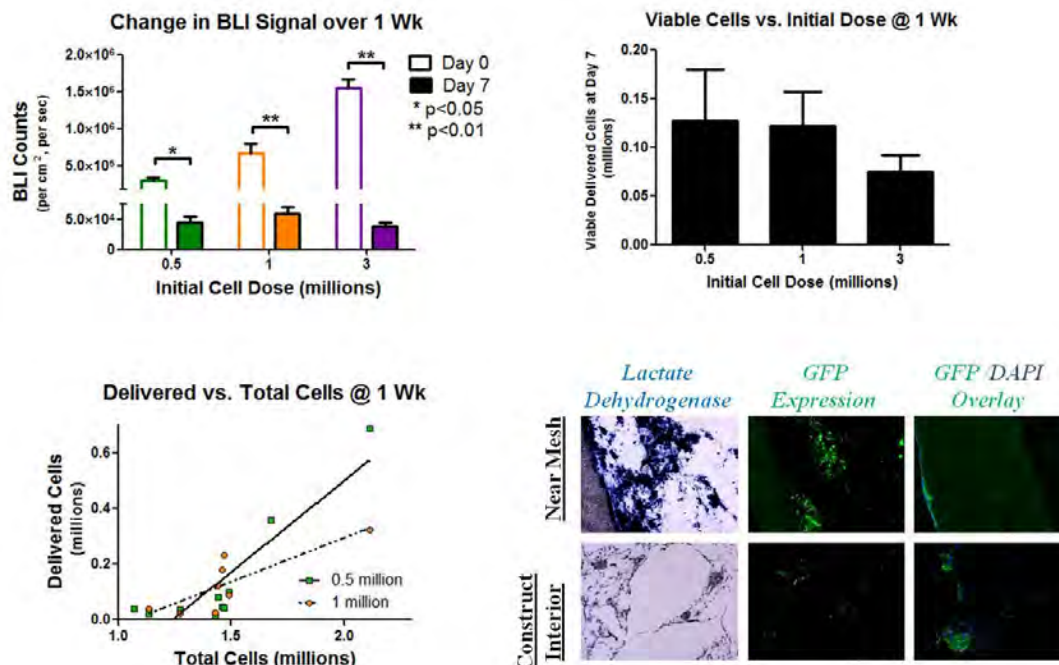
After determining that large-sized agarose constructs facilitated a relatively low stem cell survival rate, we investigated the utility of RGD-alginate hydrogel vehicles described previously and pooled human platelet lysate (pHPL) incorporation. pHPL has been shown to enhance stem cell proliferation in 2D culture and is capable of forming a hydrogel due to its fibrinogen content. However, because gels consisting solely of pHPL are fragile and challenging to manipulate (see images below), we assessed the impact of pHPL addition to the more mechanically stable RGD-alginate hydrogel. A pHPL incorporation dosing study was first conducted in vitro, where incorporation of pHPL within RGD-alginate hydrogels was found to increase the amount of viable hydrogel-embedded hMSCs in a dose-dependent manner over one day in culture (see images below). Interestingly, addition of pHPL caused a noticeable contraction along the periphery of the well suggesting cell interactions with the matrix.
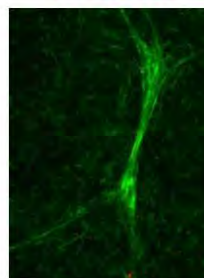
pHPL Addition to RGD-Alginate

BLI of Embedded-hMSCs
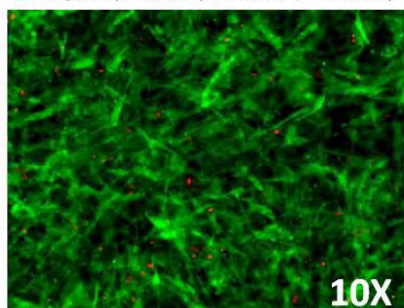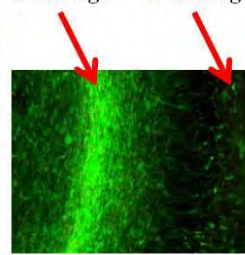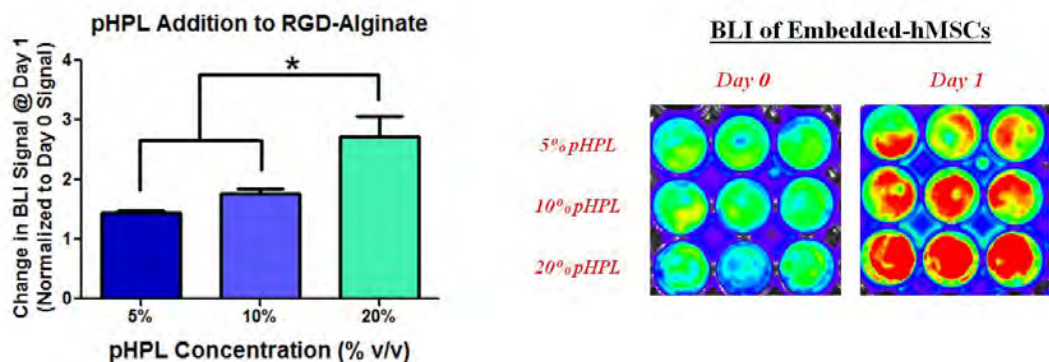
The impact of pHPL on delivered stem cell viability was next examined in vivo using a subcutaneous implant model in RNU nude rats. Preliminary studies were used to compare utility of the rat and mouse models and observed that one-week explants from rats demonstrated greater vascularization, improved histological processing for one-week explants, and would likely resemble tissues excised from our rat in vivo segmental defect model more similarly. In order to examine the potential impact of pHPL incorporation on delivered stem cell survival in vivo, an appropriate BLI protocol was first developed and verified (similar to the BLI technique previously validated in the NOD/SCID mouse model). Luciferin delivered via intraperitoneal (IP) injection resulted in no bioluminescent signal, likely due to mass transfer limitations imposed by the large of size of animal and of constructs. Local luciferin delivery, using one 0.3ml injection per construct at a concentration of 20mg/ml, resulted in an effective BLI protocol. The correlation between BLI signal and viable cell number when imaged at 30 minutes (data shown below) following luciferin injection was linear with an r-squared value of 0.9122. The correlation achieved from imaging conducted at 10 and 20 minutes following luciferin injection were also relatively high, with r-squared values of 0.8264 and 0.9096 respectively. BLI signal was measured over a one-week period to determine the effect of hMSC seeding dose on delivered cell survival. Lower cell doses (0.25 and 0.5 million hMSCs per construct) exhibited better survival in comparison to the higher cell dose groups, as is consistent with results from previous cell dose experiments conducted in our laboratory (data shown below; *=different within cell dose group, $=difference between cell dose groups within timepoint).
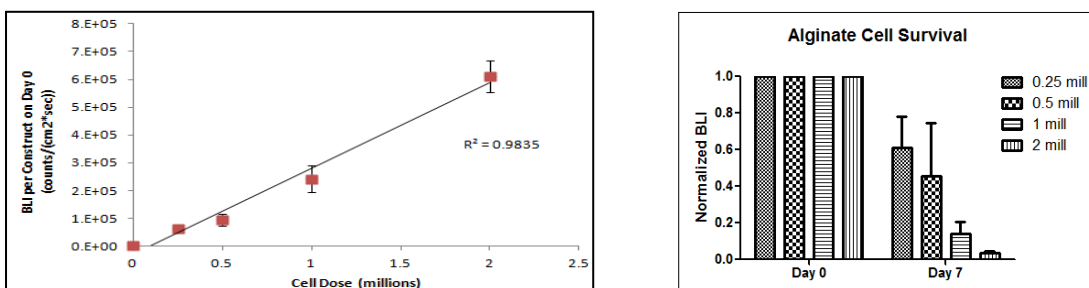
One-week evaluation of RGD-alginate constructs implanted subcutaneously in rats revealed a significant overall effect of pHPL incorporation on the viability of delivered hMSCs, although there was no effect within any given timepoint (see images below). The marginally higher day 0 signal for the pHPL-containing group may have been due to the 5-

hour culture period occurring between construct preparation and surgical implantation. Insufficient data points for the hAFSC constructs at day 0 prevented statistical analysis of BLI counts for this cell group, although qualitatively there appeared to be no impact of pHPL incorporation.
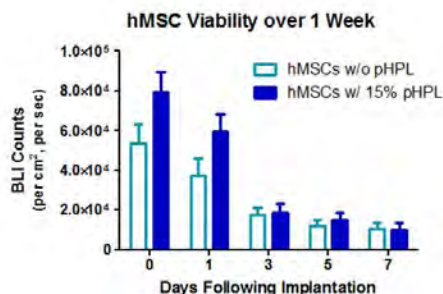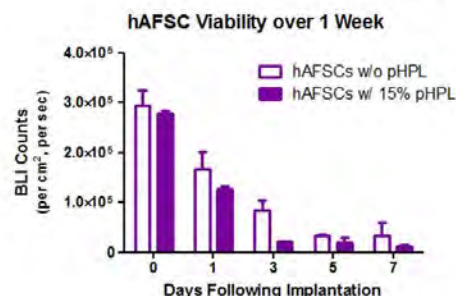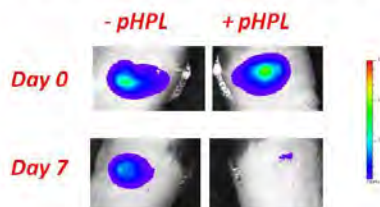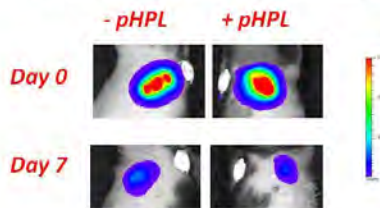
Vascular volume within the construct was greater for hMSC-seeded vs. acellular explants at one week, but there was no effect of pHPL incorporation (see images below). Briefly, this data was generated by perfusing the animals' vasculature with a radio-opaque dye and then explanting and scanning the samples via Micro-CT. Vascular morphology was evaluated by quantifying microCT voxel counts by vessel diameter. This data is presented in the forms of a histogram and binned diameter range chart. hMSC-seeded constructs had significantly more smaller vessels (<75μm-diameter) in comparison to the acellular group and there was no effect of pHPL addition. There was no effect of treatment on the counts for medium vessels (75-300μm-diameter), although cell delivery approached significance (p=0.07). Only hMSC-seeded constructs contained vessels within the largest diameter bin of >300μm. It is possible that greater effects of pHPL addition might have been seen with an adapted incorporation protocol or co-delivery of an osteogenic stimulus. Alternative modes of pHPL incorporation (such as adjustments in percentage volume, method of alginate integration and cross-linking, and pre-implantation construct culturing) may be required to produce greater efficacy.

Construct Vascularization at 1 Week

Representation Vascular Reconstructions
hMSC-Seeded · Acellular
hAFSC-Seeded

Vascular Morphology

Vessel Diameter Binning
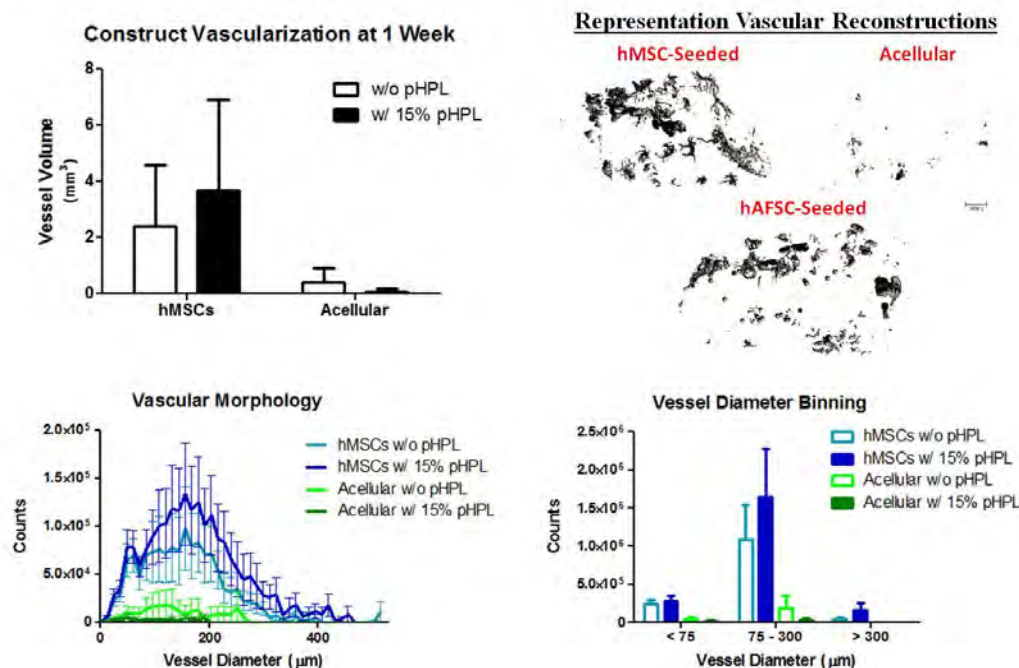
We have also assessed the RGD alginate system in terms of in vivo bone formation in a subcutaneous implantation model similar to the one used in the PEG system described previously. Briefly, 1 million cells were cross-linked into a 2% alginate hydrogel and then injected into a nanofiber mesh to retain the gel at the defect site. Constructs were implanted subcutaneously into the backs of RNU Nude rats and remained in the animal for 8 weeks. After 8 weeks constructs were explanted and scanned via Micro-CT. The groups tested were ADSCs, resveratrol treated ADSCS, carrier free resveratrol treated ADSCs (cells injected directly into the defect site without an alginate carrier), bone marrow stem cells as a positive cell control, and acellular constructs as a negative cell control. Carrier free and BMP free implants were also tested with the BMMSCs to determine if the hydrogel, cell source, and protein delivery are all necessary to produce robust mineralization in vivo. All groups (except the BMP free BMMSC group) received 2 µg of BMP-2 to stimulate bone formation in vivo.

Micro-CT imaging and processing showed that the bone marrow and acellular groups produced the most bone formation in vivo as shown in above in the 3-D reconstructions, with the adipose derived stem cells actually inhibiting bone formation in the hydrogels as shown in the Micro-CT reconstructions below. Both resveratrol treated and untreated ADSCs produced less than 2 mm^3 of bone tissue and there was no effect of resveratrol treatment. The acellular group had a mean of 13.7 mm^3 of bone tissue. Interestingly, 3 out of the 6 cellular samples produced fairly robust bone formation, while the other 3 did not. The bone marrow derived stem cell group with BMP co-delivery had a mean of 31.8 mm^3 of bone tissue and all 6 samples produced robust bone formation, and this group was significantly higher than all other groups. Removal of either the carrier or the BMP resulted in a significant decrease in bone formation. Following Micro-CT scanning, samples were decalcified and prepared for histology. Histological analysis was performed using H&E and Safranin-O stains, and further the presence of implanted cells was tested via immunohistochemistry for GFP positive cells. The presence of cells was observed in acellular constructs demonstrating host cell invasion into the hydrogel.

Further, mineralized tissue was only found where cells were present. ADSC loaded hydrogels had very little positive staining for mineralized tissue. In contrast, there were large areas on mineralization observed in BMMSC load hydrogels. For carrier free hydrogels, the majority of tissue present was granular and fibrous as there was no hydrogel in the construct to impede penetration of host tissue. GFP positive cells were found in cell loaded constructs, but were not found in acellular constructs. A majority of the cells present however were not positive for GFP demonstrating that a majority of the cells present in the construct after 8 weeks are from the invading host cells.
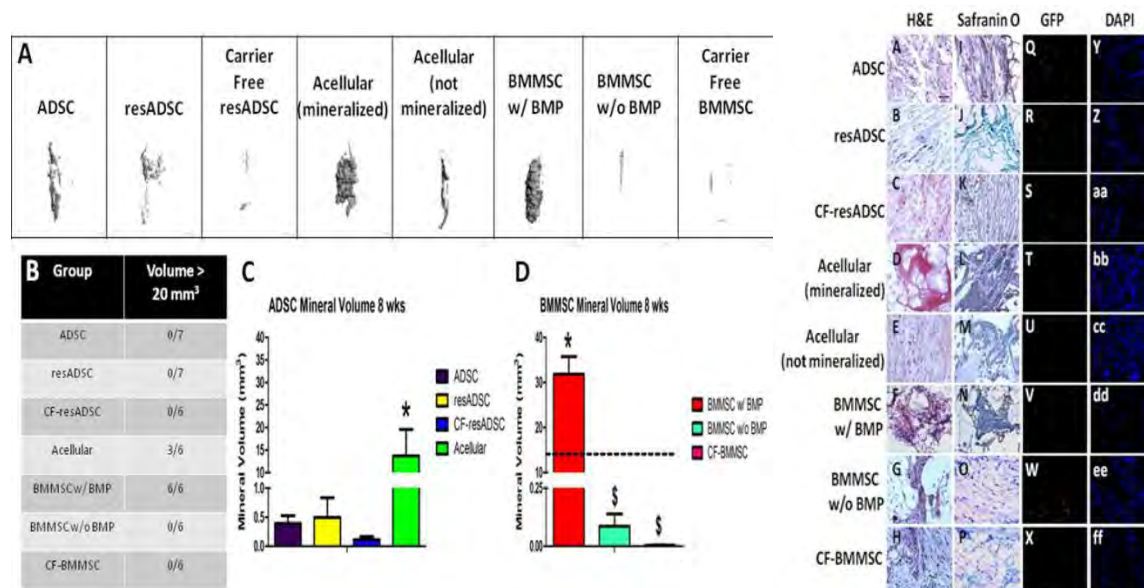
We investigated whether pooled human platelet lysate (pHPL) could be utilized more effectively as a pre-treatment strategy for hMSCs and hMSC-seeded RGD-alginate constructs to enhance cell survival following implantation. Our additional objective was to examine whether the establishment of cell attachment prior to *in vivo* delivery, by pre-culturing hydrogel constructs for 3 days, could improve maintenance of hMSC viability following delivery. For this study, we compared the impact of hMSC expansion in FBS (16%) vs. expansion in pHPL (5%) supplemented culture media and the delivery of pre-cultured vs. syringe-injected (hMSC-seeded hydrogel constructs prepared in the surgical suite) constructs on cell survival and vasculature after one week of subcutaneous implantation in nude rats. The impact of pHPL-culture on hMSC proliferation under subsequent environmental stress was first examined. It was found that expansion in pHPL-culture did not protect against serum starvation (1% BSA) or hypoxic (6% oxygen) environmental challenge *in vitro*, as no difference was found when compared to FBS-culture. Live (GFP; green)/dead (ethidium homodimer; red) fluorescence microscopy was conducted on hydrogel constructs at the time of implantation. All hMSC-seeded hydrogels contained a similar number of total cells and displayed no difference due to pHPL pre-conditioning. Pre-cultured (PC) constructs appeared to contain a higher fraction of dead cells in comparison to the syringe-injected (SI) equivalents.

Impact of Pre-Treatment Serum *In Vitro*
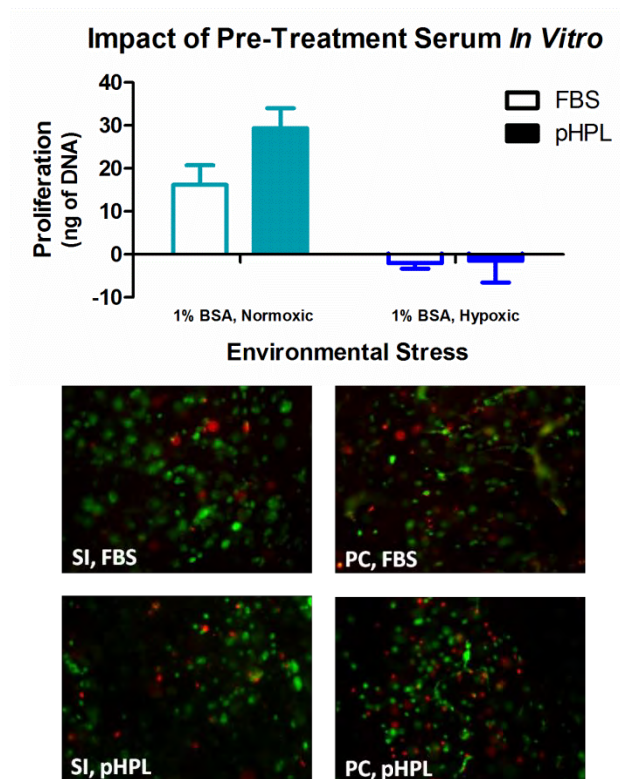
In vivo BLI revealed that fewer viable cells were delivered on Day 0 by the pre-cultured/pHPL-culture group (refer to "PC, PL" on the Absolute BLI chart). By Day 7, the syringe-injected/FBS-culture pre-treatment strategy ("SI, FBS" on the Normalized BLI chart) resulted in the greatest survival of hMSCs. (An asterisk (*) represents distinction from all other pre-treatment groups within that time-point; a dollar sign ($) represents a difference from the same pre-treatment group at Day 0.) Construct vasculature was found to be similar across pre-treatment groups. Overall, pre-culturing surprisingly did not assist cell survival upon implantation *in vivo*. As syringe-injected constructs better maintained cell viability at Day 7, the approach of combining stem cells and hydrogels in the surgical suite may be preferred to pre-culturing of constructs. These results also suggest that pre-conditioning with pHPL does not protect against cell death under nutrient- or oxygen-depleted conditions. In summary for the pHPL studies completed thus far, it is possible that sustained benefits of pHPL utilization might be seen with an adapted incorporation protocol or co-delivery of an osteogenic stimulus. Alternative modes of pHPL incorporation (such as adjustments in percentage volume, method of alginate integration and cross-linking, and delivery using the syringe-injectable technique) may be required to produce efficacy greater than that observed in the 15% pHPL co-delivery experiment.
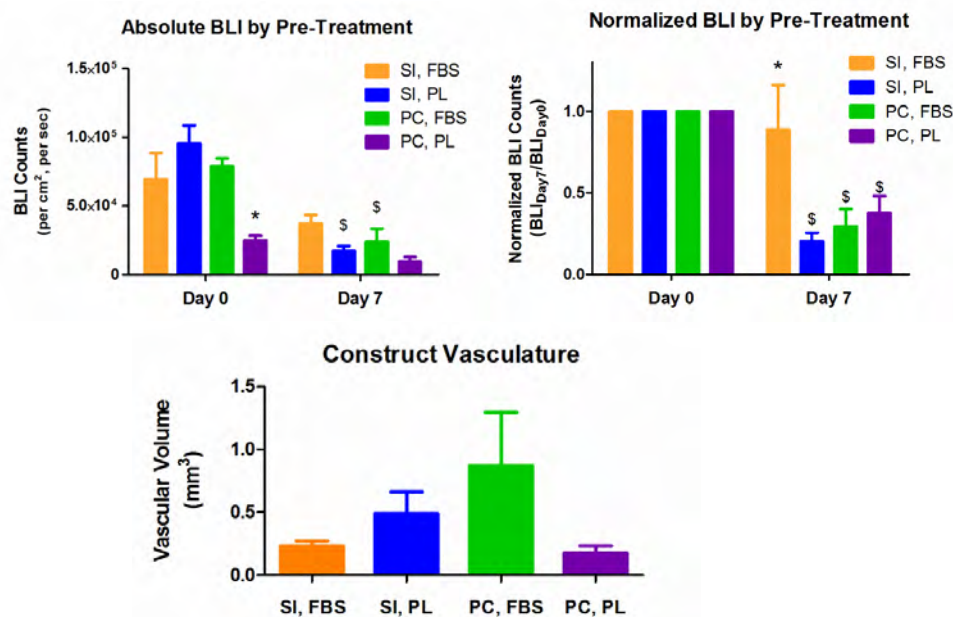
Task 6: Test scaffolds plus cells in the rat critical size defect model.

Given our results with the alginate hydrogel setup in the subcutaneous model, we have chosen to go forward with that system in our bone regeneration models over microencapsulation techniques. As sated previously, an alternative to immediate delivery of stem cells to a bone defect site is delayed cell implantation. The rationale behind this approach is that immediate implantation of stem cells is hindered by cell death due to the inflammation and lack of nutrients at the defect site. By injecting cells at a later time point, cell viability should be increased due to neovascularization at the defect site providing the delivery of nutrients and ridding the site of cellular waste products. Further, the injected cells would induce a

minimal inflammatory response as there would not be a large amount of tissue damage via injection with a needle. Thus far, we have modified the fixation plate used in the segmental defect by placing two holes in the middle of the plate in the defect area (as shown above) and have had the plates machined. We have also characterized empty defects as described below, and further have begun segmental defect surgeries at both an immediate and delayed time point.

Before performing the delayed injection surgeries, a proper time point for cell delivery needed to be indentified. To address this question, we performed a segmental defect surgery in the femur of the rat and used the fixation plate pictured above as an internal fixator. An 8 millimeter segmental defect was created in the femur and a poly-caprolactone nanofiber mesh was implanted into the defect site. After the mesh was implanted, the muscle and skin were sutured and closed leaving the defect site empty. At days 3, 7 and 14 legs were harvested and examined for tissue infiltration into the defect site. Micro-CT analysis of the defect site was performed to analyze bone remodeling on the bone ends over the 14 day time course. Cancellous bone in the medullary cavity was quantified for 600 microns adjacent to both sides of the defect site. Histological analysis

was performed using H&E staining for general morphology, and testing for macrophage presence via CD68 staining.

Micro-CT imaging showed that little bone formation occurred in the defect site over the 14 day time course. Analysis of the cancellous bone in the medullary cavity demonstrated that on the proximal side of the defect there was bone remodeling causing a significant decrease in the cancellous bone over time. Conversely, on the distal side there was a significant increase in the cancellous bone in the medullary cavity. It should be noted that both sides approached similar bone volume fractions by day 14. These results demonstrate that bone remodeling occurs quickly after the creation of the defect site.
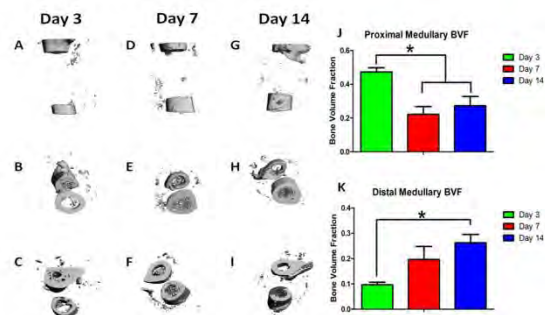
Histological analysis showed that over the 14 day time course there is a gradual filling of the defect site with granular tissue over the 14 day time course. At day 3 the defect site is still largely empty and there are few macrophages present in the defect site. Polymorphonuclear cells, indicative of neutrophils, were observed in the defect site and at the bone ends. Few macrophages were observed at day 3 in the defect site. By day 7 there is more tissue present in the defect site. Immunohistochemistry for macrophages showed a large presence of CD68 positive cells in the defect site demonstrating macrophage infiltration. A large polymorphonuclear cell presence was also observed via H&E staining. By day 14, the defect site is nearly filled with host tissue. On the bone ends, the tissue had an organized structure which may be indicative of the beginning of 'end capping' where the periosteum grows over the defect site in critically sized defects that do not achieve union. There was also a large presence of macrophages and polymorphonuclear cells present in the defect site at this time. Given these results, we determined that a 14 day time point may be the most advantageous time to deliver stem cells to the defect site. The presence of host tissue suggests that the implanted cells would be able to achieve nutrient exchange and further a cell carrier may not be needed at this time point as implanted cells could possibly graft into the infiltrated host tissue. Surgeries are currently underway to evaluate the difference in immediate and delayed delivery of stem cells into the segmental defect model and should be completed in the next two quarters.
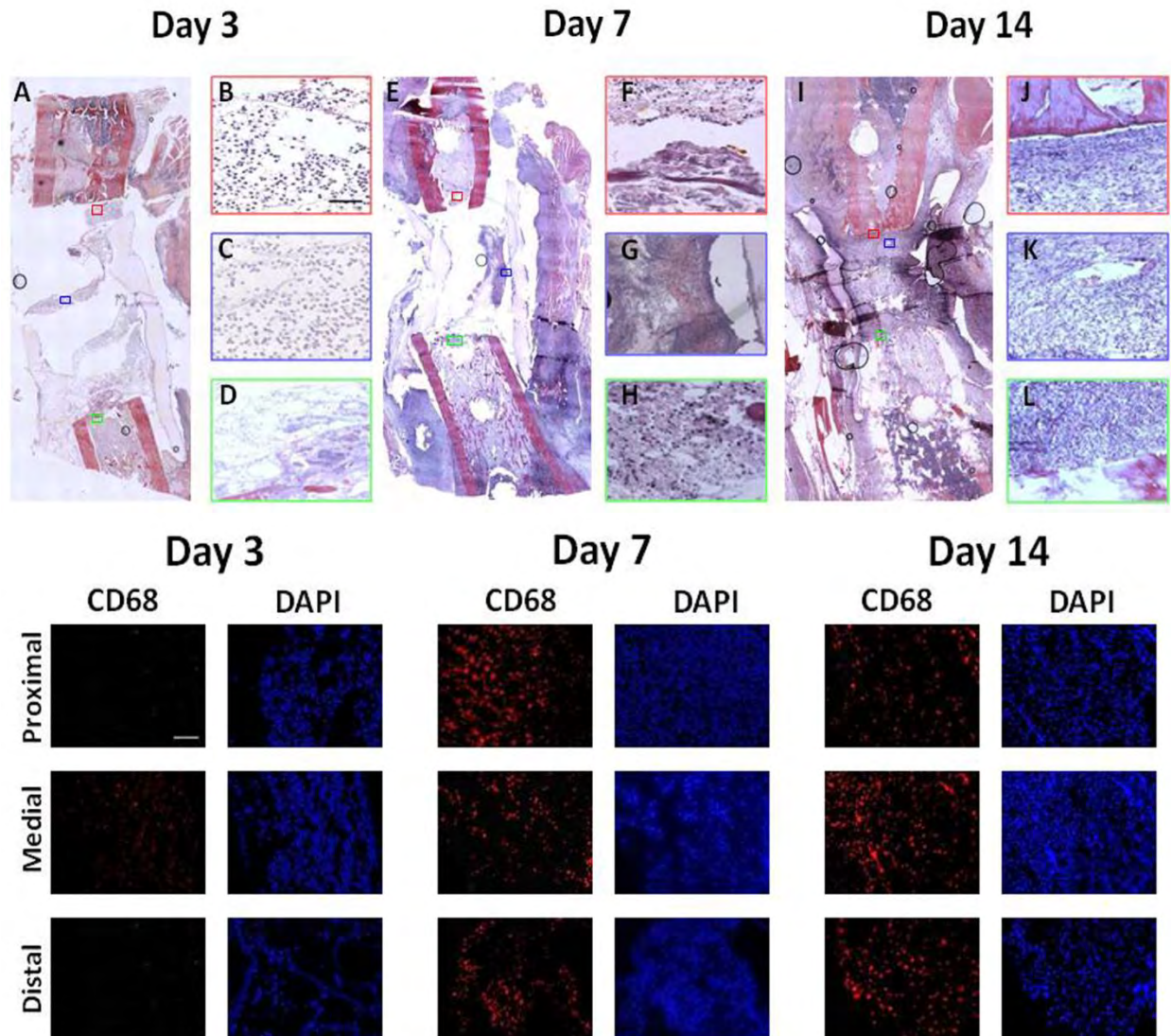
We have made tremendous progress in testing our alginate hydrogel system with and without cells in a rat segmental defect model. Our previous subcutaneous experiments demonstrated that the two viable candidates for observing mineralization were a bone marrow mesenchymal stem cell loaded hydrogel supplemented with BMP-2, and also a BMP-2 loaded hydrogel with no cells. We therefore tested these two groups along with an alginate hydrogel without any additional osteogenic factors to serve as a negative control in the segmental defect model. BMP-2 containing hydrogels received 1 microgram of BMP-2 and cell loaded hydrogels received 1 million GFP expressing BMMSCs. In this experiment, we also tested the effect of timing of delivery of the therapeutic and its ultimate influence on the bone regeneration process. For the delayed implant groups, segmental defects were created and the nanofiber mesh placed in the defect site and the animal was aseptically closed. 7 days later, we re-entered the defect site through the same incision, and injected our therapeutic into the defect site. Immediate delivery animals received their injected therapeutic at the time of surgery. The outcome measures for this experiment are bone volume as determined by micro-CT imaging, mean density of bone tissue, and histological

analysis for implanted cell retention and participation in the healing as well as general morphology.

In vivo micro-CT analysis at 8 weeks demonstrated that little to no bone formation occurs in the alginate hydrogels without BMP-2 as expected. For immediate delivery samples, the addition of BMP-2 causes a significant increase in the bone volume over non-BMP-2 containing hydrogels. The group with the most mineral at the 8 week time point is the immediate delivery group containing 1 million cells. This group was significantly greater than both the BMP-2 and non-BMP-2 containing hydrogels, as well as the delayed cell implantation group containing cells. In several samples the defect has mineral going throughout the defect site and is approaching a bridged defect. Interestingly, delayed therapeutic implantation resulted in significantly less mineralization in the BMP-2 containing hydrogels and the BMP-2 with cells hydrogels. There were no significant differences observed between any of the groups for the delayed therapeutic delivery, and none of the defects were bridged by this time point.

8 Weeks In vivo Bone Volume Results

* = significantly greater than No BMP
# = significantly greater than BMP
$ = significantly greater than delayed for that group
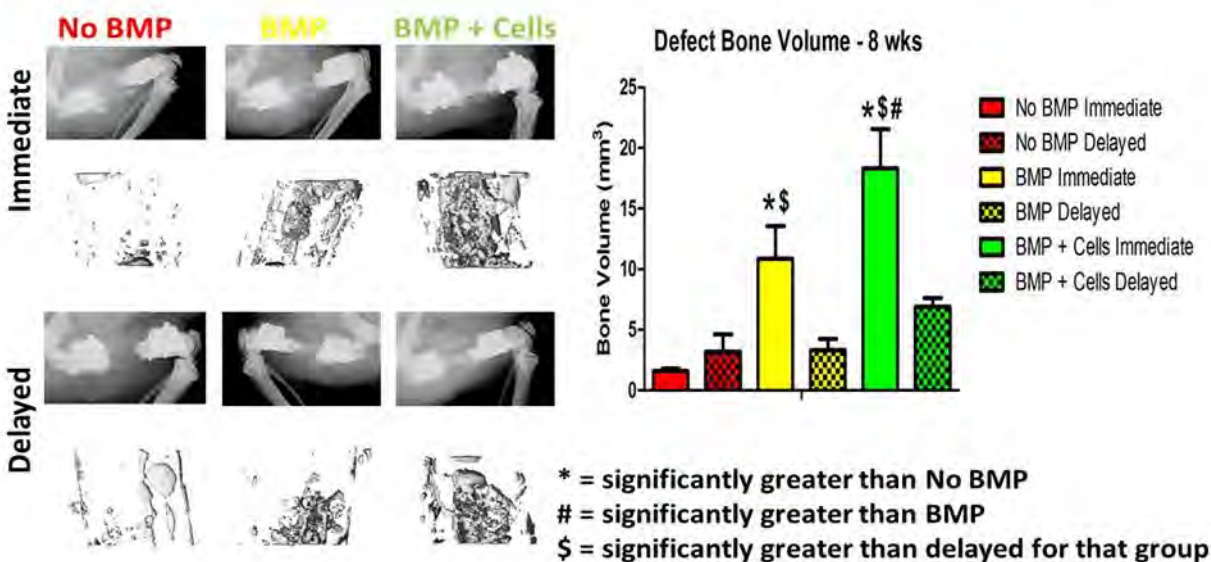
Similar results were observed at 12 weeks, albeit with elevated levels of bone volume compared to 8 weeks. Again there was a significant increase in bone volume for hydrogels containing BMP-2 over non-BMP-2 containing hydrogels.   The immediately delivered hydrogel containing BMP-2 and cells had significantly greater bone volume than BMP-2 only and non-BMP-2 loaded hydrogels.   For the delayed samples, a significant effect of including cells and BMP-2 was observed over non-BMP-2 loaded hydrogels. However, this group still had significantly less mineral than its immediately delivered

12 Weeks In vivo Bone Volume Results

* = significantly greater than No BMP
# = significantly greater than BMP
$ = significantly greater than delayed for that group

counterpart.   Analysis of the mean mineral density revealed no significant differences among any of the groups for any time point (data not shown). Current efforts to complete this experiment include histomorphometric analysis for implanted cells present 12 weeks after implantation.   We will also be performing general histology looking at the tissue present via H&E and Safranin-O staining. This experiment will be followed up with a 24 hour assessment of implanted cell viability at both the immediate and delayed time points, which will provide insight into the differences observed between the immediate and delayed cell loaded hydrogels.

Immediate versus Delayed Stem Cell Delivery

Last quarter we tested our hybrid alginate hydrogel/mesh system with and without cells in our rat segmental defect model. Our studies investigated bone marrow mesenchymal stem cell (BMMSC) loaded hydrogels supplemented with BMP-2, acellular hydrogels with BMP-2 and an alginate hydrogel without cells or osteogenic factors (negative control) in the segmental defect model. BMP-2 containing hydrogels received 1 µg BMP-2 and cell loaded hydrogels received 1×10^6 GFP positive BMMSCs. We also tested the effect of timing of delivery of the therapeutic and its influence on the bone regeneration process. In the delayed implant groups, segmental defects were created, the nanofiber mesh placed at the defect site and then seven days post surgery, the defect site was re-opened through the same incision and our therapeutic injected into the defect site. Immediate delivery animals received their injected therapeutic at the time of surgery. The

outcome measures for this experiment were bone volume as determined by micro-CT imaging, mean density of bone tissue, and histological analysis for implanted cell retention and participation in bone healing.

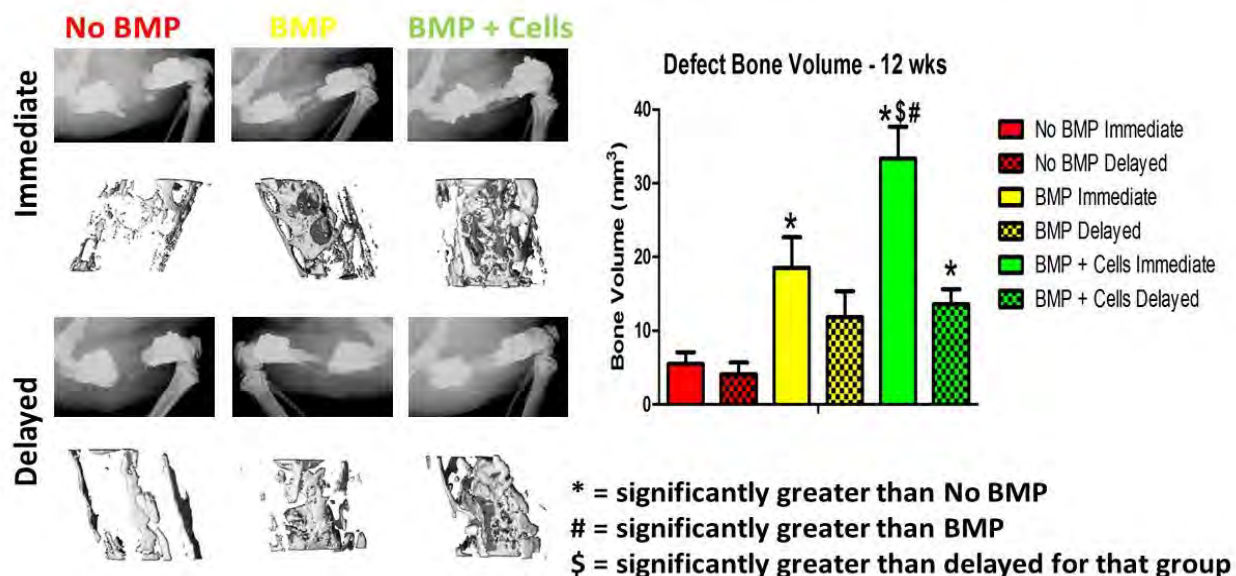We noted that at 12 weeks there was a significant increase in bone volume for hydrogels containing BMP-2 compared to non-BMP-2 containing hydrogels. The
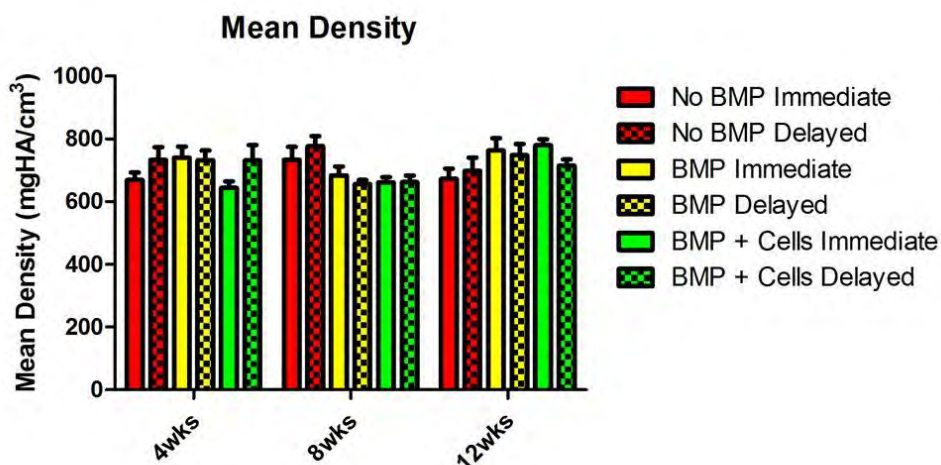
Figure 32. Mean mineral density of newly formed bone in tested hydrogels at 4, 8 and 12 weeks.

immediately delivered hydrogel containing BMP-2 and cells had significantly greater bone volume than BMP-2 only and non-BMP-2 loaded hydrogels. For the delayed samples, a significant effect of including cells and BMP-2 was observed over non-BMP-2 loaded hydrogels. However, this group still had significantly less mineral than its immediately delivered counterpart. Analysis of the mean mineral density revealed no significant differences among any of the groups for any time point (Fig. 32) indicating a similar level of bone maturity despite treatment or delivery time point.

Histological Analysis

H&E and Safranin-O staining of hydrogels lacking BMP-2 showed the presence of fibrous tissue along with remnants of alginate hydrogel. No areas of mineralization were observed in the defect site for both the immediate and delayed samples for this group (Figures 33 and 34). For BMP-2 containing hydrogels, areas of mature bone were observed. For both immediate and delayed samples, areas of alginate hydrogel were still observable after 12 weeks. Interestingly, in cell loaded alginate hydrogels, the alginate showed cells present in the hydrogel while acellular hydrogels lacked cells (arrows in Figure 33 and 34). Most of these cells however do not stain for nuclei on H&E staining, suggesting the cells are no longer functional after 12 weeks. Some cells are found along the surface of mineralized tissue, possibly indicating implanted cell mediated bone formation.
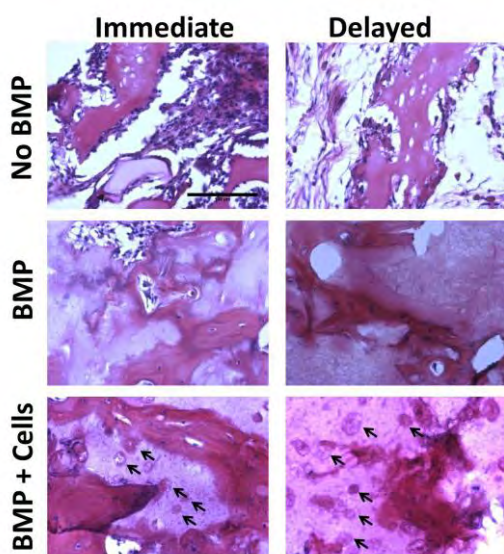
Figure 33. H&E staining of constructs after 12 weeks. Cell loaded alginate hydrogels still showed the presence of cells after 12 weeks (arrows). Scale bar = 100 μm.
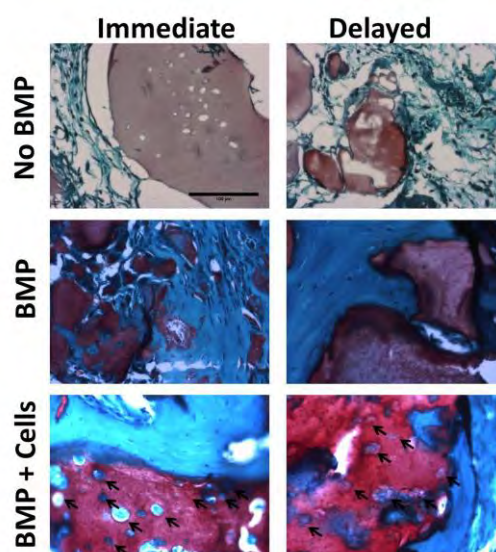
Figure 34. Safranin-O staining of constructs after 12 weeks. Cell loaded alginate hydrogels still showed the presence of cells after 12 weeks (arrows). Scale bar = 100 μm.

Immunohistochemistry for GFP showed very little positive staining, suggesting that by 12 weeks most of the implanted cells are no longer alive (Figure 35). This confirms what is seen in the H&E and Safranin-O stains of cell loaded constructs, where the lack of nuclei suggest that the cells are no longer metabolically active. Most of the cells visible in the H&E and Safranin-O stains did not stain positive for GFP.

In summary, our delivery approach, similar to the Masquelet technique where the defect site is re-opened through the initial incision and the therapeutic delivered to the defect site, accurately delivered hydrogels yet we observed a detrimental effect of delayed implantation compared to immediate implantation. However, a beneficial effect of stem cell delivery was observed over acellular hydrogels at both time points. Acellular samples consistently did not achieve bridging of the defect, while cell loaded constructs did achieve bridging of the defect in the majority of samples.
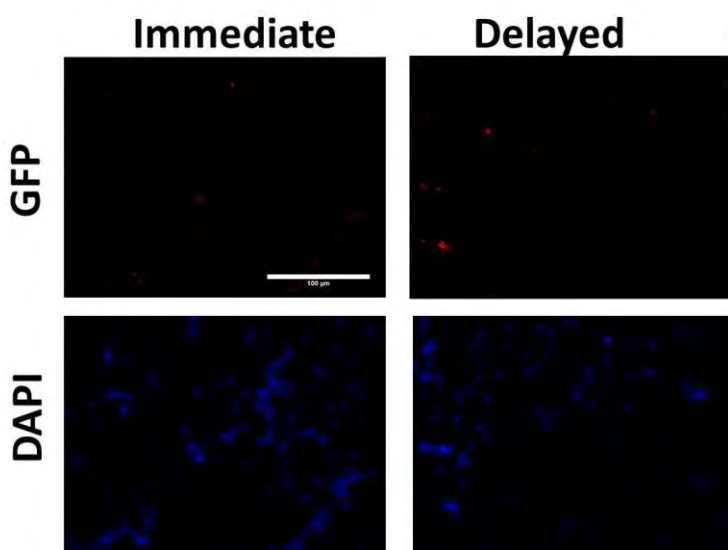
Figure 35. Immunohistochemistry for GFP positive cells after 12 weeks in cell loaded alginate hydrogels. Scale bar = 100 µm.

Our time points were chosen as we hypothesized that the presence of endogenous tissue in the defect site may facilitate nutrient and waste exchange of the delivered stem cells, provide attachment sites for the cells as well as recruit more host progenitors before the BMP-2 could be degraded. However, given our results, our delivery time may have been too late. The amount of granular tissue in the defect site may have inhibited bone formation, and the BMP-2 may have been degraded by inflammatory cells at the defect site, limiting endogenous host cell recruitment. In addition, during the second surgical procedure we did not clear the defect site of infiltrated tissue. A possible consequence of this is limited space for the hydrogel at the 7 day time point, similar to what was observed in the 14 day delivery samples. An alternative hypothesis is that immediate delivery of osteoinductive factors significantly affects the endogenous cells recruited to the defect site. The mechanisms underlying our results need further study.

Overall this study demonstrates that incorporation of adult stem cells into an injectable hydrogel is a viable system to promote repair of clinically challenging bone defects.

Specific Aim 7. Test feasibility of replacing injured or otherwise abnormal muscle with decellularized muscle.

Task 1. Obtain IACUC and ACURO approvals for the rat model to test different grafts.

Approvals were obtained, documentation provide in last quarter report.

Task 2. Determine optimal processing of decellularized muscle grafts to retain three dimensional tissue architecture and tensile strength and provide suture sites at each end.

The decellularized leg muscle (gastrocnemius) allograft is created by harvesting the gastrocnemius from the leg of a rat. Sharp transection at the distal portion of the calcaneal tendon as well as at the tendonous origin of the medial gastrocnemius allows for strong points of attachment. This will aid in attachment of the decellularized graft and the remaining tendon in the surgically created defect. The decellularization process, which is performed at the Musculoskeletal Transplant Foundation (MTF), involves removal of all

cells and their associated membrane proteins and DNA, so that only extra-cellular matrix materials remain. After this muscle is decellularized, the gastrocnemius will be excised from a different anesthetized rat. The decellularized muscle will then be sutured into the location of the excised muscle in the anesthetized rat. The recipient rat will then be observed for functionality and mobility in the days, weeks, and months post-operatively.

The team has found that complete decellularization destroys the mechanical properties of the implant with respect to suture. We have been able to partially decellularize by slicing it very thin, removing any DNA. This means it will be necessary to stack the slices prior to suturing in place to achieve enough tissue mass. The decellularized technology is approved for human use as a tissue graft. We have sent MTF rat muscle so that we can test effectiveness in vivo using a species specific material.

Task 3. Use a rodent model for screening the effectiveness of decellularized muscle grafts in vivo in order to determine if decellularized muscle grafts will restore muscle structure and function.

Muscle samples have been sent to Musculoskeletal Transplant Foundation for processing. We anticipate receiving them in early April. Upon receipt of the decellularized muscle grafts outlined under Task 2, an in vivo experiment will be conducted on 150-200g male immunocompromised rats (rNu/rNu). The experimental protocol will include five groups of 8 rats each:

Sham Surgery	8
Remove muscle only (empty defect)	8
Remove muscle and replace muscle (positive control)	8
Remove muscle and replace with decellularized graft	8
Remove muscle and replace with collagen sponge	8

The first study to demonstrate the model was completed. The results were used to refine the protocol that will be used for subsequent studies. This protocol was submitted to VCU's IACUC and has been approved. It is now being submitted to DoD for ACURO review.

Task 4. Determine if addition of MSCs or ASCs will improve graft effectiveness.

The full study will commence upon receipt of these materials from the Musculoskeletal Transplant Foundation.

Gantt Chart

Legend for cell fill: D = dark green, G = light green, B = blue

Aim 1	Q1 Y1	Q2 Y1	Q3 Y1	Q4 Y1	Q1 Y2	Q2 Y2	Q3 Y2	Q4 Y2	Q1 Y3	Q2 Y3	Q3 Y3	Q4 Y3	Status/Comments
Task 1	G	G	G	G	G	G	G	G	G	G	G	G	
Task 2	D												
Task 3	G	G	G	G	G	G	G	G	G	G	G	G	
Task 4	G	G	G	G	G	G	G	G	G	G	G	G	
Task 5	G	G	G	G	G	G	G	G	G	G	G	G	VCU subcontract
*Task 6									B				Proposed
Aim 2													
Task 1	D												
Task 2		D	D	D	D								
Task 3					G	G	G	G	B				
Task 4									B	B	B		
Task 5												B	
Aim 3													
Task 1	D												
Task 2	D	D	D										
Task 3			D										
Task 4				D	D								
Task 5						D	D	D					
Task 6		D	D	D	D								
Task 7					D	D	D						
Task 8							D	D	D				
Task 9									B	B	B		
Task 10												B	
Task 11						D							
Task 12							G	G	B	B	B	B	
Task 13							G	G	B	B	B	B	
Task 14							G	G	B	B	B	B	
Aim 4													
Task 1		D	D										
Task 2			D	D									
Task 3		D											
Task 4	D												
Task 5	D	D											
Task 6			D	D	D			B	B	B			VCU Subcontract
Task 7				D									
Task 8						G	G	B					VCU Subcontract/BDB
Task 9								B	B	B			VCU Subcontract/BDB
Task 10					G	G							VCU Subcontract
Task 11								B					VCU Subcontract/BDB
Task 12									B	B	B		VCU Subcontract
Task 13												B	VCU Subcontract
*Task 14									B				Proposed
*Task 15									B				Proposed

	Q1 Y1	Q2 Y1	Q3 Y1	Q4 Y1	Q1 Y2	Q2 Y2	Q3 Y2	Q4 Y2	Q1 Y3	Q2 Y3	Q3 Y3	Q4 Y3	Status/Comments
Aim 5													
Task 1	Completed												
Task 2		In progress	In progress					Yet to Start	Yet to Start				VCU Subcontract
Task 3				Delayed	Delayed	Delayed			Yet to Start	Yet to Start	Yet to Start		VCU Subcontract
Task 4												Yet to Start	VCU Subcontract
Task 5					Delayed	Delayed			Yet to Start	Yet to Start			VCU Subcontract
Task 6							Delayed	Yet to Start	Yet to Start	Yet to Start			VCU Subcontract
Task 7											Yet to Start	Yet to Start	VCU Subcontract
Task 8											Yet to Start	Yet to Start	VCU Subcontract
*Task 9									Yet to Start				Proposed
Aim 6													
Task 1	Completed												
Task 2	Completed												
Task 3		Completed	Completed	Completed									
Task 4					Completed	Completed							
Task 5					Completed	Completed							
Task 6							In progress	In progress	Yet to Start	Yet to Start			
Task 7										Yet to Start	Yet to Start		
Task 8											In progress	In progress	
Aim 7													
Task 1						Completed							
Task 2							In progress	Yet to Start	Yet to Start	Yet to Start	Yet to Start	Yet to Start	
Task 3							In progress	Yet to Start	Yet to Start	Yet to Start	Yet to Start	Yet to Start	
Task 4							In progress	Yet to Start	Yet to Start	Yet to Start	Yet to Start	Yet to Start	
*Task 5									Yet to Start				Proposed

Completed	Completed
In progress	In progress
Abandoned	**Abandoned due to changes in research strategy**
Yet to Start	Yet to Start
Delayed	Delayed

REPORTABLE OUTCOMES

Publications

Averett RD, Menn B, Lee EH, Helms CC, Barker T, Guthold M. A modular fibrinogen model that captures the stress-strain behavior of fibrin fibers. Biophys J. 2012 Oct 3;103(7):1537-44. doi: 10.1016/j.bpj.2012.08.038. Epub 2012 Oct 2. PMID: 23062346 [PubMed - indexed for MEDLINE].

Baker MI, Walsh SP, Schwartz Z, Boyan BD. A review of polyvinyl alcohol and its uses in cartilage and orthopedic applications. J Biomed Mater Res B Appl Biomater. 2012 Jul;100(5):1451-7. doi: 10.1002/jbm.b.32694. Epub 2012 Apr 19. PubMed PMID: 22514196.

Baraniak PR, Cooke MT, Saeed R, Kinney MA, Fridley KM, McDevitt TC. Stiffening of human mesenchymal stem cell spheroid microenvironments induced by incorporation of gelatin microparticles. J Mech Behav Biomed Mater. 2012 Jul;11:63-71. Epub 2012 Mar 3. PubMed PMID: 22658155.

Booth AJ, Hadley R, Cornett AM, Dreffs AA, Matthes SA, Tsui JL, Weiss K, Horowitz JC, Fiore VF, Barker TH, Moore BB, Martinez FJ, Niklason LE, White ES. Acellular normal and fibrotic human lung matrices as a culture system for in vitro investigation. Am J Respir Crit Care Med. 2012 Nov 1;186(9):866-76. doi: 10.1164/rccm.201204-0754OC. Epub 2012 Aug 30. PubMed PMID: 22936357; PubMed Central PMCID: PMC3530219.

Boyan BD, Hart DA, Enoka RM, Nicolella DP, Resnick E, Berkley KJ, Sluka KA, Kwoh CK, Tosi LL, O'Connor MI, Coutts RD, Kohrt WM. Hormonal modulation of connective tissue homeostasis and sex differences in risk for osteoarthritis of the knee. Biol Sex Differ. 2013 Feb 4;4(1):3. doi: 10.1186/2042-6410-4-3. PubMed PMID: 23374322; PubMed Central PMCID: PMC3583799.

Boyan BD, Tosi LL, Coutts RD, Enoka RM, Hart DA, Nicolella DP, Berkley KJ, Sluka KA, Kwoh CK, O'Connor MI, Kohrt WM, Resnick E. Addressing the gaps: sex differences in osteoarthritis of the knee. Biol Sex Differ. 2013 Feb 4;4(1):4. doi: 10.1186/2042-6410-4-4. PubMed PMID: 23374401; PubMed Central PMCID: PMC3571922.

Brown AC, Fiore VF, Sulchek TA, Barker TH. Physical and chemical microenvironmental cues orthogonally control the degree and duration of fibrosis-associated epithelial-to-mesenchymal transitions. J Pathol. 2013 Jan;229(1):25-35. doi: 10.1002/path.4114. PubMed PMID: 23018598.

Cao L, Zeller MK, Fiore VF, Strane P, Bermudez H, Barker TH. Phage-based molecular probes that discriminate force-induced structural states of fibronectin in vivo. Proc Natl Acad Sci U S A. 2012 May 8;109(19):7251-6. Epub 2012 Apr 23. PubMed PMID: 22529344; PubMed Central PMCID: PMC3358907.

Chen J, Dosier CR, Park JH, De S, Guldberg RE, Boyan BD, Schwartz Z. Mineralization of three-dimensional osteoblast cultures is enhanced by the interaction of 1α,25-dihydroxyvitamin D3 and BMP2 via two specific vitamin D receptors. J Tissue Eng Regen Med. 2013 Jun 20. doi: 10.1002/term.1770. [Epub ahead of print] PubMed PMID: 23784946 [PubMed - as supplied by publisher].

Chen J, Lobachev KS, Grindel BJ, Farach-Carson MC, Hyzy SL, El-Baradie KB, Olivares-Navarrete R, Doroudi M, Boyan BD, Schwartz Z. Chaperone properties of Pdia3 participate in rapid membrane actions of 1α,25-dihydroxyvitamin D3. Mol Endocrinol. 2013 May 9. [Epub ahead of print] PubMed PMID: 23660595 [PubMed - as supplied by publisher].

Clause KC, Barker TH. Extracellular matrix signaling in morphogenesis and repair. Curr Opin Biotechnol. 2013 May 28. doi:pii: S0958-1669(13)00109-2. 10.1016/j.copbio.2013.04.011. [Epub ahead of print] PubMed PMID: 23726156 [PubMed - as supplied by publisher].

Coleman R, Schwartz Z, Boyan B, Guldberg R. The Therapeutic Effect of Bone Marrow Derived Stem Cell Implantation Following Epiphyseal Plate Injury is Abrogated by Chondrogenic Pre-3 4 Differentiation. Tissue Eng Part A. 2012 Aug 24. [Epub ahead of print] PubMed PMID: 22920855.

Diab T, Pritchard EM, Uhrig BA, Boerckel JD, Kaplan DL, Guldberg RE. A silk hydrogel-based delivery system of bone morphogenetic protein for the treatment of large bone defects. J Mech Behav Biomed Mater. 2012 Jul;11:123-31. Epub 2011 Nov 28. PubMed PMID: 22658161; PubMed Central PMCID: PMC3367165.

Dosier CR, Erdman CP, Park JH, Schwartz Z, Boyan BD, Guldberg RE. Resveratrol effect on osteogenic differentiation of rat and human adipose derived stem cells in a 3-D culture environment. J Mech Behav Biomed Mater. 2012 Jul;11:112-22. Epub 2011 Aug 31. PubMed PMID: 22658160; PubMed Central PMCID: PMC3367162.

Elbaradie KB, Wang Y, Boyan BD, Schwartz Z. Sex-specific response of rat costochondral cartilage growth plate chondrocytes to 17β-estradiol involves differential regulation of plasma membrane associated estrogen receptors. Biochim Biophys Acta. 2013 Jan 7;1833(5):1165-1172. doi: 10.1016/j.bbamcr.2012.12.022. [Epub ahead of print] PubMed PMID: 23305904.

Erdman CP, Dosier CR, Olivares-Navarrete R, Baile C, Guldberg RE, Schwartz Z, Boyan BD. Effects of resveratrol on enrichment of adipose-derived stem cells and their differentiation to osteoblasts in two-and three-dimensional cultures. JTissue Eng Regen Med. 2012 Mar 30. doi: 10.1002/term.513. [Epub ahead of print] PubMed PMID: 22467433.

Fridley KM, Kinney MA, McDevitt TC. Hydrodynamic modulation of pluripotent stem cells. Stem Cell Res Ther. 2012 Nov 20;3(6):45. [Epub ahead of print] PubMed PMID: 23168068; PubMed Central PMCID: PMC3580475.

Gittens RA, Olivares-Navarrete R, Cheng A, Anderson DM, McLachlan T, Stephan I, Geis-Gerstorfer J, Sandhage KH, Fedorov AG, Rupp F, Boyan BD, Tannenbaum R, Schwartz Z. The roles of titanium surface micro/nanotopography and wettability on the differential response of human osteoblast lineage cells. Acta Biomater. 2013 Apr;9(4):6268-77. doi: 10.1016/j.actbio.2012.12.002. Epub 2012 Dec 8. PubMed PMID: 23232211.

Gittens RA, Olivares-Navarrete R, McLachlan T, Cai Y, Hyzy SL, Schneider JM, Schwartz Z, Sandhage KH, Boyan BD. Differential responses of osteoblast lineage cells to nanotopographically-modified, microroughened titanium-aluminum-vanadium alloy surfaces. Biomaterials. 2012 Dec;33(35):8986-94. doi: 10.1016/j.biomaterials.2012.08.059. Epub 2012 Sep 16. PubMed PMID: 22989383.

Gutowski SM, Templeman KL, South AB, Gaulding JC, Shoemaker JT, Laplaca MC, Bellamkonda RV, Lyon LA, García AJ. Host response to microgel coatings on neural electrodes implanted in the brain. J Biomed Mater Res A. 2013 May 13. doi: 10.1002/jbm.a.34799. [Epub ahead of print] PubMed PMID: 23666919 [PubMed - as supplied by publisher].

Hermann C, Lawrence K, Olivares-Navarrete R, Williams JK, Guldberg RE, Boyan BD, Schwartz Z. Rapid Re-synostosis Following Suturectomy in Pediatric Mice is Age and Location Dependent. Bone. 2012 Nov 27. doi:pii: S8756-3282(12)01381-6. 10.1016/j.bone.2012.11.019. [Epub ahead of print] PubMed PMID: 23201269.

Hermann CD, Lee CS, Gadepalli S, Lawrence KA, Richards MA, Olivares-Navarrete R, Williams JK, Schwartz Z, Boyan BD. Interrelationship of Cranial Suture Fusion, Basicranial Development, and Resynostosis Following Suturectomy in Twist1(+/-) Mice, a Murine Model of Saethre-Chotzen Syndrome. Calcif Tissue Int. 2012 Aug 18. [Epub ahead of print] PubMed PMID: 22903506.

Hermann CD, Richards MA, Chang R, Olivares-Navarrete R, Williams JK, Guldberg RE, Vidakovic B, Schwartz Z, Boyan BD. Biphasic fusion of the murine posterior frontal suture. Plast Reconstr Surg. 2013 Apr;131(4):727-40. doi: 10.1097/PRS.0b013e3182827585. PubMed PMID: 23542246 [PubMed - indexed for MEDLINE].

Hermann CD, Richards MA, Olivares-Navarrete R, Williams JK, Guldberg RE, Skrinjar O, Schwartz Z, Boyan BD. Algorithm to assess cranial suture fusion with varying and discontinuous mineral density. Ann Biomed Eng. 2012 Jul;40(7):1597-609. Epub 2012 Feb 14. PubMed PMID: 22350663.

Huang X, Yang N, Fiore VF, Barker TH, Sun Y, Morris SW, Ding Q, Thannickal VJ, Zhou Y. Matrix stiffness-induced myofibroblast differentiation is mediated by intrinsic mechanotransduction. Am J Respir Cell Mol Biol. 2012 Sep;47(3):340-8. Epub 2012 Mar 29. PubMed PMID: 22461426.

Kinney MA, McDevitt TC. Emerging strategies for spatiotemporal control of stem cell fate and morphogenesis. Trends Biotechnol. 2013 Feb;31(2):78-84. doi: 10.1016/j.tibtech.2012.11.001. Epub 2012 Dec 5. PubMed PMID: 23219200; PubMed Central PMCID: PMC3557560.

Kinney MA, Saeed R, McDevitt TC. Systematic analysis of embryonic stem cell differentiation in hydrodynamic environments with controlled embryoid body size. Integr Biol (Camb). 2012 Jun ;4(6):641-50. Epub 2012 May 18. PubMed PMID:22609810.

Kinney MA, Sargent CY, McDevitt TC. Temporal Modulation of β-Catenin Signaling by Multicellular Aggregation Kinetics Impacts Embryonic Stem Cell Cardiomyogenesis. Stem Cells Dev. 2013 Epub Jun 14. PubMed PMID: 23767804.

Kumar S, Hoffman SJ, Samadfam R, Mansell P, Jolette J, Smith SY, Guldberg RE, Fitzpatrick LA.   The effect of rosiglitazone on bone mass and fragility is reversible and can be attenuated with alendronate. J Bone Miner Res. 2013 Jul;28(7):1653-65. doi: 10.1002/jbmr.1918. PubMed PMID: 23456892 [PubMed - in process].

Lee CS, Burnsed OA, Raghuram V, Kalisvaart J, Boyan BD, Schwartz Z. Adipose stem cells can secrete angiogenic factors that inhibit hyaline cartilage regeneration. Stem Cell Res Ther. 2012 Aug 24;3(4):35. [Epub ahead of print] PubMed PMID: 22920724.

Lee CS, Watkins E, Burnsed OA, Schwartz Z, Boyan BD. Tailoring adipose stem cell trophic factor production with differentiation medium components to regenerate chondral

defects. Tissue Eng Part A. 2013 Jun;19(11-12):1451-64. doi: 10.1089/ten.TEA.2012.0233. Epub 2013 Mar 28. PMID: 23350662 [PubMed - in process].

Markowski MC, Brown AC, Barker TH. Directing epithelial to Mesenchymal transition through engineered microenvironments displaying orthogonal adhesive and mechanical cues. J Biomed Mater Res A. 2012 Aug;100(8):2119-27. doi: 10.1002/jbm.a.34068. Epub 2012 May 21. PubMed PMID: 22615133.

Mokarram N, Merchant A, Mukhatyar V, Patel G, Bellamkonda RV. Effect of modulating macrophage phenotype on peripheral nerve repair. Biomaterials. 2012 Dec;33(34):8793-801. doi: 10.1016/j.biomaterials.2012.08.050. Epub 2012 Sep 12. PubMed PMID: 22979988; PubMed Central PMCID: PMC3483037.

Munson JM, Bellamkonda RV, Swartz MA. Interstitial Flow in a 3D Microenvironment Increases Glioma Invasion by a CXCR4-Dependent Mechanism. Cancer Res. 2013 Mar 1;73(5):1536-46. doi: 10.1158/0008-5472.CAN-12-2838. Epub 2012 Dec 27. PubMed PMID: 23271726.

Nicolella DP, O'Connor MI, Enoka RM, Boyan BD, Hart DA, Resnick E, Berkley KJ, Sluka KA, Kwoh CK, Tosi LL, Coutts RD, Havill LM, Kohrt WM. Mechanical contributors to sex differences in idiopathic knee osteoarthritis. Biol Sex Differ. 2012 Dec 23;3(1):28. doi: 10.1186/2042-6410-3-28. PubMed PMID: 23259740; PubMed Central PMCID: PMC3560206.

Olivares-Navarrete R, Gittens RA, Schneider JM, Hyzy SL, Haithcock DA, Ullrich PF, Schwartz Z, Boyan BD. Osteoblasts exhibit a more differentiated phenotype and increased bone morphogenetic protein production on titanium alloy substrates than on poly-ether-ether-ketone. Spine J. 2012 Mar;12(3):265-72. Epub 2012 Mar 15. PubMed PMID: 22424980.

Olivares-Navarrete R, Hyzy SL, Gittens RA 1st, Schneider JM, Haithcock DA, Ullrich PF, Slosar PJ, Schwartz Z, Boyan BD. Rough titanium alloys regulate osteoblast production of angiogenic factors. Spine J. 2013 May 14. doi:pii: S1529-9430(13)00399-9. 10.1016/j.spinee.2013.03.047. [Epub ahead of print] PubMed PMID: 23684238 [PubMed - as supplied by publisher].

Olivares-Navarrete R, Raines AL, Hyzy SL, Park JH, Hutton DL, Cochran DL, Boyan BD, Schwartz Z. Osteoblast maturation and new bone formation in response to titanium implant surface features are reduced with age. J Bone Miner Res. 2012 Aug;27(8):1773-83. doi: 10.1002/jbmr.1628. PubMed PMID: 22492532.

Park JH, Wasilewski CE, Almodovar N, Olivares-Navarrete R, Boyan BD, Tannenbaum R, Schwartz Z. The responses to surface wettability gradients induced by chitosan nanofilms on microtextured titanium mediated by specific integrin receptors. Biomaterials. 2012 Oct;33(30):7386-93. Epub 2012 Jul 24. PubMed PMID: 22835642.
Park JH, Olivares-Navarrete R, Wasilewski CE, Boyan BD, Tannenbaum R, Schwartz Z. Use of polyelectrolyte thin films to modulate osteoblast response to microstructured titanium surfaces. Biomaterials. 2012 Jul;33(21):5267-77. Epub 2012 Apr 27. PubMed PMID: 22541354.

Phillips-Cremins JE, Sauria ME, Sanyal A, Gerasimova TI, Lajoie BR, Bell JS, Ong CT, Hookway TA, Guo C, Sun Y, Bland MJ, Wagstaff W, Dalton S, McDevitt TC, Sen R, Dekker J, Taylor J, Corces VG. Architectural Protein Subclasses Shape 3D Organization of Genomes during Lineage Commitment. Cell. 2013 Jun 6;153(6):1281-95. doi: 10.1016/j.cell.2013.04.053. Epub 2013 May 23. PubMed PMID:23706625.

Saxena T, Karumbaiah L, Gaupp EA, Patkar R, Patil K, Betancur M, Stanley GB, Bellamkonda RV. The impact of chronic blood-brain barrier breach on intracortical electrode function. Biomaterials. 2013 Jul;34(20):4703-13. doi: 10.1016/j.biomaterials.2013.03.007. Epub 2013 Apr 2. PubMED PMID: 23562053 [PubMed - in process].

Singh A, Suri S, Lee T, Chilton JM, Cooke MT, Chen W, Fu J, Stice SL, Lu H, McDevitt TC, García AJ. Adhesion strength-based, label-free isolation of human pluripotent stem cells. Nat Methods. 2013 May;10(5):438-44. doi: 10.1038/nmeth.2437. Epub 2013 Apr 7. PubMed PMID: 23563795 [PubMed - indexed for MEDLINE].

Sluka KA, Berkley KJ, O'Connor MI, Nicolella DP, Enoka RM, Boyan BD, Hart DA, Resnick E, Kwoh CK, Tosi LL, Coutts RD, Kohrt WM. Neural and psychosocial contributions to sex differences in knee osteoarthritic pain. Biol Sex Differ. 2012 Dec 17;3(1):26. doi: 10.1186/2042-6410-3-26. PubMed PMID: 23244577; PubMed Central PMCID: PMC3583673.

Soon AS, Smith MH, Herman ES, Lyon LA, Barker TH. Development of Self-Assembling Mixed Protein Micelles with Temperature-Modulated Avidities. Adv Healthc Mater. 2013 Feb 26. doi: 10.1002/adhm.201200330. [Epub ahead of print] PubMed PMID: 23441099 [PubMed - as supplied by publisher].

Stoppato M, Stevens HY, Carletti E, Migliaresi C, Motta A, Guldberg RE. Effects of silk fibroin fiber incorporation on mechanical properties, endothelial cell colonization and vascularization of PDLLA scaffolds. Biomaterials. 2013 Jun;34(19):4573-81. doi: 10.1016/j.biomaterials.2013.02.009. Epub 2013 Mar 19. PubMed PMID: 23522374 [PubMed - in process].

Sweeney E, Roberts D, Lin A, Guldberg R, Jacenko O. Defective Endochondral Ossification-Derived Matrix and Bone Cells Alter the Lymphopoietic Niche in Collagen X Mouse Models. Stem Cells Dev. 2013 Jun 18. [Epub ahead of print] PubMed PMID: 23656481 [PubMed - as supplied by publisher].

Thote T, Lin AS, Raji Y, Moran S, Stevens HY, Hart M, Kamath R, Guldberg RE, Willett NJ. Localized 3D Analysis of Cartilage Composition and Morphology in Small Animal Models of Joint Degeneration. Osteoarthritis Cartilage. 2013 Jun 5. doi:pii: S1063-4584(13)00833-9. 10.1016/j.joca.2013.05.018. [Epub ahead of print] PubMed PMID: 23747340 [PubMed - as supplied by publisher].

Uhrig BA, Boerckel JD, Willett NJ, Li MT, Huebsch N, Guldberg RE. Recovery from hind limb ischemia enhances rhBMP-2-mediated segmental bone defect repair in a rat composite injury model. Bone. 2013 Aug;55(2):410-7. doi: 10.1016/j.bone.2013.04.027. Epub 2013 May 7. PubMed PMID: 23664918 [PubMed - in process].

Uhrig BA, Clements IP, Boerckel JD, Huebsch N, Bellamkonda RV, Guldberg RE. Characterization of a composite injury model of severe lower limb bone and nerve trauma. J Tissue Eng Regen Med. 2012 Jun 11. doi: 10.1002/term.1537. [Epub ahead of print] PubMed PMID: 22689452.

Wang Y, Huang YC, Gertzman AA, Xie L, Nizkorodov A, Hyzy SL, Truncale K, Guldberg RE, Schwartz Z, Boyan BD. Endogenous Regeneration of Critical-Size Chondral Defects in Immunocompromised Rat Xiphoid Cartilage Using Decellularized Human Bone Matrix Scaffolds. Tissue Eng Part A. 2012 Jul 30. [Epub ahead of print] PubMed PMID: 22731693.

White DE, Kinney MA, McDevitt TC, Kemp ML. Spatial pattern dynamics of 3D stem cell loss of pluripotency via rules-based computational modeling. PLoS Comput Biol. 2013;9(3):e1002952. doi: 10.1371/journal.pcbi.1002952. Epub 2013 Mar 14. PubMed PMID: 23516345 [PubMed - in process].

Willett NJ, Li MT, Uhrig BA, Boerckel JD, Huebsch N, Lundgren TL, Warren GL, Guldberg RE. Attenuated human bone morphogenetic protein-2-mediated bone regeneration in a rat model of composite bone and muscle injury. Tissue Eng Part C Methods. 2013 Apr;19(4):316-25. doi: 10.1089/ten.TEC.2012.0290. Epub 2012 Nov 2. PbuMed PMID: 22992043 [PubMed - in process].

Wilson JL, McDevitt TC. Stem cell microencapsulation for phenotypic control, bioprocessing, and transplantation. Biotechnol Bioeng. 2013 Mar;110(3):667-82. doi: 10.1002/bit.24802. Epub 2013 Jan 17. PubMed PMID: 23239279.

Presentations

Boerckel, J.D., Uhrig, B.A., Willett, N.J., Guldberg, R.E., "Mechanical Regulation of Vascular Growth and Tissue Regeneration In Vivo," Proceedings of the National Academies of Science, 108(37):E674-80, 2011.

ORS Abstract and Presentation: Pan QF, Olivares-Navarrete R, Hyzy SL, Schwartz Z, Boyan BD. 24R,25-dihydroxy vitamin D3 prevents articular cartilage degradation induced by IL1□.
ORS Abstract and Presentation: Lee CSD, Burnsed OA, Raghuram V, Schwartz Z, Boyan BD. Adipose cells secrete factors that inhibit cartilage regeneration.

ORS Abstract and Presentation: Olivares-Navarrete R, Smith K, Hyzy SL, Haithcock D, Gall K, Boyan BD, Schwartz Z. Surface stiffness controls mesenchymal stem cell fate towards osteogenic and chondrogenic phenotype.

ORS Abstract and Presentation: Hermann CD, Wilson S, Ning X, Olivares-Navarrete R, Williams JK, Murthy N, Schwartz Z, Boyan BD. Click-hydrogel therapy for controlled delivery to bone defects.

ORS Abstract and Presentation: Dosier, C R; Lee, T T; Phelps, E A; Garcia, A J; Guldberg, R E. *In vivo* Osteogenic Differentiation of Adipose and Bone Marrow Derived Stem Cells in a Functionalized Hydrogel.

TERMIS-NA Poster: Dosier, C R; Lee, TT; Phelps, E A; Garcia, A J; Guldberg, R E. Manipulating Hydrogel Formation to Promote Prolonged Cell Viability *in vitro.* Selected as a finalist for Best Poster competition at TERMIS-NA 2011 Conference in Houston, TX.

TERMIS-NA Poster: Lee CSD, Watkins EA, Burnsed OA, Schwartz Z, Boyan BD. Chondrogenic medium and microencapsulation is effective in tailoring adipose stem cell trophic factor expression regardless of anatomical site, passage or donor age. Houston, TX 2011 .

TERMIS-NA Oral: Olivares-Navarrete R, Sutha K, Hyzy SL, Hutton DL, Schwartz Z, McDevitt T, and Boyan BD. Osteogenic differentiation of embryonic and adult stem cells is accompanied with shifts in membrane and nuclear vitamin D receptor expression. Houston, TX 2011.

CONCLUSIONS

- CABSS is on track with its proposed research tasks.
- VCU Subcontract and the required approvals are in process.
- Modifications to contract to incorporate these changes will be forwarded within the next quarter.

REFERENCES

1. Wang, Y., et al., *The synergistic effects of 3-D porous silk fibroin matrix scaffold properties and hydrodynamic environment in cartilage tissue regeneration.* Biomaterials, 2010. 31(17): p. 4672-81.

2. Erdman CP, D.C., Olivares-Navarrete R, Baile C, Guldberg RE, Schwartz Z, Boyan BD., *Effects of resveratrol on enrichment of adipose-derived stem cells and their differentiation to osteoblasts in two-and three-dimensional cultures.* Journal of tissue engineering and regenerative medicine, 2012 doi: 10.1002/term.513. [Epub ahead of print].

3. Tsai M, Kita A, Leach J, Rounsevell R, Huang JN, Moake J, Ware RE, Fletcher DA, Lam WA*: In vitro modeling of the microvascular occlusion and thrombosis that occur in hematologic diseases using microfluidic technology*, The Journal of clinical investigation 2012, 122:408-418.

APPENDIX

1. CABSS RETREAT 2013 AGENDA
2. CABSS RETREAT 2013 MINUTES

CABSS Retreat Agenda
Thursday, January 10, 2013

8:00AM-2:30PM

Location: Parker H. Petit Institute for Bioengineering and Biosciences
Room #: 1128 – IBB Suddath Seminar Room
Address: 315 Ferst Drive, Atlanta, GA 30332

8:00 a.m.	**REGISTRATION** *Breakfast provided*	
8:30 a.m.	Welcome and Introduction	Barbara D. Boyan
	CABSS Investigators Progress Report and New Directions	
8:50 a.m.	Cartilage Regeneration - Microbeads	Barbara D. Boyan
9:15 a.m.	Acellular Therapies Derived from Stem Cells	Todd McDevitt
9:40 a.m.	Composite Models of Severe Limb Trauma	Robert E. Guldberg
10:05 a.m.	**COFFEE BREAK**	
10:20 a.m.	Internal Bleeding Detection Mechanism	Ravi Bellamkonda
10:45 a.m.	Wound Stasis and Repair	Thomas Barker
11:20 a.m.	**POSTER SESSION: LUNCH BREAK**	
	New Project Ideas	
12:30 p.m.	Post Traumatic Osteoarthritis	Nick Willett
12:45 p.m.	Osteoarthritis: Sex Differences	Rene Olivares-Navarrete
1:00 p.m.	Infection-resistant Biomaterials	Andres Garcia
1:15 p.m.	Traumatic Brain Injury (TBI)	Shean Phelps
1:30 p.m.	Advisory Board Closed Meeting	David Cohen/Maria Britt
2:00 p.m.	Future Strategic Plan	

CABSS Retreat 2013

1.10.2013	8 am – 2:30pm	Georgia Tech IBB 1128
Meeting called by	Dr. Barbara Boyan	
Type of meeting	Board of Directors	
Facilitator	Maria Britt	
Note taker	Martha Willis	
Timekeeper		
Attendees	Maria Britt, Peggy Wilmoth, Linda Cendales, Joe Williams, David Cohen, Tim Patrick.	

Topics:		
What makes CABSS unique?		
Are the problems we are addressing relevant to military medical problems? Gaps?		
Are there other funding opportunities we need to leverage?		
What is the "way ahead" for CABSS?		

What makes CABSS unique?	
Discussion	Maria Britt opened with the question "What makes CABSS Unique?"

The board focused on the interdisciplinary, collaborative "brain trust" that resides within the center. This "uniqueness" provided the back drop for most of the meetings' discussion since it is critical to the success of CABSS. The Center was established as a result of DoD funding, so projects were reviewed and proposed for funding with a focus on the military.

Everyone agreed that the collaboration of scientists, engineers, practicing clinicians, physicians and industry is the model for future program funding. All agreed that the investment the team members have made in working with, and getting to know one another is worth preserving. Although the center should seek additional funding for related programs from other avenues, the consensus was to keep the focus on military health issues.

There was a short discussion on changing the name of the center and looking at an expanded scope of mission. The board agreed that the name was appropriate and broad enough for future missions. There was some discussion about the aspect of "translation" and "commercialization" that has in the past been part of the focus of CABSS. There was consensus that it is important for ideas to get developed into products, approved and then manufactured quickly so that there could be a positive impact on soldiers' quality of life.

Conclusions	

What makes CABSS unique is the DoD focus, the brain trust, and the collaborative network that has been established. Once it was determined that leadership would continue with Dr. Boyan and Dr. Guldberg, all agreed that the CABSS name was good for "brand recognition," and that even if the mission expands, the military focus, the branding, and the collaborative team of scientists, engineers, practicing clinicians, physicians and industry are important to preserve.

Are the problems we are addressing relevant to military medical problems? Gaps?
Discussion
The original mandate/mission of CABSS was focused on tissue regeneration and traumatic injury.   Although still critical, many in the group noted that there should be an expanded scope to include chronic health issues as the troop drawdowns continue. Projects in osteoarthritis have recently been submitted but not funded. Presentations on new project ideas covered a wide range of issues, including post traumatic osteoarthritis, sex differences in osteoarthritis, internal bleeding detection, infection-resistant biomaterials, and traumatic brain injury.
Conclusions
All EAB members agreed that the focus of the center should be expanded based on the military situation and resourcing constraints. Chronic diseases including osteoarthritis and funding from the VA and NIH were areas to target in the future.

Are there funding opportunities we need to leverage medical problems? Gaps?
Discussion
Shrinking budgets in DoD and lack of additional funding for CABSS this year point to the need for additional funding sources. Areas mentioned included the NFL/TBI, NIH and the VA. All agreed that although CABSS has a military focus, the translation of medical advances is still needed for similar health issues in the general public. The projects are important for all of society in terms of traumatic injuries as well as chronic diseases. FDA medical device "fast track" approval has worked for only a single product, and it was a sophisticated prosthetic arm that would help wounded warriors. This illustrates a significant benefit in the area of medical device development and its alignment with a military requirement.
Conclusions
The board agreed on the benefit of reaching out to additional funding sources to support CABSS and related projects. VA was the major focus of future opportunities. The collaborative value of CABSS makes it unique. The interdisciplinary mix of scientists, engineers, practicing clinicians, physicians and industry, is critical in seeking grant funding, especially from DoD.

What is the "way ahead" for CABSS?
Discussion
Initially the group was unaware of how CABSS would be handled with Dr. Boyan transitioning to VCU. This was clarified upon discussion with Dr. Boyan following the session with the board. Another issue discussed centered on the composition of board membership. It was recommended to add a practicing military surgeon to the board in order to understand the most up to date military medical challenges. A second recommendation is to add a military industry member. This individual would be of value in creating understanding of the private industry process for translating technology into product.
Conclusions
The CABSS framework is working and valuable to future grant proposals. All agreed that keeping Dr. Boyan as a key leader of CABSS is important. The joint venture with Dr. Boyan at VCU and Dr. Guldberg at GT creates a stronger synergy of effort. The board agreed that the focus on the military should remain, but that a shift in mission towards chronic diseases and quality of life issues would be advantageous. Seeking additional funding sources through the VA and NIH was also recommended.